X-901-76-164

 NASA TM X- 71207

GEOLOGICAL APPLICATIONS OF NIMBUS RADIATION DATA IN THE MIDDLE EAST

LEWIS J. ALLISON

OCTOBER 1976

GODDARD SPACE FLIGHT CENTER
GREENBELT, MARYLAND

For information concerning availability
of this document contact.

Technical Information & Administrative Support Division
Code 250
Goddard Space Flight Center
Greenbelt, Maryland 20771

(Telephone 301–982–4488)

X-901-76-164

GEOLOGICAL APPLICATIONS OF NIMBUS RADIATION DATA IN THE MIDDLE EAST

Lewis J. Allison
Meteorology Program Office

October 1976

GODDARD SPACE FLIGHT CENTER
Greenbelt, Maryland

GEOLOGICAL APPLICATIONS OF NIMBUS RADIATION DATA IN THE MIDDLE EAST

Lewis J. Allison

Goddard Space Flight Center

Greenbelt, Maryland 20771

ABSTRACT

Large plateaus of Eocene limestone and exposed limestone escarpments, in Egypt and Saudi Arabia respectively, were indicated by cool brightness temperatures $T_B < 240°$ to 265°K by the Nimbus 5 Electrically Scanning Microwave Radiometer (ESMR) over a 2-year period. Nubian sandstone, desert eolian sand and igneous-metamorphic rocks of the Pliocene, Miocene, Oligocene and Cretaceous period were differentiated from these limestone areas by warm T_B values ($> 265°$ to 300°K). These brightness temperature differences are a result of seasonal in-situ ground temperatures and differential emissivity of limestone (0.7) and sand, sandstone and granite (0.9) whose dielectric constants are (6 to 8.9) and (2.9 and 4.2 to 5.3) respectively at 19.35 GHz. Cool T_B values in the form of a "V", were found oriented N/S over broad areas of the Nile Valley southward to Lake Nasser and

NW/SE from the Kharga Oasis to the Baharia Oasis in the Western Desert of central Egypt. Surface moisture from sub-surface leakage from the Aswan Dam and the Western Desert oases could be a secondary cause for this T_B value drop. Similar cool T_B values were shown over limestone-dolomitic hills of the Interior Homocline and the Hadramawt Plateau of Saudi Arabia. Nimbus 5 and 6 ESMR T_B values selectively identified intermediate dense rock types (limestone versus sandstone/granite) in the Lake Nasser region whose thermal inertia ranged from 0.035 to 0.06 cal cm^{-2} °C $sec^{-½}$. Space albedo was determined from spatially averaged (1 km resolution) Landsat 1, MSS-7 (0.8 to 1.1 μm) data and day-night ground brightness temperature differences from Nimbus 5 THIR 11 μm data (9 km resolution) under clear sky conditions.

CONTENTS

ILLUSTRATIONS

ILLUSTRATIONS (Cont.)

ILLUSTRATIONS (Cont.)

ILLUSTRATIONS (Cont.)

ILLUSTRATIONS (Cont.)

ILLUSTRATIONS (Cont.)

ILLUSTRATIONS (Cont.)

TABLES

INTRODUCTION

Early television pictures of the Middle East recorded by TIROS 1 to 5 (Schnapf, 1962, World Meteorological Organization, 1963) and geophysical observations by Nimbus 1 to 4 and Gemini 4, provided the first detailed satellite images of geological interest (Nordberg and Samuelson, 1965, Lowman and McDivitt, 1967, Pouquet, 1968, 1969, Pouquet and Raschke, 1968, Merrifield et al., 1969, Sabatini et al., 1971). With the flight of Landsat 1 in July 1972, more sophisticated rock type discrimination techniques were developed using computer-enhanced images recorded in the 0.5 to 1.1 μm region (Rowan et al., 1974, Blodget et al., 1975).

The Nimbus 5 and 6 meteorological satellites which were launched on 12 December 1972 and 12 June 1975 respectively, carried the electrically scanning microwave radiometer (ESMR) and the temperature-humidity infrared radiometer (THIR) which recorded useful complimentary data.

The purpose of this paper is to study the geological features of selected Middle East regions using the combination of Nimbus 5 and 6 ESMR and THIR primarily, with supportive data from Landsat 1, NOAA 2 and 4, US Air Force DMSP images and USGS geological charts and reports. The following sections contain a brief description of the two radiometers used in this study.

THE ELECTRICALLY SCANNING MICROWAVE RADIOMETER (ESMR)

The Nimbus 5 and 6 were flown in near-polar (81° retrograde) sun-synchronous circular orbits of about 1100 km (600 n. miles). Each orbit crossed the equator with an approximate 27° longitude separation and a period of 107 minutes (Nimbus 5 User's Guide, 1972, Nimbus 6 User's Guide, 1975). The basic physics behind the Nimbus 5 and 6 ESMR are the same although the scanning geometry and operating wavelengths are different.

The Nimbus 5 ESMR measures the earth and atmosphere radiation in a 250 MHz band centered at 19.35 GHz (1.55 cm) with a noise equivalent temperature difference (NEΔT) of approximately 2°K (Fig. 1a). It scans the earth every 4 secs. from 50° to the left through nadir to 50° to the right in 78 steps with some overlap. The scanning process is controlled by an onboard computer and scans a region approximately 30° of longitude wide at 30°N. The half-power beamwidth of the antenna is 1.4° or 22 km at nadir and 2.2° or 45 by 160 km at the 50° nadir angle edges. The instrument is discussed by Wilheit, 1972, Allison et al., 1974, 1975, Wilheit et al., 1976 and Kidder, 1976.

The Nimbus 6 ESMR receives thermal radiation from the earth in a 250 MHz band centered at 37 GHz (0.81 cm) (Fig. 1b). Each electrically scanned sweep records brightness temperatures at 71 steps over a 5.3 sec. period and scans a region approximately 13° of longitude wide at 30° N. The antenna beam

scans ahead of the spacecraft along a conical surface with a constant 45° angle with respect to the antenna axis and delineates a 15 km to 30 by 60 km field of view at the earth's surface with an NEΔT of 1°K. The Nimbus 5 ESMR measures only the horizontally polarized component while the Nimbus 6 ESMR measures the horizontal and vertical components by using two radiometer channels. A full description of this instrument has been discussed by Wilheit, 1975.

The microwave brightness temperature of the earth's surface is mainly effected by the surface emissivity and temperature, atmospheric water vapor and liquid water droplets. Cloud ice crystals (cirrus) have little effect on microwave radiation and at the Nimbus wavelengths are essentially transparent. Molecular oxygen absorption can also be neglected (Wilheit et al., 1975, Sabatini, 1975). The emissivity of the surface may vary due to the change in dielectric constant. Since the dielectric constant of water can be 80 and dry soil as low as 3 to 5, water content of soil can have a strong effect at microwave frequencies (Schmugge et al., 1974 (a and b), Meneely, 1975). The resulting soil emissivity can vary from 0.5 (wet) to 0.9 (dry) (Poe et al., 1971). The emissivity of non-vegetating surfaces can vary from 0.85 to > 0.95 and depending on the soil moisture content, the occurrence of dew, the surface temperature and receiver polarization, can indicate microwave brightness temperatures between 205° to $> 310°$K. Surface microwave radiation can

be effected by roughness, topographic slope, stratigraphy (layering of different materials), density of rocks, vegetation cover, receiver wavelengths, and angle of incidence observed (Oberste-Lehn, 1970, Cihlar and Ulaby, 1974, Vickers and Rose, 1971). Ocean surfaces have a low emissivity of ca. 0.40 and a resulting cold microwave brightness temperature of 120° to 170°K (horizontal polarization) and 190° to 220° K (vertical polarization).

THE TEMPERATURE-HUMIDITY INFRARED RADIOMETER (THIR)

The Nimbus 5 and 6 satellites carried the THIR, a two-channel radiometer which had proven its reliable performance by recording several years of day-night data indicating cloud heights, ground and sea temperature and providing a qualitative estimate of mid-tropospheric humidity under clear sky conditions (Allison et al., 1975).

The two THIR detectors consist of germanium-immersed thermistor bolometers which have peak spectral responses in the 10.5 - 12.5 μm "window" region and the 6.3 - 7.25 μm water vapor absorption region (Figure 2). A cutaway of the radiometer, shown in Figure 3, includes the scan mirror, sun shield, 5 inch-folded optical Cassegranian telescope, a dichroic beam splitter, electronics module and two detectors.

The elliptically-shaped plane scan mirror, inclined at 45 degrees to the optical axis of the instrument, rotates at 48 rpm and scans through a 360 degree angle in the plane perpendicular to the direction of motion of the satellite.

Figure 4 shows the 7.7 by 7.7 km (4.1 by 4.1 n. miles) ground resolution (scan spot) of the 11 μm channel at zero degree nadir increasing to an elongated 14 by 31.8 km scan spot at 50 degrees nadir, at an 1112 km (600 n. mile) orbital altitude. Similarly the ground resolution of the 6.7 μm channel at the sub-satellite point was 22.6 km while at 50 degrees nadir, it was 41.1 km by 93.5 km.

A sample Nimbus 5 THIR (11 μm) scan sequence is shown in Figure 5. The two detectors simultaneously view the housing, A at spacecraft zenith, (zero seconds). Seven synchronous pulses start at C, followed by six-1 volt calibration steps. A space scan starts at D to G, followed by an earth scan (117° wide) to I, a space scan to K, a housing scan to M, and then back to zenith. The entire sequence lasts 1.23 seconds. The space and housing-viewed parts of the scan serve as part of the in-flight check of calibration. Note the small noise ripple on the housing and space scans (McCulloch, 1972). The NE ΔT for the 11 μm channel is approximately 1.5°K at 185°K and 0.28°K at 300°K. Corrections of 2 to 7°K must be added for losses due to atmospheric water vapor. A correction of < 1°K may be disregarded for extremely dry desert atmospheres, which was the case in this study.

CASE STUDIES

Two areas of the Middle East were examined using the Nimbus 5 and 6 ESMR and THIR data in order to explain the repetitive occurrance of distinctive cool

microwave surface brightness patterns on successive cloud-free days and nights over a 2 year period.

EGYPT

A light gray "V" structure was noted in the Nimbus 6 ESMR pictures in the region of north-central Egypt (Fig. 6). A computer-produced grid print map (1:2 million, Mercator) of this scene (Fig. 7) shows cool brightness values of $< 240°K$ to $265°K$ overlaying the Nile Valley, Lake Nasser and extending northwestward along a line of known oases in the Western Desert. A review of all Nimbus 5 and 6 ESMR pictures over Egypt was made from December 1972 to the June 1976. This "V" structure appeared consistently in the imagery both day and night under cloud-free conditions. Two geological maps of Egypt (Figs. 8 and 9) delineate the Eocene limestone (Said, 1962) and Nubia sandstone (Issawi, 1973). These rock formations together with large sand areas in the Western Desert and igeneous-metamorphic rocks formations along the Red Sea, outline and coincide with the "V" structure shown in Figs. 6 and 7. A more detailed geological analysis of the Nile Valley in the Aswan Dam area was made from Landsat 1 data by El Shazly et al. (1974, a, b,) who confirmed the limestone, sandstone and granitic deposits.

Since surface and sub-surface soil moisture can lower microwave brightness temperatures in the salt deserts (Ulaby et al., 1975) a literature search was

made of Egypt with the hope of finding some evidence of sub-surface water seepage from prominent surface water systems such as the Nile or Lake Nasser.

Figs. 10(a) through (d) show the pre-and flood stage of the Lake Nasser Reservoir in 1969 on Nimbus 3 and Landsat 2 images, respectively. A New York Times article by Tanner, 1975 reported that Lake Nasser had been filling up more slowly than expected since 1969 and that only 5 to 6 of 12 available hydroelectric turbines were being utilized in the Aswan Dam due to the lack of water storage. Drs. Farouk El Baz and Abdel-Hady (1975) confirmed the possibility that underground water seepage could occur in the extensive Egyptian limestone and sandstone deposits in the Lake Nasser and Nile Valley region. Surface drilling would be attempted in 1976 in Egypt to measure the extent of water loss.

MICROWAVE PHYSICS RELATIONSHIPS

Previous field work by Edgerton and Trexler, 1970, Kennedy et al., 1966, and later by Edgerton et al., 1973 using a truck-mounted microwave-sensing equipment (Fig. 11), showed that limestone had a low computed and measured brightness temperature (high dielectric constant) when compared with other minerals of lower dielectric constants (high brightness values) (Fig. 12). Note the emissivity decreases more rapidly for the Brewster angle ($>60°$) resulting in a drop in brightness values. The dielectric constant of a material

is defined as the ratio of the capacitance of a condenser filled with the material to the capacity of the condenser when a vacuum exists between its plates (Oberste-Lehn, 1970).

The dielectric constants of selected solid rocks measured at 35 GHz can range from 2 to 10 (Peake, 1967, Campbell and Ulrichs, 1969, Peake and Oliver, 1971). The following tables contain a partial list of the physical characteristics of ground materials relevant to this study (Clark, ed., 1966, Peake, 1967, Edgerton and Trexler, 1970, Ingersoll, 1954, Pohn et al., 1974).

Table 1

Surface Materials	Dielectric Constant (Real Part)	Emissivity (at 37 GHz)	Density (gm cm^{-3})	Porosity (%)
Desert Sand (quartz, dry. med. fine)	2.9	0.93	1.4-1.93	39-46%
Sandstone	4.2-4.8	0.93	2.2-2.7	0.7-20%
Granite	4-5.3	0.90	2.5-2.8	0%
Limestone	6-8.9	0.75	2.65-2.8	0.5-5%

Table 2

Surface Materials	Thermal Inertia (cal cm^{-2} °C $sec^{-½}$)	Thermal Conductivity (cal cm^{-1} sec^{-1} $°C^{-1}$)
Desert Sand	0.01 -0.02	0.00063
Sandstone	0.030-0.058	0.0062
Granite	0.036-0.066	0.0065
Limestone	0.04 -0.06	0.0048

Table 3

Surface Materials	Thermal Diffusivity (cm^2 sec^{-1})	Volumetric Heat Capacity (cal cm^{-3} $°C^{-1}$)
Desert Sand	0.0020	0.314
Sandstone	0.0113	0.546
Granite	0.0127	0.511
Limestone	0.0081	0.594

The physical constants above which appear to be similar, are enclosed by a bracket. The use of thermal inertia mapping to discriminate geological units in the United States and Oman indicated that limestone, dolomite, sandstone and granite fall in a thermal inertia class interval of 0.03 to 0.06 cal cm^{-2} $°C^{-1}$ $sec^{-½}$. (Pohn et al., 1974, Watson et al., 1971, Rowan et al., 1970,

Watson, 1975, Kahle et al., 1975). Any microwave radiation technique which will better selectively identify any of these minerals within this class interval would be of value (Pohn, 1976).

The following parameters effect the Nimbus 5 ESMR (19.35 GHz) brightness values (T_B), of a smooth desert surface (Moore et al., 1975, Ulaby, 1975):

$$T_B = \tau\,[\epsilon\, T_g + (1-\epsilon)\, T_d] + T_u$$

Where

τ = atmospheric transmittance

ϵ = emissivity

T_g = ground temperature, °K

T_d = downward emitted atmospheric temperature, °K

T_u = upward emitted atmospheric temperature, °K

For two fields of view with different emissivities but the same ground temperature, the difference in T_B is:

$$\Delta T_B = \tau(T_g - T_d)\,(\epsilon_2 - \epsilon_1)$$

For a dry desert atmosphere, a ground temperature of 310°K, $\tau \approx 0.95$ and $T_d \approx 10$°K, the emissivity is:

$$\epsilon = 1 - \left(\frac{\sqrt{K} - 1}{\sqrt{K} + 1} \right)^2$$

Where K is the dielectric constant.

	Limestone	Sand
Thus: Dielectric Constant:	8.4	2.9
Emissivity :	0.763	0.932

these emissivities give:

Sand: $T_B = 285°K$

Limestone: $T_B = 237°K$

$\Delta T_B = 48\ °K$

The effect of roughness is minimal for a high emissivity material such as sand but roughness in limestone, a lower emissivity material, may warm the T_B by 20°K or more at 19.35 GHz.

From the basic thermodynamic relationship:

Emissivity = 1-Reflectivity

The reflectivity of a rough surface is smaller than a smooth surface since multiple reflections tend to reduce the total amount of incident radiation reflected. Therefore, the emissivity is greater and the T_B value is warmer. Conversely, high soil moisture content can cause an increase in dielectric constant which results in higher reflectivity or lower emissivity, causing the T_B to decrease. A one percent change in soil moisture content can result in a 4°K change in brightness temperatures (Edgerton et al., 1973).

NILE DELTA - NILE RIVER VALLEY

An excellent cloud-free visible picture (0.5 to 0.7 μm) of the Nile Valley was taken on 23 October 1974 by NOAA 2 VHRR (1 km ground resolution) (Fig. 13). Note the darker heart-shaped region to the southwest of the present Nile Delta which I labelled the "Old Nile Delta". This area according to a hypothesis of the "Urnil", described by Hanter, 1975, was the region where the Nile River exited to the Mediterranean Sea at 29°E, southwest of Alexandria and may have produced an "old" delta, which consists of fluvial and fluvio-marine sediments deposited during lower and middle Miocene period. This sand and shale region which logically could have moved eastward according to current theory to the present delta location, appears warmer in all the Nimbus 5 and 6 ESMR analyses, to be discussed later. Figures 14, 15 and 16 which cover the Nile Delta show an ONC H-5, 1:1 million base map for reader reference, a NOAA 4, VHRR (10.5 to 12.5 μm) (1 km resolution) day, unrectified thermal IR map of 28 June 1975, and a typical Landsat 1, band 7 (0.8 to 1.1 μm) (80 meter resolution) picture of the region. The irrigated farmland in the Delta which extends from Port Said westward to Rosetta and southward to Cairo, appears 4° to 8°K cooler in the IR (Fig. 15) than the nearby desert sand. A wedge of cooler T_B values indicating high soil moisture in the Delta is also shown on Nimbus 5 THIR (11 μm) day, on 16 July 1974 (Fig. 17). The Red Sea hills and mountains of Jordan and Saudi Arabia are generally the warmest (> 315°K),

followed by large portions of the Western Desert (310° to 315°K) and the coastal strip and Nile Valley (<310°K). The water-land interface shows up well in the daytime but there is little coastal, hill or low-land definition at night (293° to 303°K).

THERMAL INERTIA RELATIONSHIPS

The thermal inertia of a material is determined by its volumetric heat capacity, thermal conductivity, thermal diffusivity, specific heat and density. Figure 19 shows the variations of surface temperature as a function of thermal inertia. Optimum surface heating and cooling occurs at 1:30 pm and 2:30 am. The temperature variations are caused by atmospheric cooling and heating at 35°N, heat loss by thermal emission and heat gain by solar energy absorption (Watson et al., 1971, Smith, (ed), 1974). The greater the diurnal surface temperature variation of a material, the smaller the inferred thermal inertia and conversely the smaller the temperature variation the larger the thermal inertia (Schutt, 1975, Price, 1976).

A previous study by Pohn et al., 1974, used Nimbus 3 High Resolution Infrared Radiometer (HRIR) (0.8 to 1.1 μm) day-time data for measuring surface reflectivity and Nimbus 4 THIR (11 μm) data for day-night temperature differences to derive a thermal inertia map of geological units in Oman. A similar visible band (MSS-7, 0.8 to 1.1 μm) from Landsat 1, on 9 November 1972

was used in this study to obtain space albedo over the Lake Nasser region and Nimbus 5 THIR for day-night differences. The Landsat 1, 80 meter resolution elements were averaged to 1 km elements in order to permit comparison with the larger scan spots covered by the THIR data.

Space reflectivity (R_7), from MSS 7, on Landsat 1 was derived as follows: (Otterman & Fraser, 1976)

$$R_7 = \frac{\pi N_7}{S_7 \cos \theta_o}$$

$$R_7(\%) = 1.3795 \times C_7$$

where:

N_7 = nadir radiance

S_7 = solar constant for MSS 7

θ_o = sun zenith angle

C_7 = Landsat digital count for MSS 7

A one km element represents an average of 16 columns and 12 rows of the full resolution (80 meter) Landsat digital data printout.

Figures 19 and 20 show the Landsat 1, MSS 7 image and the 1 km averaged Cal-Comp line drawn analysis for 9 November 1972, respectively. Large limestone areas indicated by space reflectivities of 50 to 65% are shown to the left of column 1600 (top) while the Nubian sandstone (greytone) and granite areas are 35 to 45% and $< 35\%$, respectively. Figures 21 and 22 are included to

show the large limestone units described by El Shazly et al., 1974, for the same Landsat picture. Otterman and Fraser, 1976 had reported space reflectivities of 54 to 57% for Libyan desert sand from Landsat 2, MSS 7. A laboratory spectrographic analysis of Sinai desert sand indicated 49 to 54% total diffusive reflectances for this wavelength (Fig. 23) which makes the above space reflectivities more credible.

Day-night temperature differences for 16 July 1974 were obtained using Nimbus 5, 11 μm data, under clear sky conditions (Fig. 24). A radiosonde run at Aswan, Egypt on 16 July 1974, 1200 GMT, (Fig. 25) indicated a dry atmosphere and therefore no atmospheric corrections were made to the 11 μm analyses. The southern Sinai Peninsula, the Red Sea hills, mountains of Jordan and Saudi Arabia and portions of the Western Desert show the largest diurnal temperature difference (20° to 35°K), while the limestone deposits in the Nile Valley and coastal deserts indicate 5° to 20°K. The Red Sea - Mediterranean Sea, and Nile Delta show a smaller ΔT_B of 3° and 5° to 10°K, respectively.

Pohn et al., 1974, developed a least squares fit of thermal inertia versus day-night temperature difference for different albedos (Fig. 26). By overlaying a portion of the day-night temperature difference chart (Fig. 24) on the reflectivity chart of the Lake Nasser region (Fig. 20), the following range of thermal inertia (cal cm^{-2} °C $sec^{-½}$) was derived:

Table 4

	Space Reflectivity	Day-night 11 μm T_B differences	Thermal Inertia
Granite	20% - 35%	20° - 25°K	0.038 - 0.058
Sandstone	35% - 45%	16° - 20°K	0.040 - 0.060
Limestone	50% - 65%	12° - 16°K	0.035 - 0.058

The thermal inertia values for the 3 materials above range from 0.035 to 0.060 cal cm^{-2} °C $sec^{-½}$ which is in agreement with published values in the literature, shown in Table 2. The use of microwave data to further differentiate these materials will be discussed in the next section.

MICROWAVE AND INFRARED BRIGHTNESS TEMPERATURE RELATIONSHIPS

In order to compare the Nimbus 5 ESMR (19.35 GHz) and THIR (11 μm) brightness temperatures, four crossections, (Box 1, 2, 3, 4) were drawn through the area of interest (Figs. 27, 28, 29). Coincidental data was used for the night of 16 July 1974 but a 10 day separation occurred for the day comparison (July 16 to July 25, 1974) due to satellite instrument processing problems.

Individual Landsat 1 and 2 frames with box area limits in black are shown for ready reference of geological formations (Figs. 30, 31, 34, 37, 40).

Averages of IR and ESMR brightness values were plotted within a half degree of latitude from 24°N in the 4 regions to 29° 30°N using the respective Nimbus grid print map (1:2 million, Mercator). The IR brightness data was uncorrected due to negligible atmospheric moisture content.

An analysis of the crossectional data in Figs. 32, 33, 35, 36, 38, 39, 41, 42 show the following relationships:

1. The Nimbus 5, 11 μm brightness values over the igneous-metamorphic rocks in the Red Sea hills and southern Sinai peninsula were the warmest (320°K ± 2°K) during the day while the cooler nighttime T_B gradients appear rather flat (296° ± 4°C) over most ground surfaces.

2. The Nimbus 5 ESMR, 19.35 GHz brightness values were warmest (270° to 282°K, day) (260° to 265°K, night) over the igneous-metamorphic rocks and sandstone and coolest (250° to 263°K day) (240° to 251°K, night) over limestone. The average day or night difference between the above materials was approximately 15° to 30°K.

3. The THIR-ESMR brightness difference is largest for the Red Sea (> 100°K), followed by limestone (48° to 52°K, day) (42° to 45°K, night), igneous-metamorphic rocks (38° to 47°K, day) (26° to 40°K, night) and sandstone (35° to 41°K, day) (28° to 37°K, night). A second areal average of THIR-ESMR brightness temperature difference between limestone and igneous-metamorphic rocks-sandstone was 14°K night and 10°K, day. Sandstone and igneous-

metamorphic rocks have similar dielectric constants, density, thermal inertia but different porosity and surface roughness (Tables 1 and 2).

Nimbus 6 ESMR (37 GHz) data were also analyzed for selected days in July and August 1975. The dotted "V" structure in the horizontal polarization data of 28 July 1975 (Fig. 43) appears cooler (T_B : $< 250°$ to 260°K) while the sandstone and igneous-metamorphic rocks are warmer (T_B : 270° to $> 300°$K). The cool "V" structure in the vertical polarization data appears to be $< 280°$ to 290° while the sandstone and granitic hilly areas are warmer: 300° to 318°K. (Fig. 44). When horizontal polarization data is subtracted from the vertical polarization data on 14 August 1975, large 70° to 80°K T_B differences occur over the sea while 40° to 50°K T_B differences occur in the Western Desert and the An Nafud Desert (Fig. 45). These differences may have been caused by scattering from smooth sand dune surfaces which have similar scattering characteristics to that of the 10° to 15° slope of a "low wind" sea surface (Peake, 1975). A similar effect was noted in the sands of the Rub Al Khali Desert (Empty Quarter) of southern Saudi Arabia (Fig. 59). Smaller T_B differences ($< 20°$K) appear in the hilly regions bordering the Red Sea, the Sinai Peninsula and Israel.

SAUDI ARABIA

Several Nimbus 5 and 6 ESMR and THIR orbits over Saudi Arabia were selected in order to study the patterns of microwave and infrared brightness temperatures

over an adjacent cloud-free desert-mountainous region. This area does not have an established river system flowing through it like the Nile in Egypt which could have underground water seepage and possibly change the surface microwave emissivity patterns of the desert.

Figure 46 (a) shows an excellent U.S. Air Force Defense Meteorological Satellite Program DMSP visible picture of the region (Dickinson et al., 1974) on 14 Feb. 1975 while (b) indicates the main geological features as described by Powers et al., 1966.

The Arabian Shield consists mainly of igneous and metamorphic rocks which have been tectonically stable since the Precambrian period and locally overlain by Cenozoic volcanics, and Quaternary alluvial and Eolian sediments (dark and light-tones) (Blodget, 1971).

The Interior Homocline falls away from the shield (Fig. 47) and consists of eroded limestone, dolomite, shale and sandstone which appear in a stripe-pattern in the central Arabian arch area. Extensive low lying wind-blown Eolian sand occur in the An Nafud and Rub Al Khali Deserts, to the north and south respectively. The Hadramawt Plateau along the south coast is a high, dissected plateau with a dominant east-west drainage system make up of limestone, shale and marl strata. Fig. 48 shows all areas containing large units of limestone obtained from the U.S. Geological Survey-Arabian

American Oil Co., 1963, Geologic map of the Arabian Peninsula; U.S. Geological Survey Misc. Geol. Inv. Map I-270A. Note the similarity in the light grey areas in the Interior Homocline (central portion) and south coast of Saudi Arabia in the Nimbus 5 ESMR image (Fig. 49) and the limestone deposits in Fig. 48.

Cool microwave brightness temperatures at night, (240° to 260°K) on 18 Sept. 1973 clearly outline these areas (Fig. 50). The Arabian Shield (granitic rock) is progressively warmer (>260° to 270°K) and the Rub Al Khali Desert is the warmest (>270°K). However in a day analysis over the same area on 24 Sept. 1973 (Fig. 51) a 2 to 4° of longitude-wide strip of hills in the Arabian Shield from 40°E to 45°E indicate warmer T_B values (280° to >290°K) than the sands of the Rub Al Khali Desert. A similar pattern showing this temperature reversal is found on 16 July 1974, day (Fig. 53). A distinctively warm T_B pattern (>270°K) night, >280°K, day) was found over the Kuwait oilfields (McCaslin, 1975) in all Nimbus 5 ESMR analyses. This was an area mixed with chalk, limestone and quartz gravel, marly sandstone, sandy marl, sandy limestone and calcareous silty sandstone (Fig. 48) (Powers et al., 1966.) Fig. 52 which shows another view of the region at night on 8 March 1975 indicates a pattern similar to Fig. 50 but overall ESMR brightness values are lower by 10° to 20°K due to seasonal temperature changes. Analyses of Nimbus 5 ESMR and THIR (Fig. 53, 54) for 16 July 1974, day were made,

on which a half degree latitude crossection through the Arabian Shield, the Interior Homocline and Platform was performed (Fig. 55). Large differences (52° to 61°K) were found between the 11 μm and ESMR T_B values over limestone and dolomite hills while smaller differences (38° to 43°K) were found over igneous-metamorphic rocks and sandstone. The limestone-dolomite structures in the Interior Homocline are generally 20° to 30°K cooler than the granitic rocks in the Arabian Shield and 10° to 20°K cooler than the eolian sand in the Rub Al Khali and An Nafud Desert at 19.35 GHz.

Nimbus 6 ESMR (37 GHz) vertical and horizontal polarization data for 16 August 1975 (Fig. 56, 57) showed a similar night temperature pattern as did the Nimbus 5 analyses (Fig. 50, 52) i.e., the eolian sand appeared warmest in both polarizations. When horizontal was subtracted from vertical polarization data, large 40° to 60°K T_B values were noted to be located over the sands of the Empty Quarter (Fig. 58, 59). This may be caused by a surface scattering effect of the sand dunes at 37 GHz (Peake, 1975).

CONCLUSION

The microwave brightness temperatures from Nimbus 5 and 6 ESMR and THIR have been used to identify large units of limestone-dolomite against a background of igneous-metamorphic rocks, sandstone and eolian sand in the Middle Eastern deserts. Nimbus G, Seasat and Shuttle to be launched

in the 1978-81 time period will carry multi-frequency passive and infrared radiometers which hold great promise for further geological exploration from space.

ACKNOWLEDGMENTS

The author wishes to acknowledge the assistance of Dr. Robert Fraser and Dr. O. Bahethi in processing the Landsat data and to Dr. Joseph Otterman for initiating this study over the deserts of the Middle East.

REFERENCES

Allison, L. J., E. B. Rodgers, T. T. Wilheit, and R. W. Fett, 1974: "Tropical Cyclone Rainfall as Measured by the Nimbus 5 Electrically Scanning Microwave Radiometer," Bulletin of the American Meteorological Society, Vol. 55, No. 9, 1074-1089.

Allison, L. J., E. B. Rodgers, T. T. Wilheit and R. Wexler, 1975: "A Multisensor Analysis of Nimbus 5 Data Recorded on January 22, 1973", NASA TN D-7911, Goddard Space Flight Center, pp. 43.

Blodget, H. W., 1971: "A Comparative Geologic Study of Spacecraft and Aircraft Imagery," NASA X-644-71-204, Goddard Space Flight Center, pp. 56.

Blodget, H. W., G. F. Brown and J. G. Moik, 1975: "Geological Mapping in Northwestern Saudi Arabia Using Landsat-Multispectral Techniques," NASA X-923-75-206. Goddard Space Flight Center, pp. 21.

Campbell, M. J. and J. Ulrichs, 1969: "Electrical Properties of Rocks and their Significance for Lunar Radar Observations," Journal of Geophysical Research, Vol. 74, No. 25, 5867-5881.

Cihlar, J. and F. T. Ulaby, 1974: "Dielectric Properties of Soils as a Function of Moisture Content," RSL Tech. Report 177-47, University of Kansas Center for Research, Lawrence, Kansas, pp. 61.

Clark, S. P. (ed.), 1966: "Handbook of Physical Constants," Memoir 97, Geological Society of America.

Dickinson, L. G., S. E. Boselly, W. S. Burgmann, 1974: "Defense Meteorological Satellite Program (DMSP) User's Guide," Hqtrs. Air Weather Service, Scott AFB, Illinois, 62225, pp. 109.

Dr. Farouk El Baz and M. S. Abdel-Hady, 1975: Private Correspondence.

Edgerton, A. T. and D. T. Trexler, 1970: "Passive Microwave Techniques Applied to Geologic Problems," Final Report 1361-R-1, Aerojet-General Corporation, El Monte, Calif., pp. 100.

Edgerton, A. T., F. Ruskey, D. Williams, A. Stogryn, G. Poe, D. Meeks, O. Russell, 1973: "Microwave Emission Characteristics of Natural Materials and the Environment," Final Report 9016R-8, Aerojet-General Corporation, Azusa, Calif., pp. 110.

El Shazly, E. M., M. A. Abdel-Hady, M. A. El Ghawaby, I. A. Kassas, 1974(a): "Geologic Interpretation of ERTS-1 Satellite Images for West Aswan Area, Egypt," in 9th Int'l Symp. on Remote Sensing of Envir.; Ann Arbor, Mich., 119-131.

El Shazly, E. M., M. A. Abdel-Hady, M. A. El Ghawaby, I. A. Kassas,: 1974(b): "Geologic Interpretation of ERTS-1 Satellite Images for East Aswan Area, Egypt," in 9th Int'l Symp. on Remote Sensing of Envir.; Ann Arbor, Mich., 105-117.

Hanter, G., 1975: "Contribution to the Origin of the Nile Delta," Paper No. 117 (B-3), 9th Arab Petroleum Congress, of The Secretariat General League of Arab States, pp. 13.

Ingersoll, L. R., 1954: "Heat Conduction with Engineering, Geological and other Applications," University of Wisconsin Press, Madison, Wisconsin, pp. 325.

Issawi, B., 1973: "Nubia Sandstone: Type Section," Geological Notes the American Association of Petroleum Geologists Bulletin, V. 57, No. 4, 741-745.

Kahle, A. B., A. R. Gillespie, A. F. H. Goetz, J. D. Addington, 1975: "Thermal Inertia Mapping," 10th Int'l Symp. on Remote Sensing of Envir.; Ann Arbor, Mich., 1-17.

Kennedy, J. M., A. T. Edgerton, R. T. Sakamoto, and R. M. Mandl, 1966: "Passive Microwave Measurements of Snow and Soil," Tech. Report #2, Aerojet-General Corporation, El Monte, Calif.

Kidder, S. Q., 1976: "Tropical Oceanic Precipitation Frequency from Nimbus 5 Microwave Data," Atmos. Science Paper 248, Colorado State University, Ft. Collins, Col., pp. 50.

Lowman, P. D. and J. A. McDivitt, 1967: "Terrain Photography on the Gemini IV Mission: Preliminary Report," NASA TN D-3982, Goddard Space Flight Center, pp. 15.

McCaslin, J. (ed.), 1975: "International Petroleum Encyclopedia," The Petroleum Publishing Co., Box 1260, Tulsa, Ok. 74101, pp. 480.

McCulloch, A. W., 1972: "The Temperature-Humidity Infrared Radiometer (THIR) Subsystem," in the Nimbus 5 User's Guide, ERTS/Nimbus Project, Goddard Space Flight Center, 11-47.

Meneely, J. M., 1975: "Application of the Nimbus 5 ESMR to Rainfall Detection over Land Surfaces," Final Report E/S No. 1008, Earth Satellite Corp., Wash., D.C., pp. 48.

Merifield, P. M. (ed.), J. Cronin, L. L. Foshee, S. J. Gawarecki, J. T. Neal, R. E. Stevenson, R. O. Stone and R. S. Williams, Jr., 1969: "Satellite Imagery of the Earth," Photogrammetric Engineering, Vol. 35, No. 7, 654-668.

Moore, R. K. (ed.), L. L. Chastant, L. J. Porcello, J. Stevenson and F. T. Ulaby, 1975: "Microwave Remote Sensors," Chapter 9, Vol. 1 of the Manual of Remote Sensing, Edited by F. Janza, American Society of Photogrammetry, Falls Church, Virginia, 399-537.

Nimbus 5 User's Guide, 1972: "The Nimbus 5 Spacecraft System," ERTS/ Nimbus Project, Goddard Space Flight Center, 1-10.

Nimbus 6 User's Guide, 1975: "The Nimbus 6 Spacecraft System," Landsat/ Nimbus Project, Goddard Space Flight Center, 1-10.

Nordberg, W. and R. E. Samuelson, 1965: "Terrestrial Features Observed by the High Resolution Infrared Radiometer," in Observations from the Nimbus 1 Meteorological Satellite, NASA SP-89, Goddard Space Flight Center, 37-41.

Oberste-Lehn, D., 1970: "Phenomena and Properties of Geologic Materials Affecting Microwaves-A Review," Stanford Remote Sensing Laboratory, TR 70-10, Stanford University, Stanford, Calif., pp. 57.

Otterman, J. and R. S. Frazer, 1976: "Earth-Atmosphere System and Surface Reflectivities in Arid Regions from Landsat Multispectral Scanner Measurements," NASA X-911-76-147, Goddard Space Flight Center, Greenbelt, Md., pp. 38.

Peake, W. H., 1967: "The Microwave Radiometer as a Remote Sensing Instrument with Applications to Geology," Notes prepared for a short course on Geologic Remote Sensing, Stanford University, 4-8 Dec., 1967, pp. 34.

Peake, W. H. and T. L. Oliver, 1971: "The Response of Terrestrial Surfaces at Microwave Frequencies," Ohio State University, Columbus, Ohio, Electroscience Lab. Report 2440-7, pp. 255.

Peake, W. H., 1975: Private Correspondence.

Poe, G., A. Stogryn and A. T. Edgerton, 1971: "Determination of Soil Moisture Content Using Microwave Radiometry," Final Report No. 1684FR-1 for DOC Contract No. 0-35239.

Pohn, H. A., T. W. Offield, and K. Watson, 1974: "Thermal Inertia Mapping from Satellite-Discrimination of Geologic Units in Oman," Journal of Research, U.S. Geological Survey, Vol. 2, No. 2, 147-158.

Pohn, H. A., 1976: Private Correspondence.

Pouquet, J., 1968. "Remote Detection of Terrain Features from Nimbus 1 High Resolution Infrared Radiometer Nighttime Measurements," NASA TN D-4603, Goddard Space Flight Center, pp. 8.

Pouquet, J. and E. Raschke, 1968· "A Preliminary Study of the Detection of Geomorphological Features over Northeast Africa by Satellite Radiation Measurements in the Visible and Infrared," NASA TN D-4648, Goddard Space Flight Center, pp. 16.

Pouquet, J., 1969: "Geopedological Features Derived from Satellite Measurements in the 3.4-4.2 and 0.7-1.3 μ Spectral Regions," NASA X-622-69-437, Goddard Space Flight Center, pp. 27.

Powers, R. W., L. F. Ramerez, C. D. Redmond, E. L. Elberg, Jr., 1966: "Geology of the Arabian Peninsula, Sedimentary Geology of Saudi Arabia, U.S. Geological Survey Prof. Paper 560-D, pp. 147.

Price, J., 1976: "Thermal Inertia Mapping, A New View of the Earth," NASA X-913-76-121, Goddard Space Flight Center, pp. 38.

Rowan, L. C., T. W. Offield, K. Watson, P. J. Cannon, R. D. Watson, 1970: "Thermal Infrared Investigations, Arbuckle Mountains, Oklahoma," Geol. Soc. Amer., Bulletin, Vol. 81, 3549-3562.

Rowan, L. C., P. H. Wetlaufer, A. F. H. Goetz, F. C. Billingsley and J. H. Stewart, 1974: "Discrimination of Rock Types and Detection of Hydrothermally Altered Areas in South-Central Nevada by the Use of Computer-Enhanced ERTS Images," Geological Survey Prof. Paper 883, pp. 35.

Sabatini, R., G. A. Rabchevsky and J. Sissala, 1971: "Nimbus Earth Resources Observations," Tech. Report #2 prepared for Goddard Space Flight Center by Allied Research Associates, Inc., Concord, Mass., pp. 256.

Sabatini, R. R., 1975: "Sea-Surface Wind Speed Estimates from the Nimbus 5 ESMR," Final Report, EPRF Tech. Report 3-75 (ESC), Earth Satellite Corp., Wash., D.C., pp. 55.

Said, R., 1962: "The Geology of Egypt," Elsevier Publishing Co., Amsterdam, New York, pp. 377.

Schmugge, T. J., A. Rango, L. J. Allison, and T. T. Wilheit, 1974(a): "Hydrologic Applications of Nimbus 5 ESMR Data," NASA X-910-74-51, Goddard Space Flight Center, pp. 21.

Schmugge, T. J., P. Gloersen, T. T. Wilheit, and F. Geiger, 1974(b): "Remote Sensing of Soil Moisture with Microwave Radiometers," Journal of Geoph. Res., Vol. 79, No. 2, 317-323.

Schnapf, A., 1962: "TIROS 1, 2 and 3 - Design and Performance," Aerospace Engineering, Vol. 21, No. 6, 32-43.

Schutt, J., 1975: "An Approach to Thermal Property and Temperature Determination from Spacecraft," NASA X-923-75-84, Goddard Space Flight Center, pp. 31.

Smith, S. R. (ed.), 1974: "Applications Explorer Missions (AEM), Mission Planners Handbook," Goddard Space Flight Center, pp. 160.

Tanner, H., 1975: "Debate Flares in Egypt over Aswan Dam," New York Times, May 4, 1975.

Ulaby, F. T., L. F. Dellwig, T. J. Schmugge, 1975: "Satellite Microwave Observations of the Utah Great Salt Lake Desert," NASA X-913-75-252, Goddard Space Flight Center, pp. 36.

Ulaby, F. T., 1975: Private Correspondence.

Vickers, R. S. and G. C. Rose, 1971: "The Use of Complex Dielectric Constant as a Diagnostic Tool for the Remote Sensing of Terrestrial Materials," AFCRL-71-0438, Colorado State U., Ft. Collins, Col., pp. 39.

Watson, K., L. C. Rowan and T. W. Offield, 1971: "Application of Thermal Modeling in the Geological Interpretation of IR Images," 7th Int'l. Symp. on Remote Sensing of Environment, Ann Arbor, Mich; U. of Mich., Vol. 3, 2017-2041.

Watson, K., 1975: "Geologic Applications of Thermal Infrared Images," Proc. of the IEEE, 128-137.

Wilheit, T. T., 1972: "The Electrically Scanning Microwave Radiometer (ESMR) Experiment." The Nimbus 5 User's Guide, R. R. Sabatini, ed., ERTS/Nimbus Project, Goddard Space Flight Center, 59-105.

Wilheit, T. T., M. S. U. Rao, T. C. Chang, E. B. Rodgers, J. S. Theon, 1975: "A Satellite Technique for Quantitatively Mapping Rainfall Rate Over the Oceans," NASA X-911-75-72, Goddard Space Flight Center, pp. 28.

Wilheit, T. T., 1975: "The Electrically Scanning Microwave Radiometer (ESMR) Experiment," The Nimbus 6 User's Guide, Landsat/Nimbus Project, Goddard Space Flight Center, 87-108.

Wilheit, T. T., J. S. Theon, W. E. Shenk, L. J. Allison and E. B. Rodgers, 1976: "Meteorological Interpretations of the Images from the Nimbus 5 Electrically Scanned Microwave Radiometer," Journal of Applied Meteorology, Vol. 15, No. 2, 166-172.

World Meteorological Organization, 1963: "Reduction and Use of Data Obtained by Meteorological Satellites," Tech. Note 49, pp. 59.

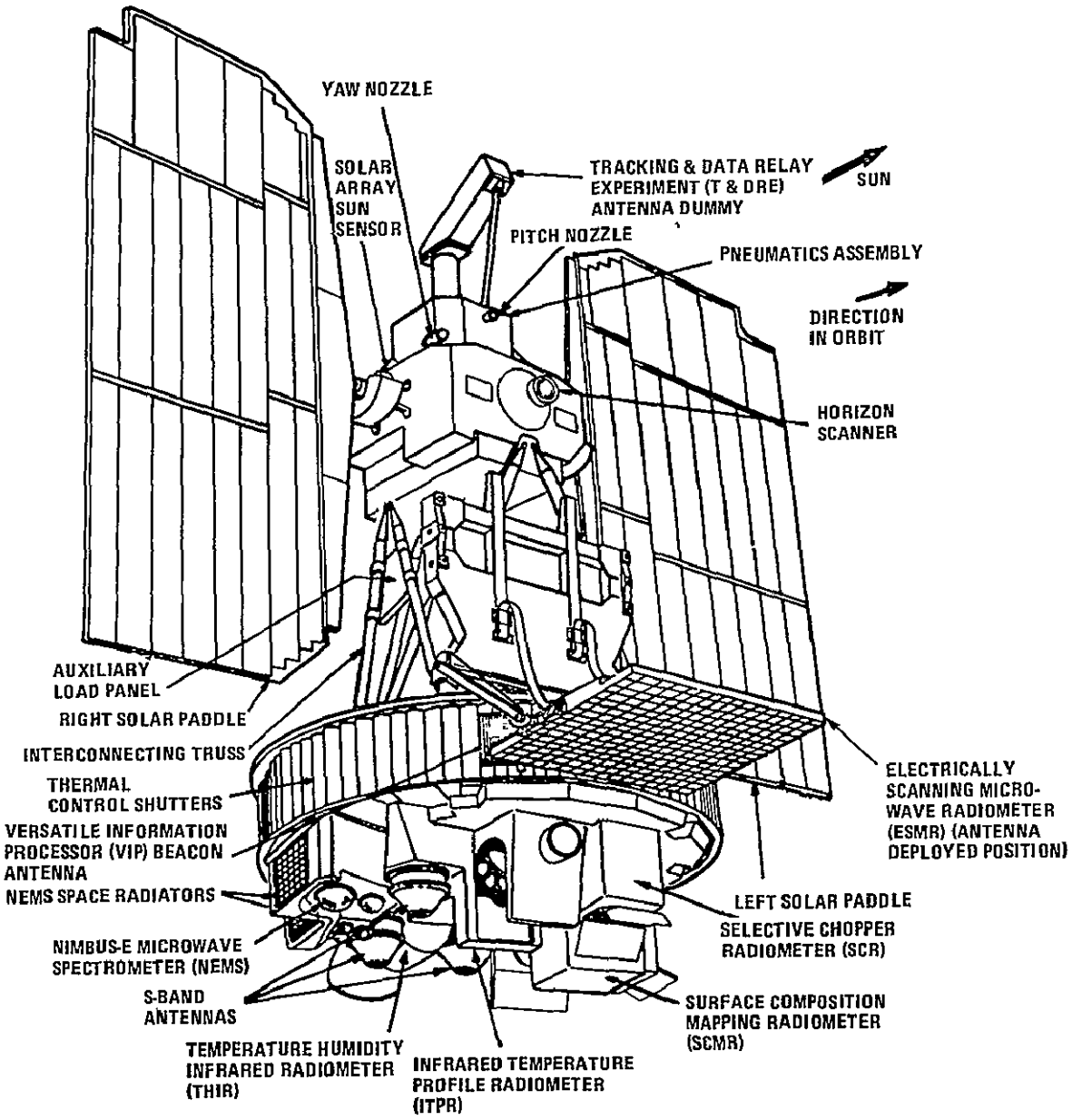

Figure 1a. Nimbus 5 spacecraft with associated experiments

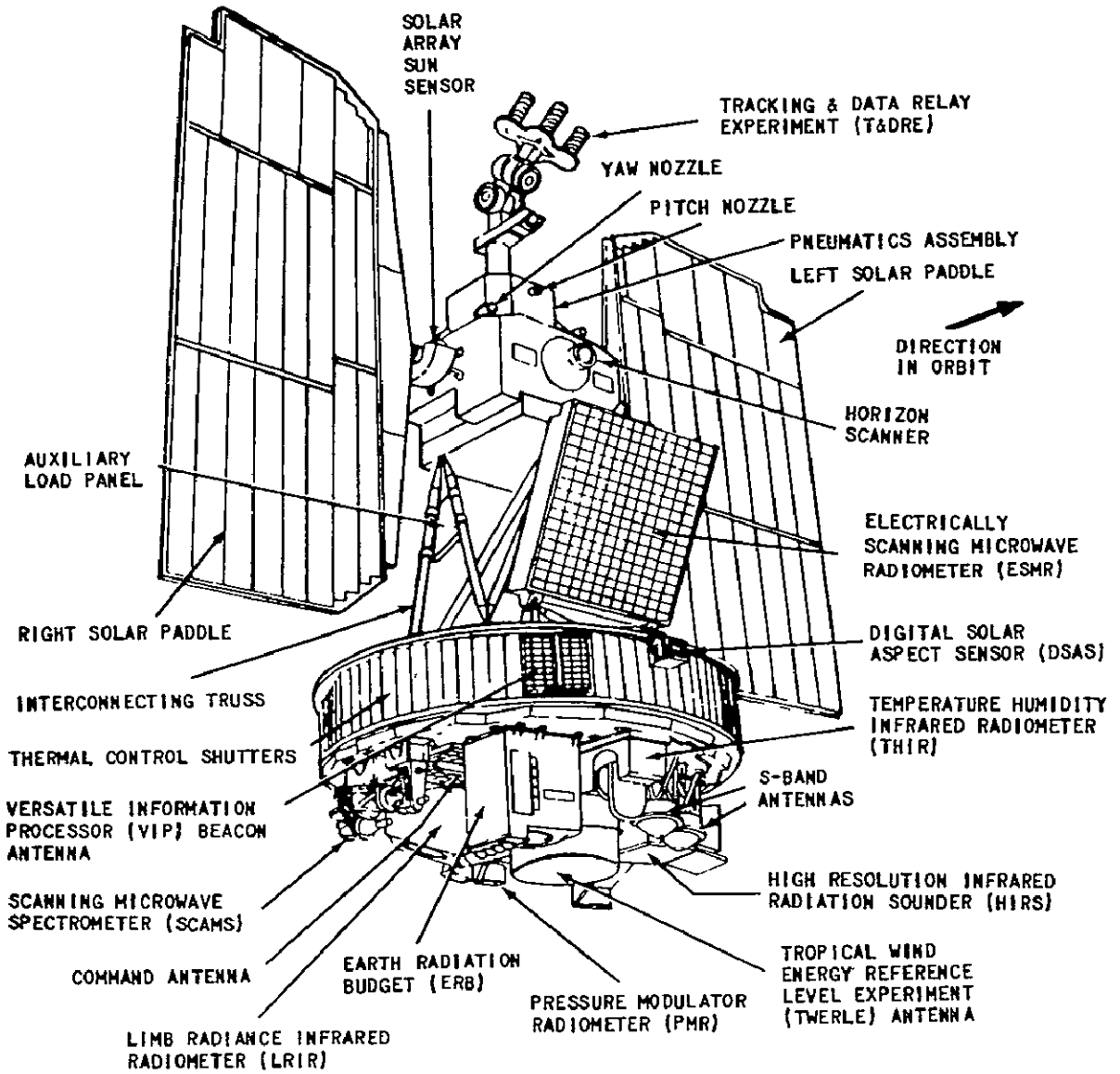

Figure 1b. Nimbus 6 spacecraft with associated experiments

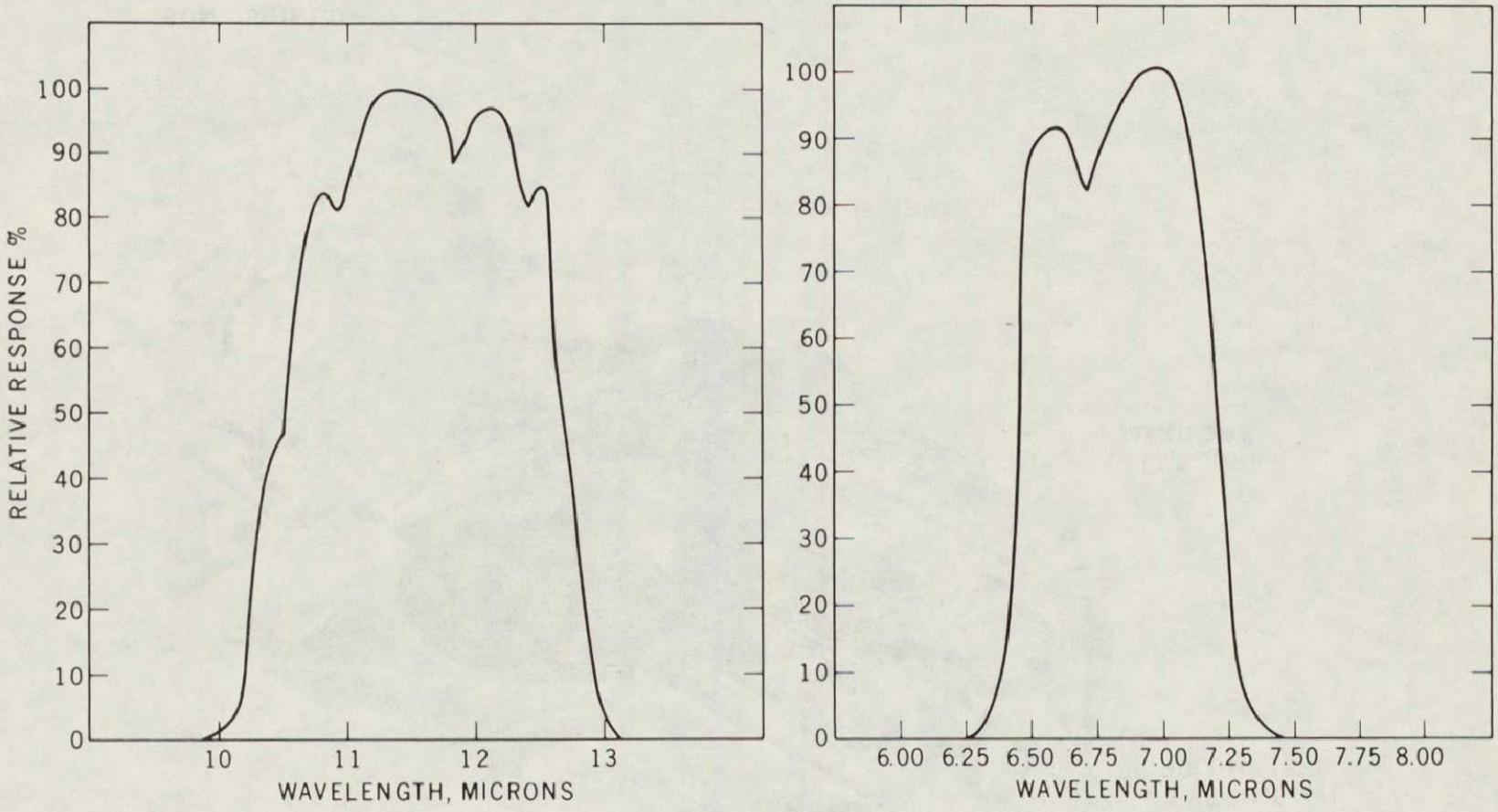

Figure 2. Relative spectral response of the 11.5 μm and 6.7 μm channel of Nimbus 5, THIR

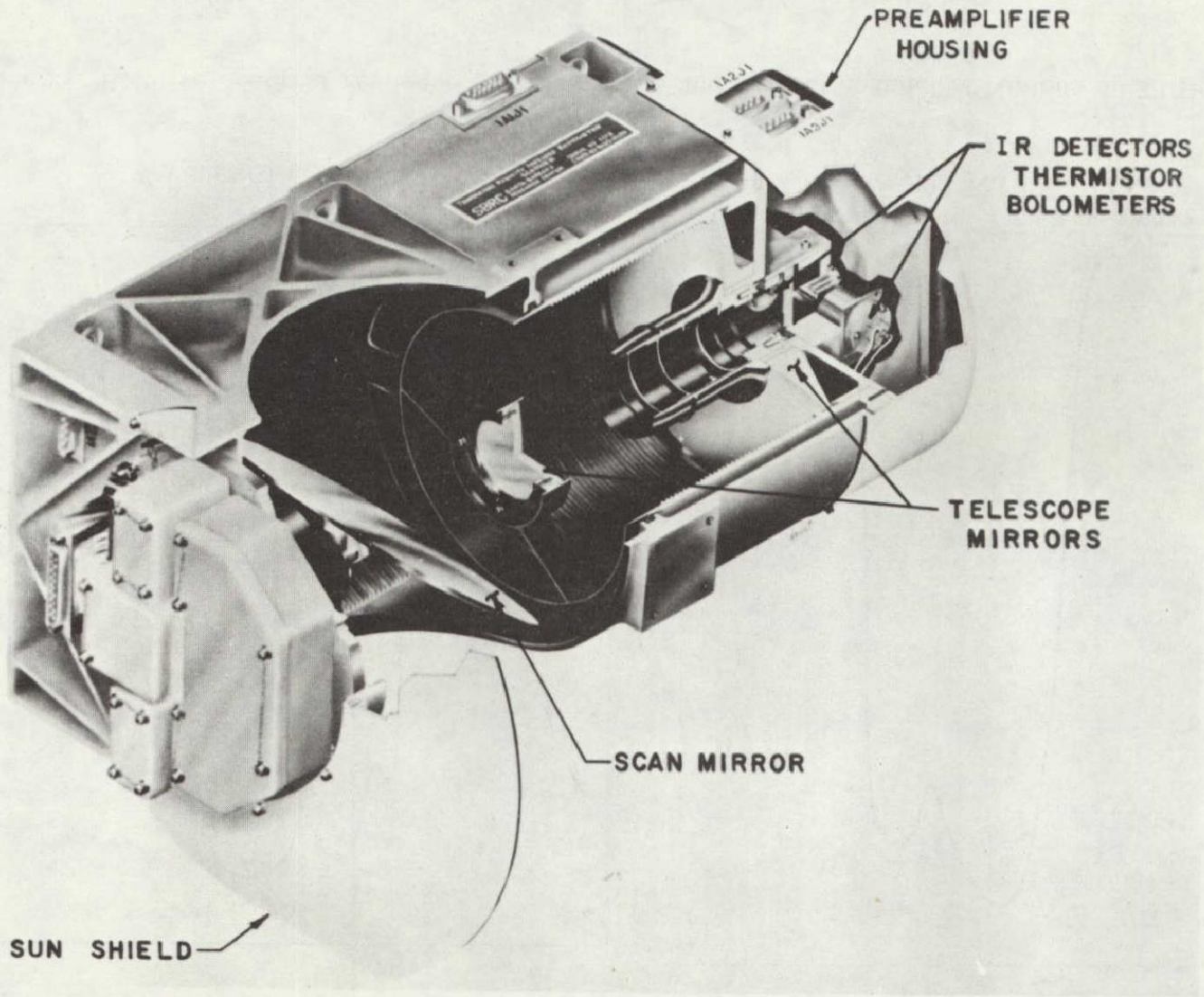

Figure 3. Cut-away of the Nimbus 5 THIR

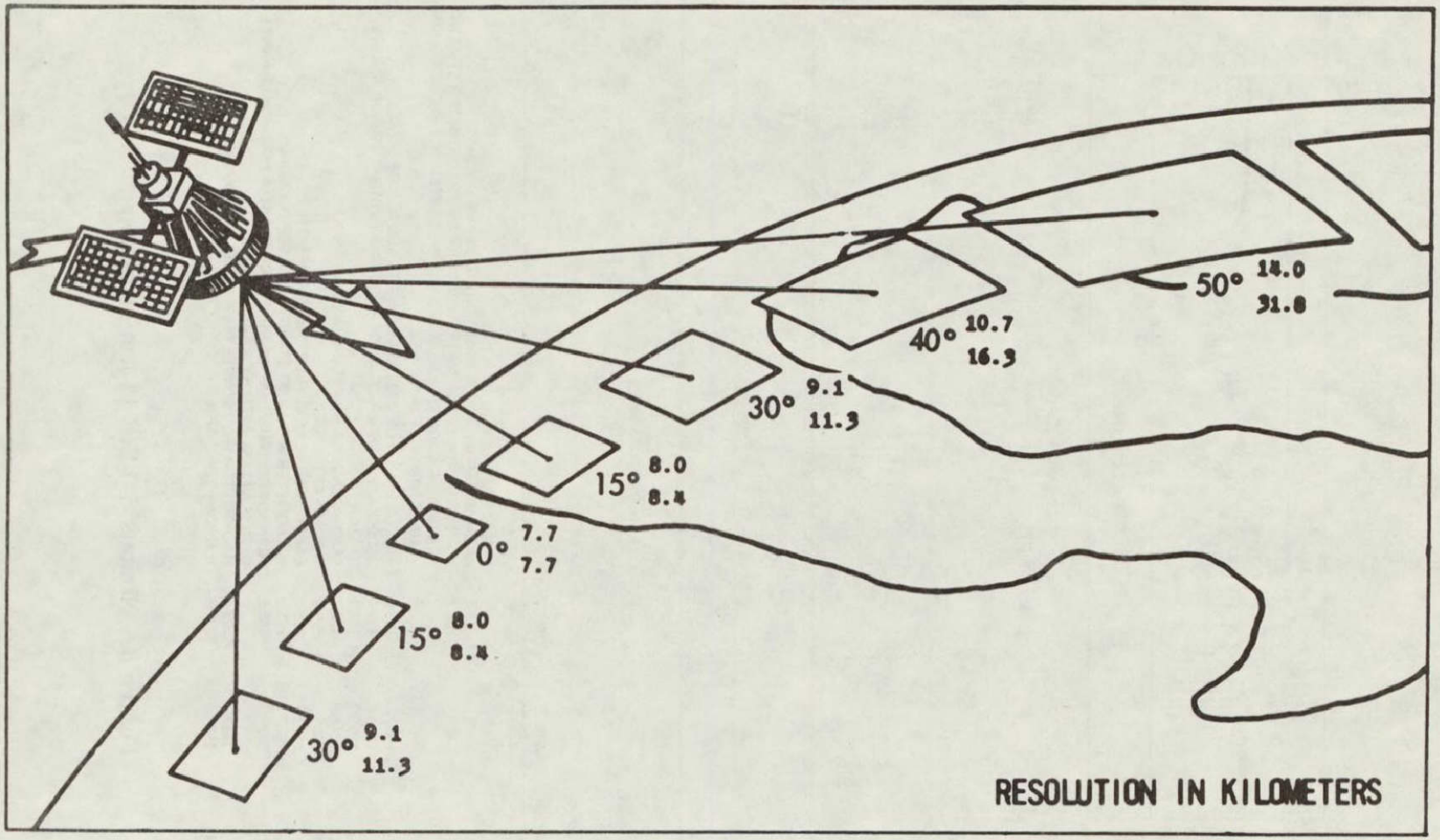

Figure 4. Scanning pattern of the Nimbus 5 THIR, 11 μm (Surface resolution in km at varied nadir angles)

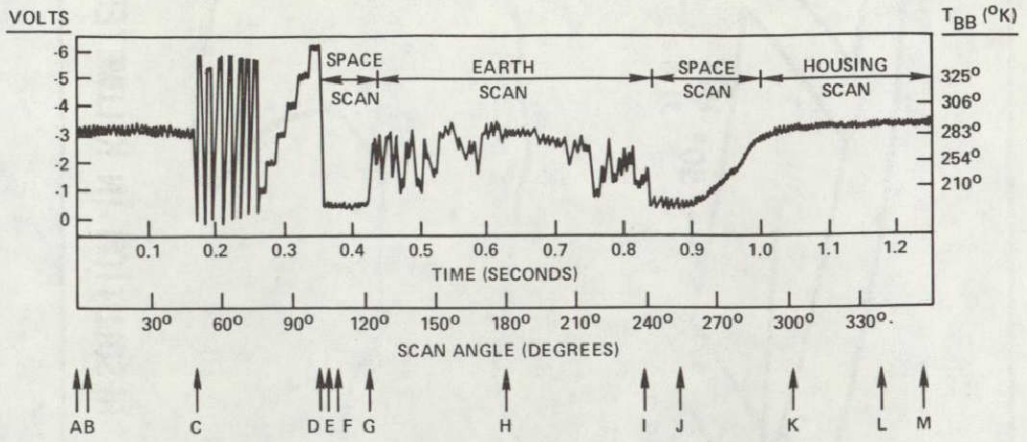

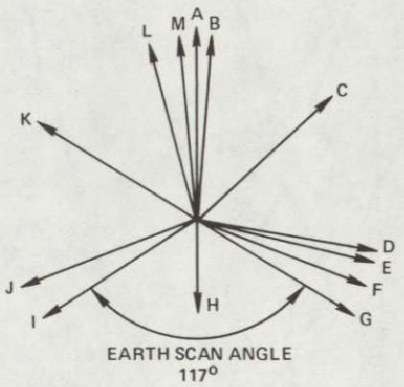

LEGEND

REFERENCE LETTER	ANGLE (DEGREES)	TIME (MSEC)	EVENT
A:	0°	0	SPACECRAFT ZENITH
B:	5°	17.4	RADIOMETER IFOV JUST STARTING TO LEAVE HOUSING.
C:	48°	166.7	SCAN MIRROR POSITION PIP NO. 1 OCCURS AND RADIOMETER SYNC WORD AND CALIBRATION SIGNAL SEQUENCE IS STARTED. 6.7 MICRON CHANNEL GAIN RETURNED TO NORMAL.
D:	100°	347.5	RADIOMETER IFOV JUST STARTING TO SEE ALL OF SPACE.
E:	103.5°	359.4	CALIBRATE SIGNAL SEQUENCE ENDS AND RESTORE PERIOD STARTS.
F:	110.7°	384.4	RESTORE PERIOD ENDS
G:	121.5°	422.2	EARTH SCAN PERIOD BEGINS (600-NMI ORIBT)
H:	180°	625.0	SPACECRAFT NADIR
I:	238.5°	828.8	EARTH SCAN PERIOD ENDS (600-NMI ORBIT)
J:	250°	868.9	RADIOMETER IFOV JUST STARTING TO SEE HOUSING
K:	302°	1048.5	SCAN MIRROR POSITION PIP NO. 2 OCCURS AND 6.7 MICRON CHANNEL GAIN IS ATTENUATED BY A FACTOR OF 3.
L:	345°	1197.9	RADIOMETER IFOV COMPLETELY FILLED BY HOUSING
M:	355°	1232.6	RADIOMETER Z-AXIS

Figure 5. Nimbus 5 THIR 11 μm scan sequence

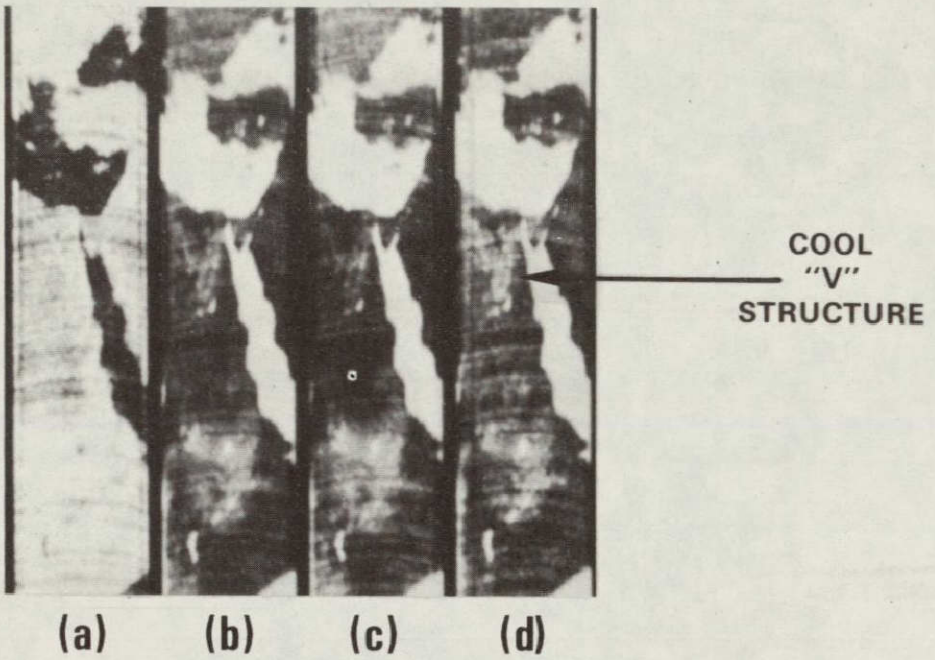

Figure 6. Nimbus 6 ESMR 37 GHz, orbit 618 (day), 28 July 1975, facsimile picture. a) Difference of c) and d); b) Average of c) and d); c) Vertical polarization; d) Horizontal polarization

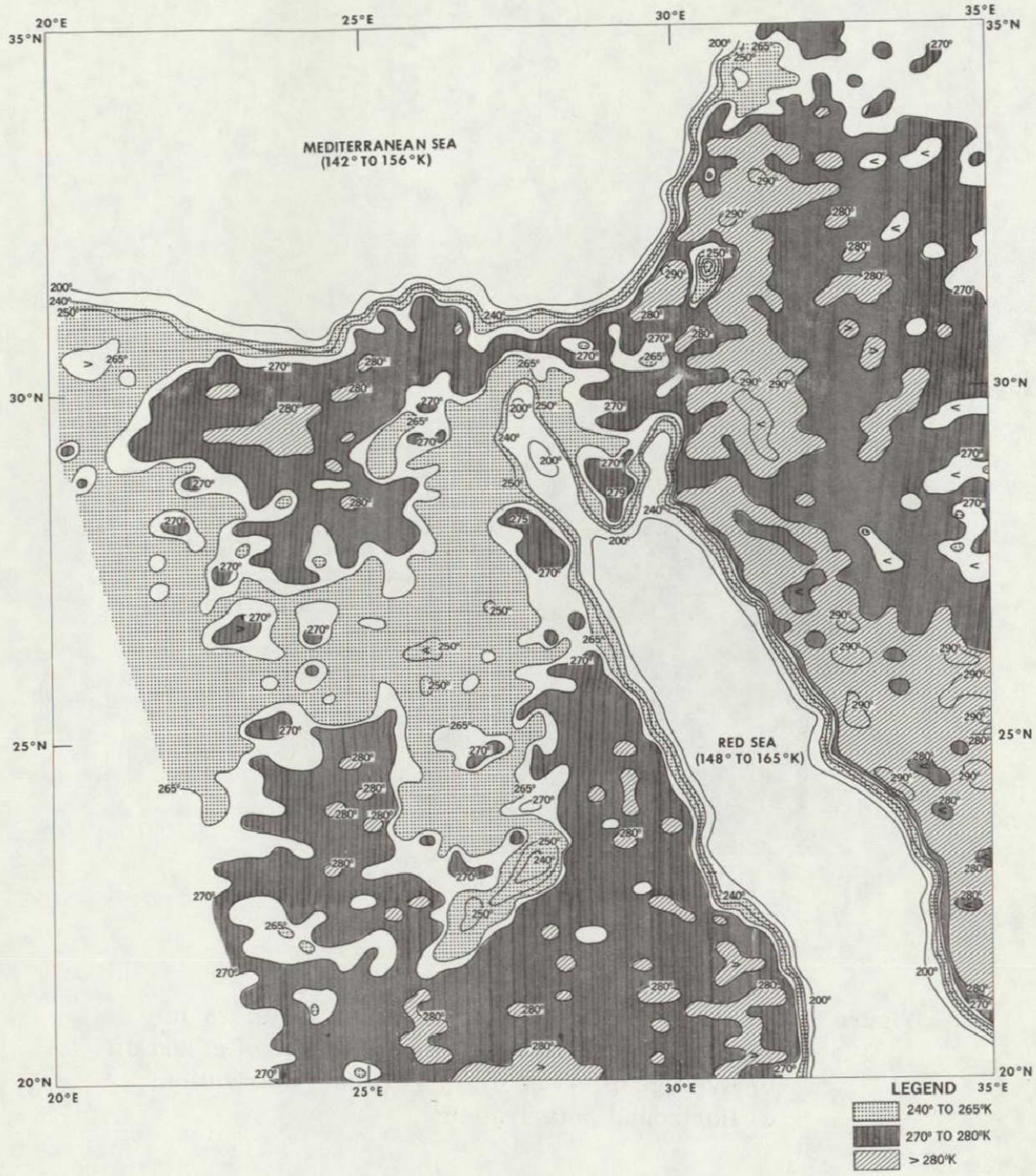

Figure 7. Nimbus 5 ESMR 19.35 GHz, orbit 3813 (day), 21 Sept. 1973, horizontal polarization, analysis of computer - produced grid print maps, 1:2 million, Mercator

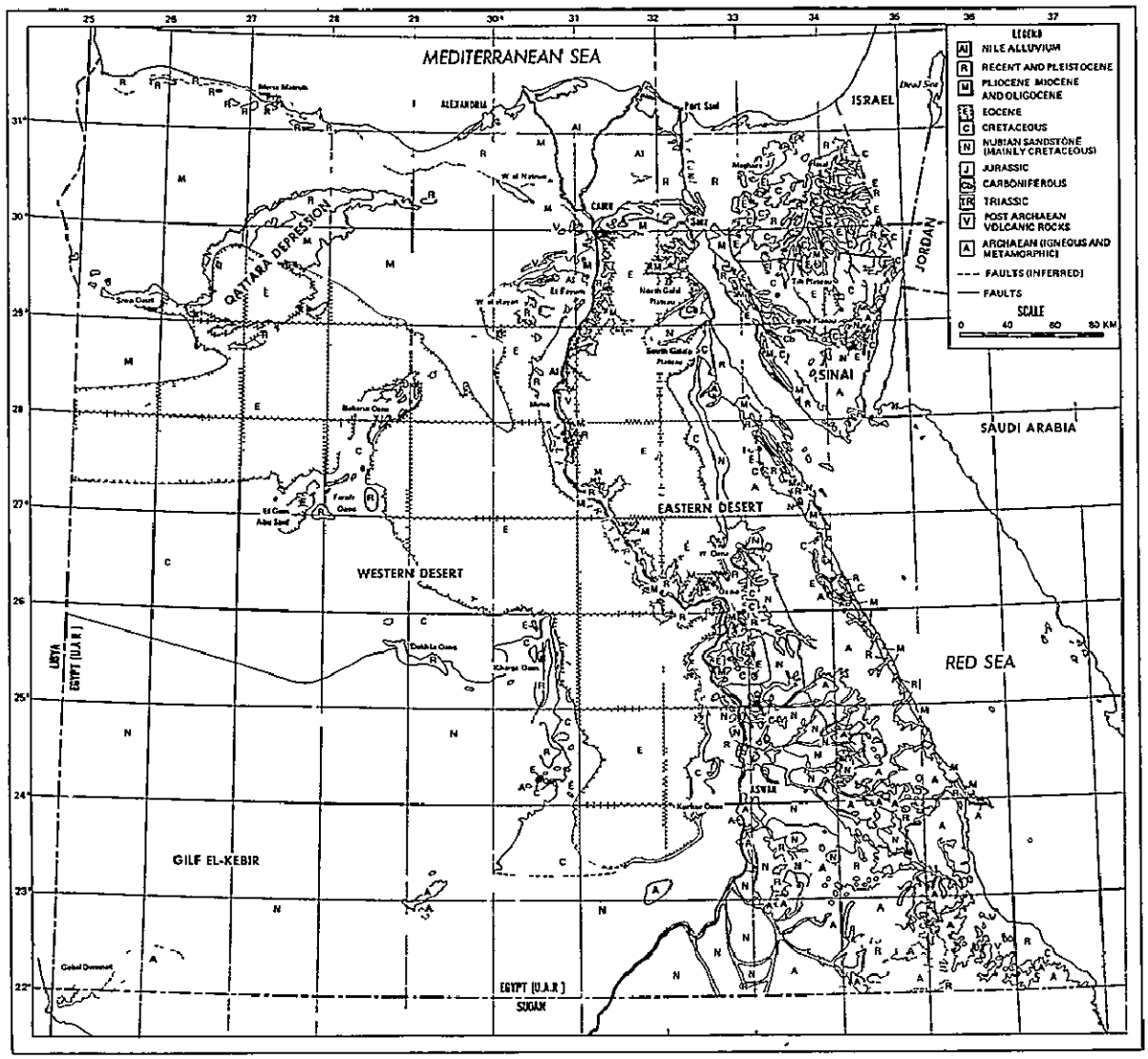

Figure 8. Geological map of Egypt (Said, 1966) (Dotted area indicates large units of Eocene limestone)

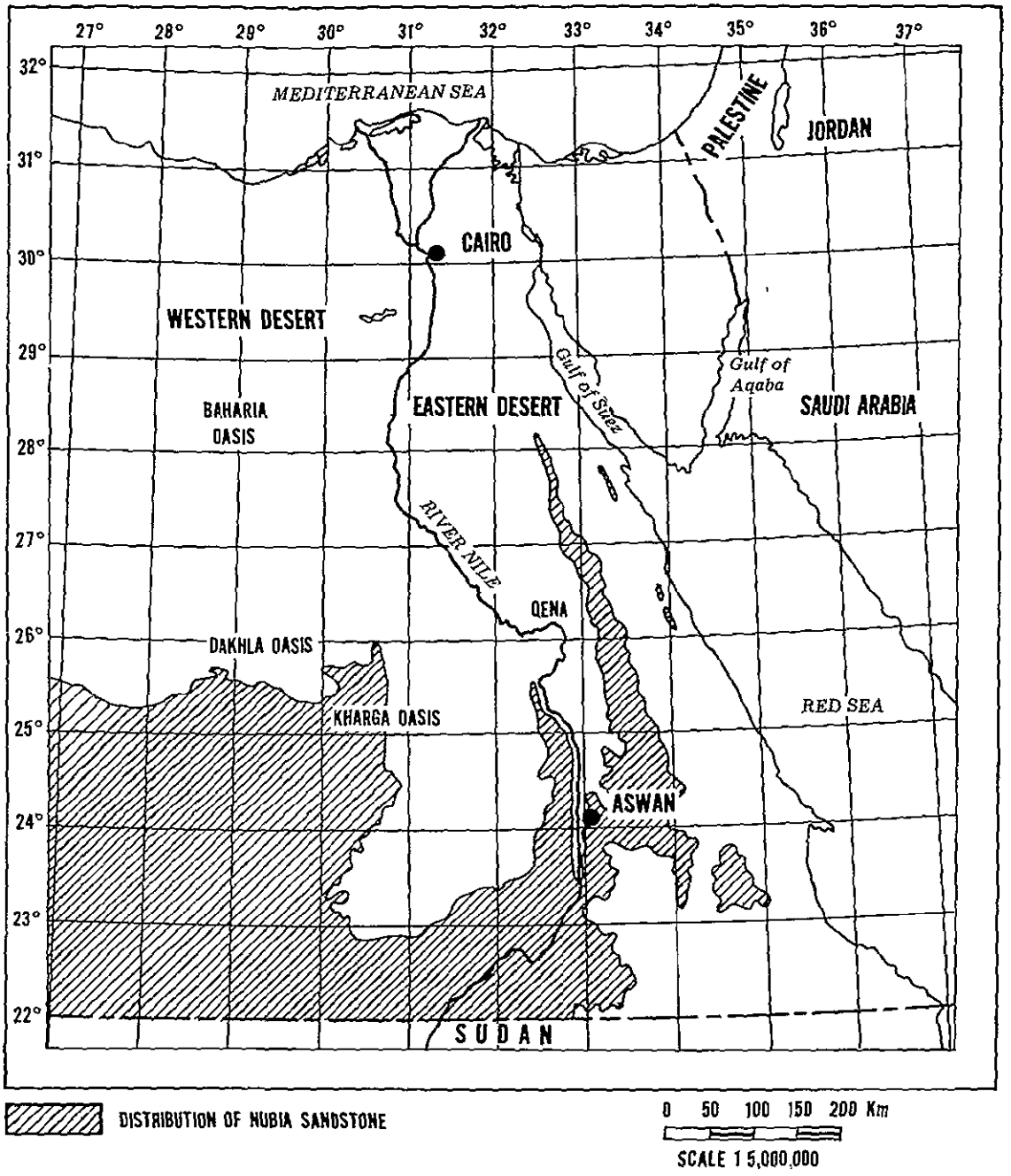

Figure 9. Map showing distribution of Nubia sandstone (diagonal lines) in Egypt (Issawi, 1973)

NIMBUS III DAY (HRIR)
26 MAY 1969
(PRE-FLOOD STAGE)
(a)

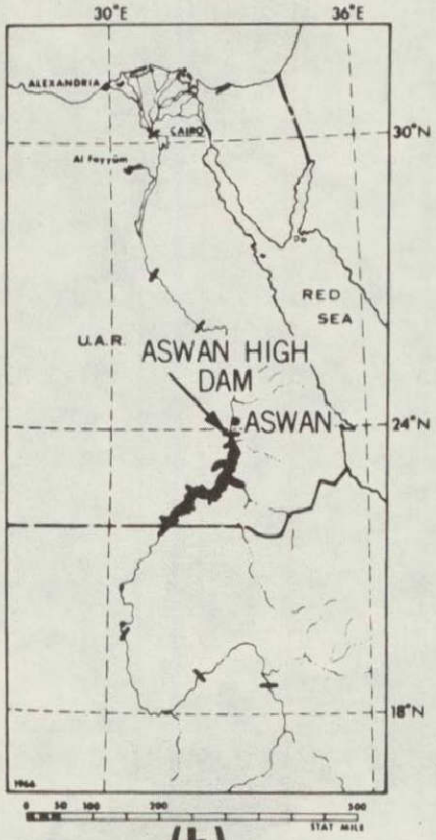

(b)

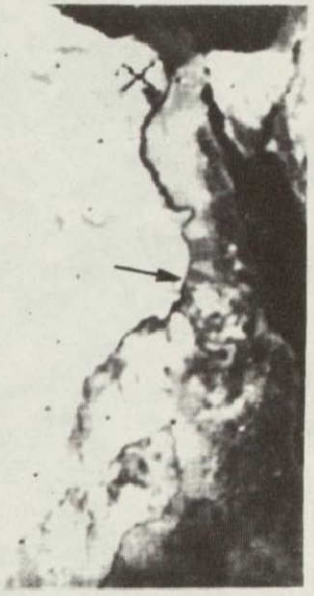

NIMBUS III DAY (HRIR)
11 SEPT 1969
(FLOOD STAGE)
(c)

FLOODING OF THE LAKE NASSER RESERVOIR
AT THE ASWAN HIGH DAM, UAR

Figure 10. a. Nimbus 3 HRIR (day), 26 May 1969, pre-flood stage of Lake Nasser; b. Map of flood area of Lake Nasser; c. Nimbus 3 HRIR (day), 11 Sept. 1966, flood stage

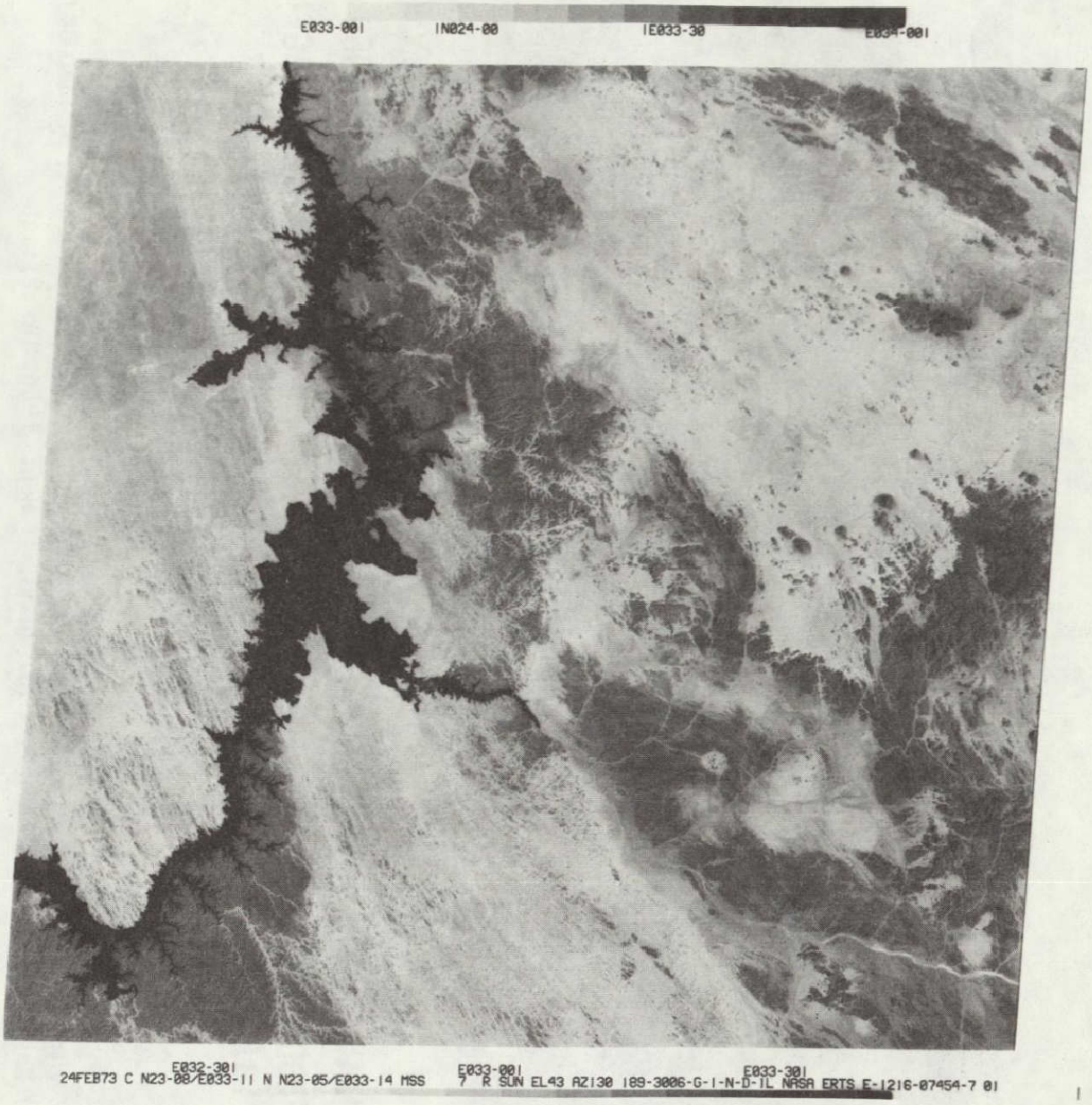

Figure 10.d. Landsat 1 MSS 7, 24 Feb. 1973 over Lake Nasser, Egypt, (UAR)

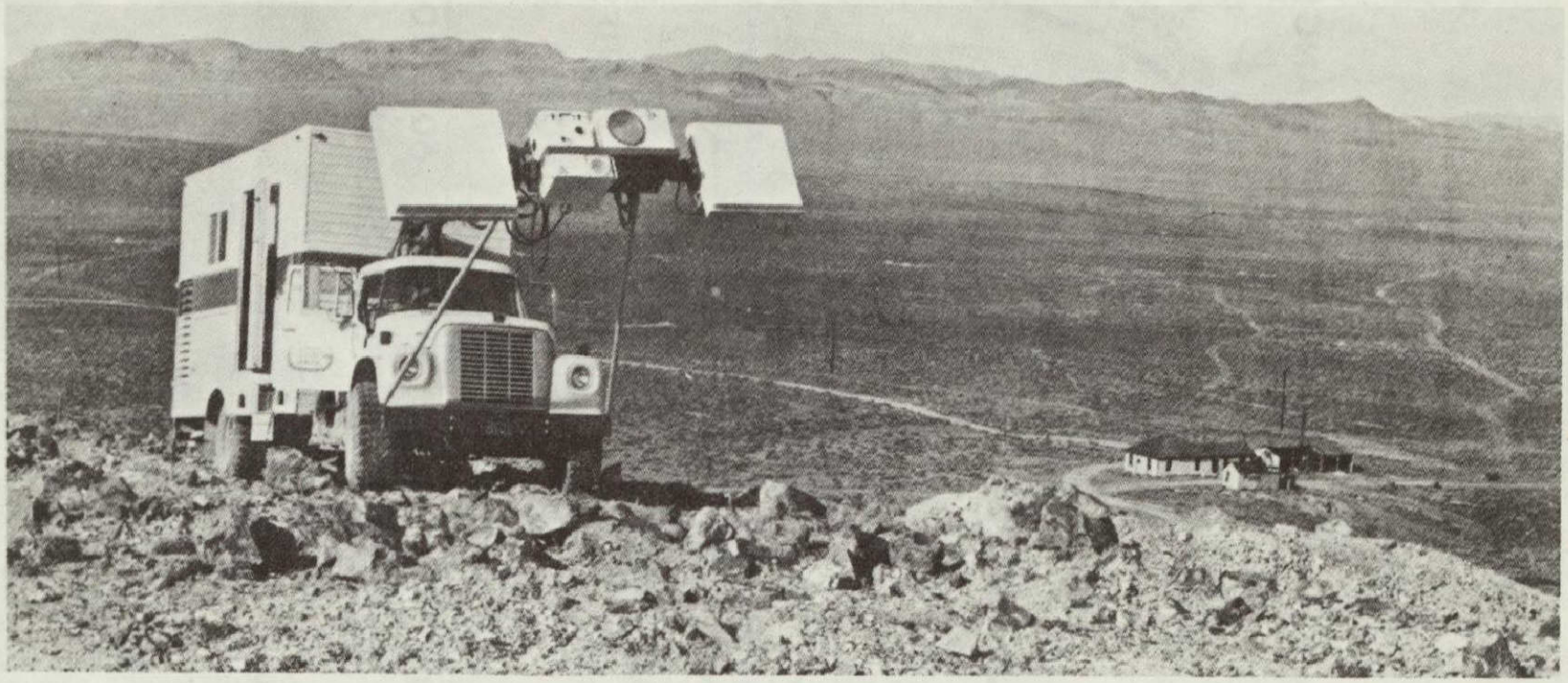

Figure 11. Truck-mounted passive microwave radiometer equipment used on geologic research (Edgerton and Trexler, 1970)

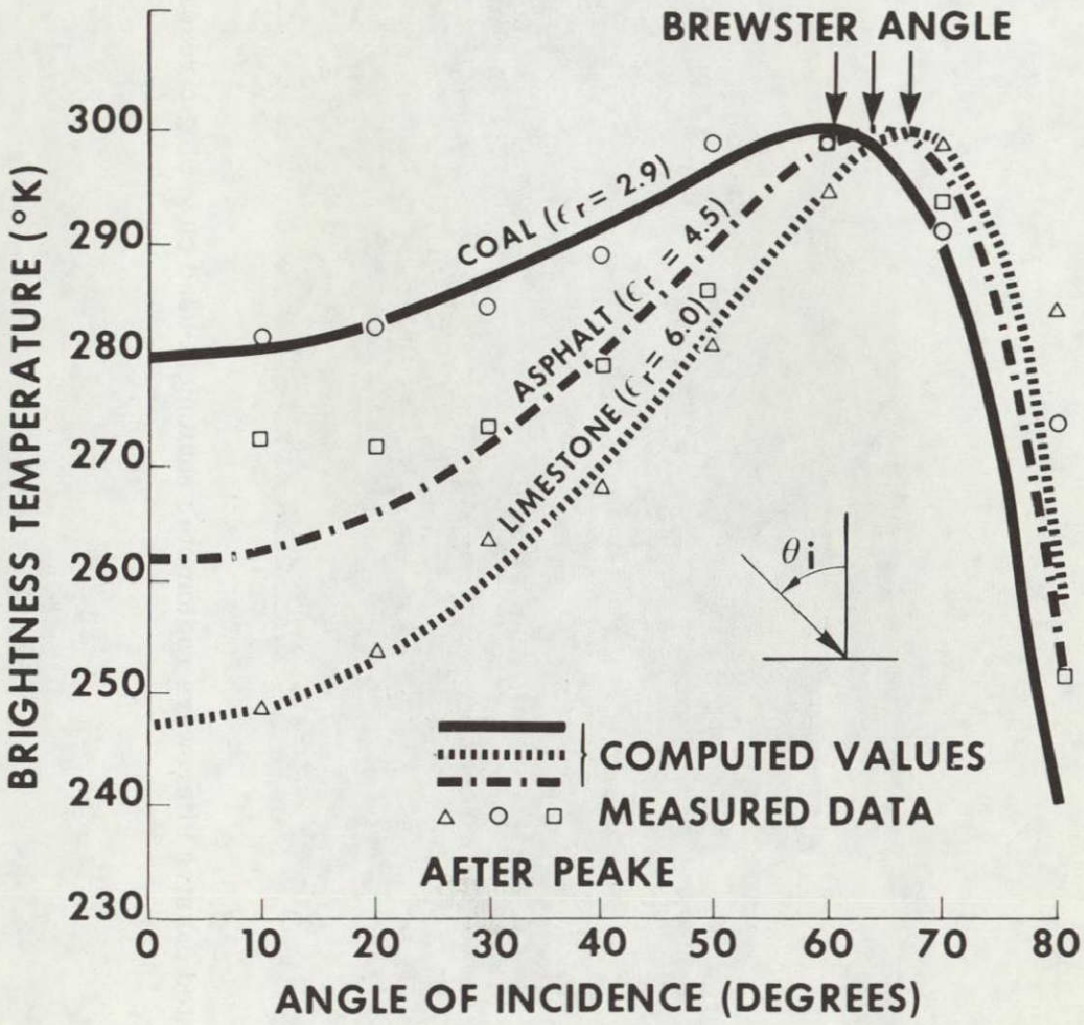

Figure 12. Computed and measured brightness temperatures of limestone, asphalt and coal at 10 GHz, vertical polarization (Edgerton and Trexler, 1970)

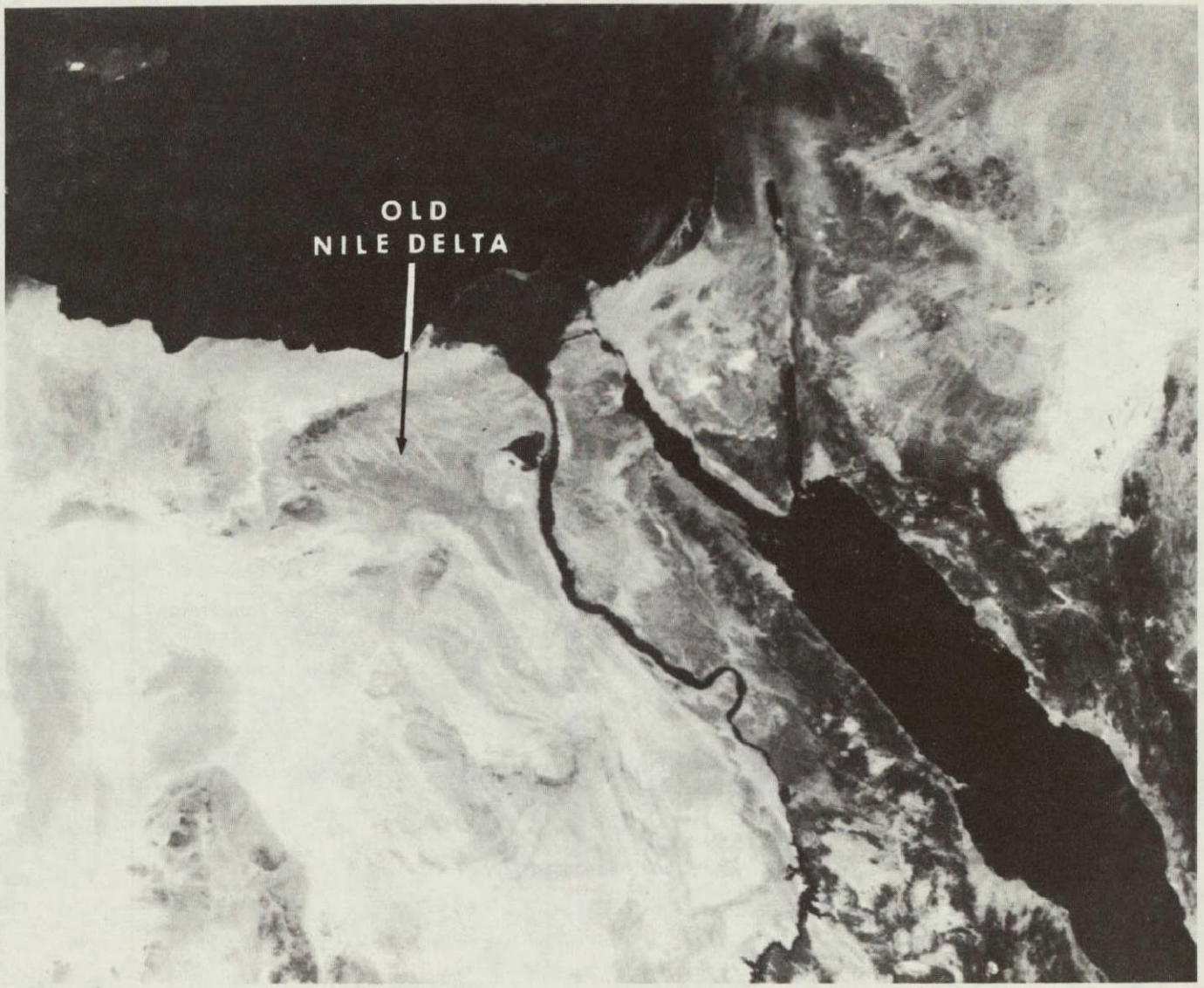

Figure 13. NOAA 2 Visual picture (VHRR), 23 October 1974 (1 km resolution) over Egypt and Red Sea area

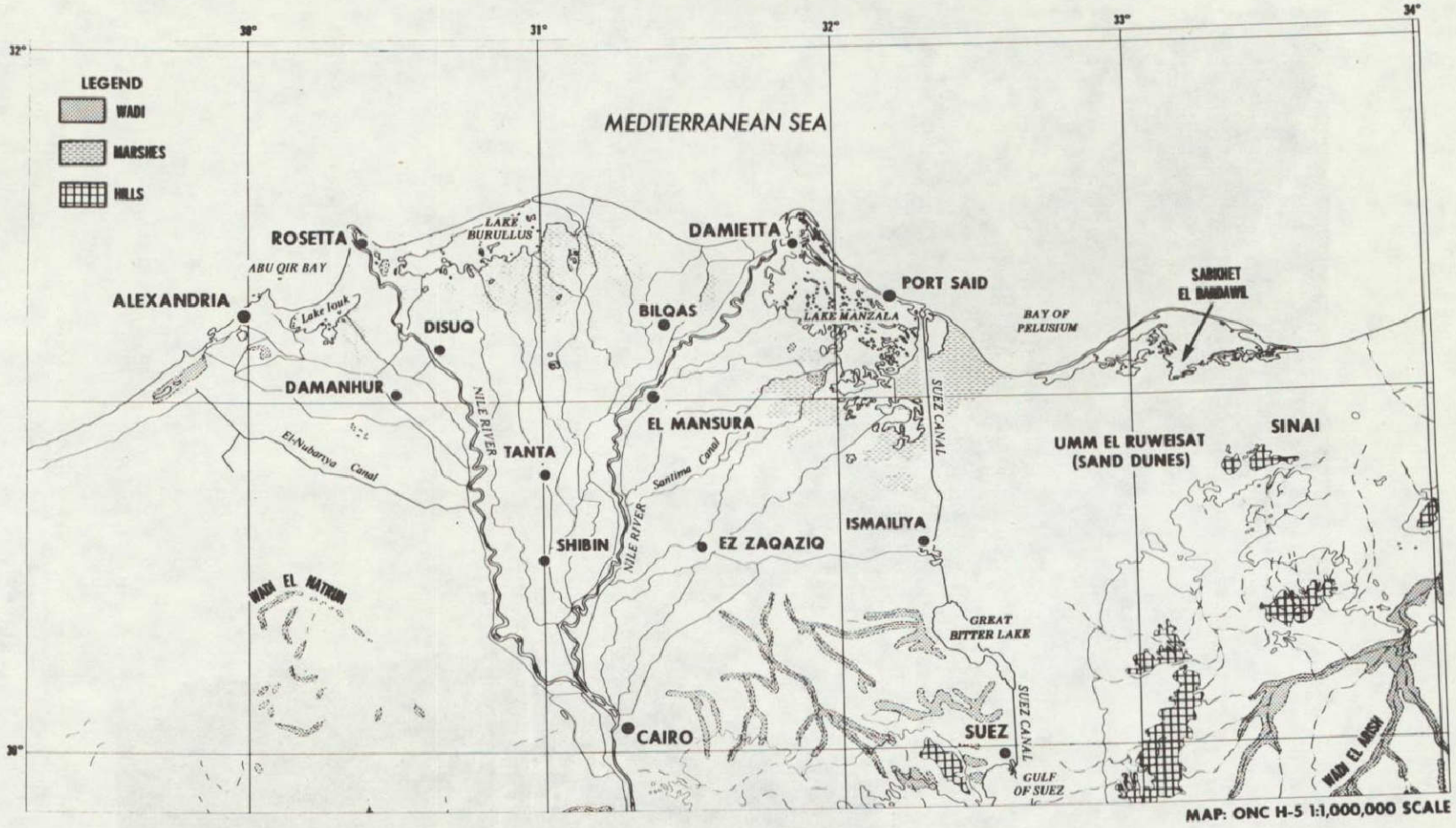

Figure 14. ONC H-5 MAP, 1:1 million scale of the Nile Delta

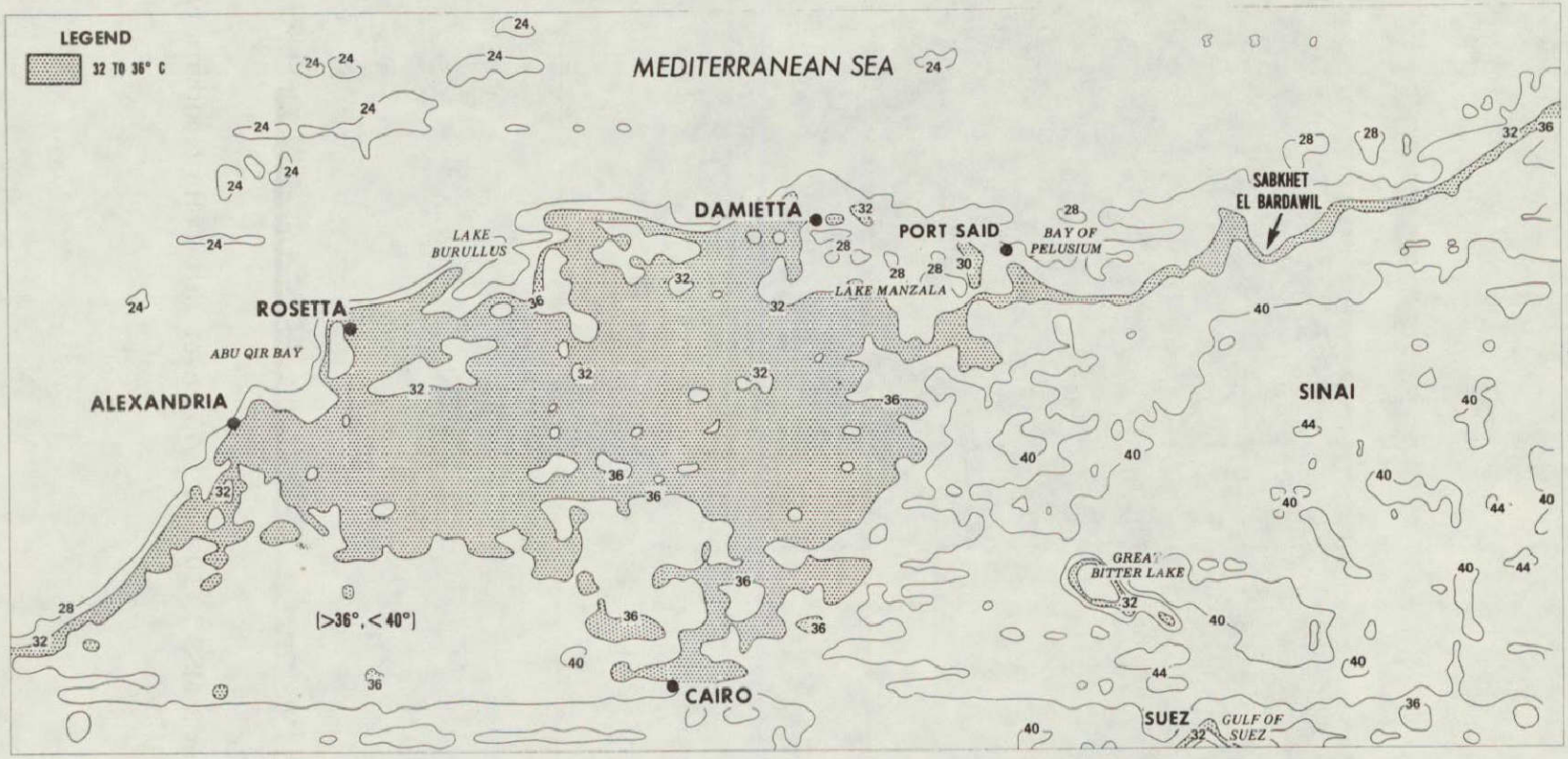

Figure 15. NOAA 4 Infra-red analysis (10.5 to 12.5 μm), orbit 2816, 28 June 1975 (Day - unrectified). Dotted area indicates T_B values from 32° to 36° C

Figure 16. Landsat 2 MSS 7, 10 May 1973, over Nile Delta (southern end), Egypt (UAR)

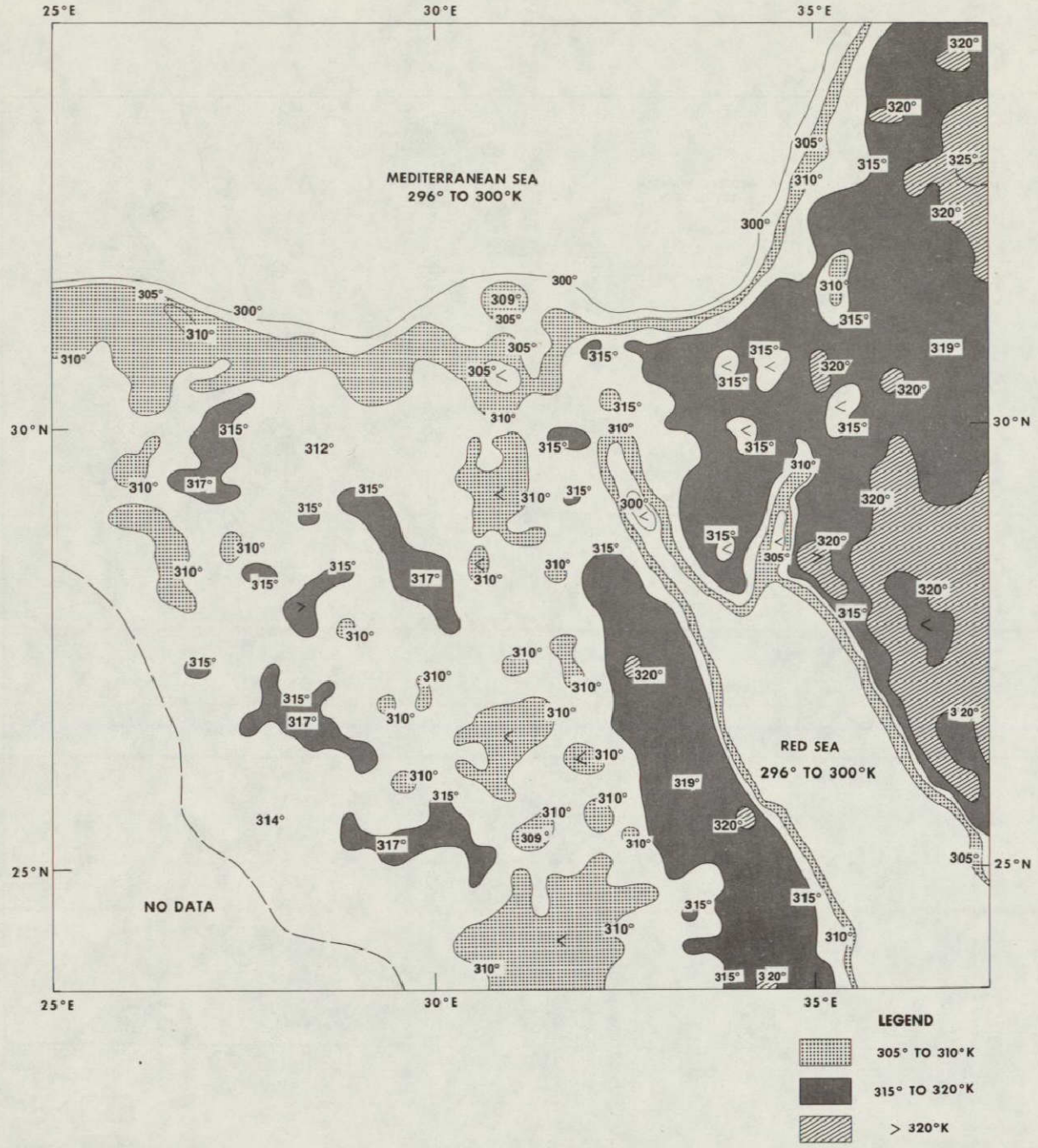

Figure 17. Nimbus 5 THIR 11 μm, orbit 7813 (day), 16 July 1974, analysis of computer-produced grid print map, 1:2 million, Mercator

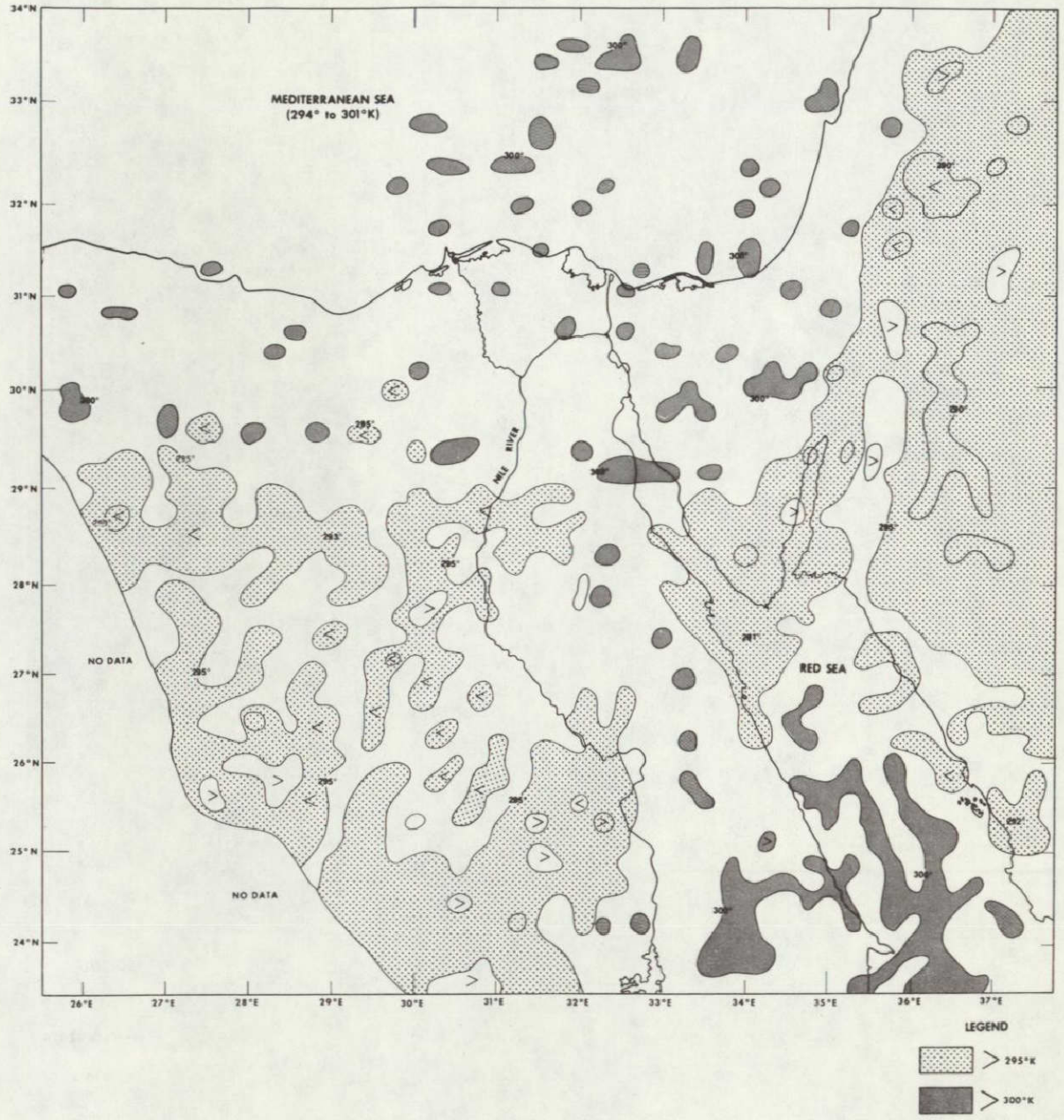

Figure 18. Nimbus 5 THIR 11 μm, orbit 7821 (night), 16 July 1974, analysis of computer-produced grid print map, 1:2 million, Mercator

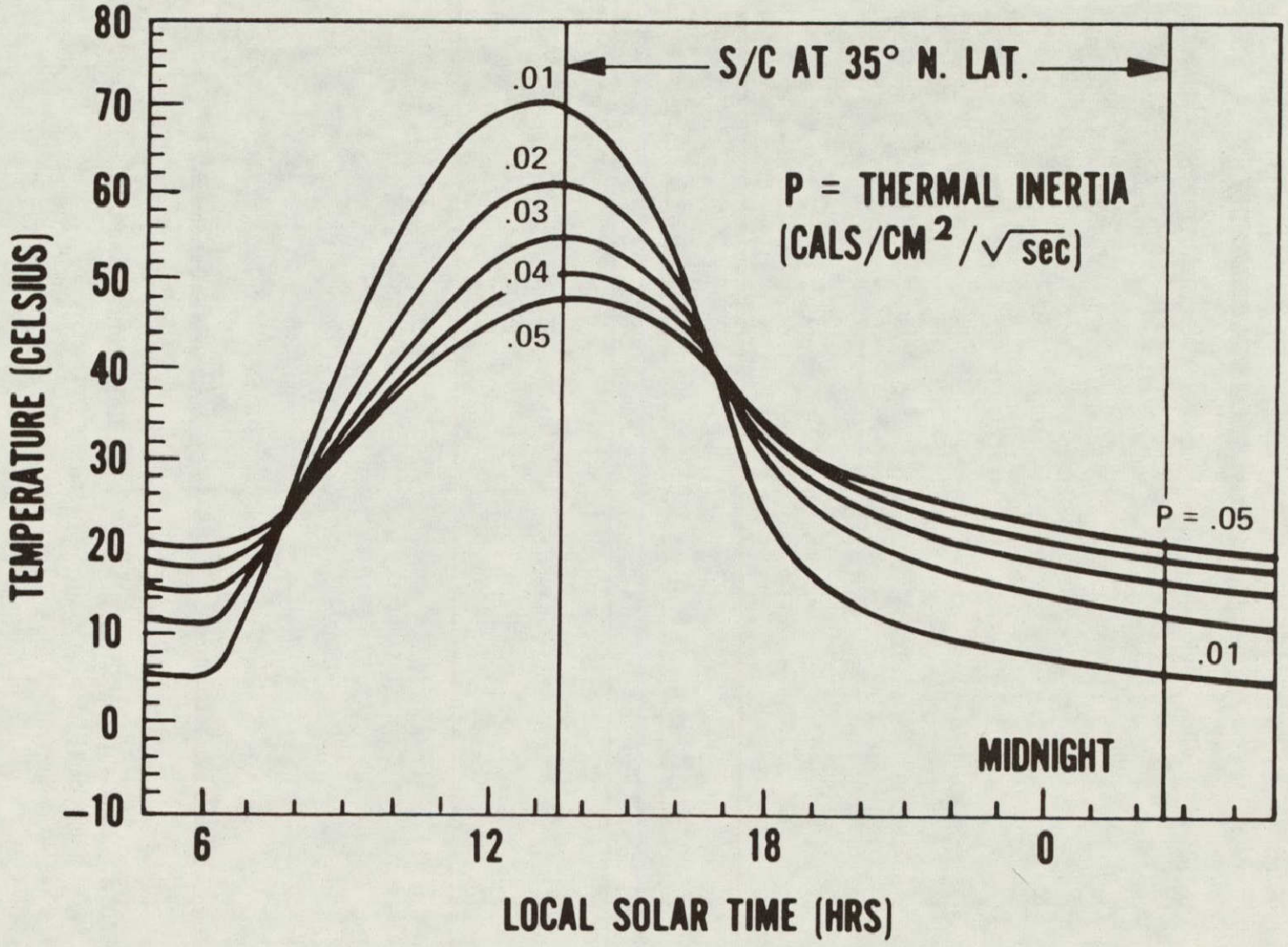

Figure 19. Diurnal surface temperature variation as a function of thermal inertia (Watson et al., 1971)

Figure 20.a. Landsat 1 MSS 7, 9 Nov. 1972, Lake Nasser and Nile Valley, Egypt (UAR)

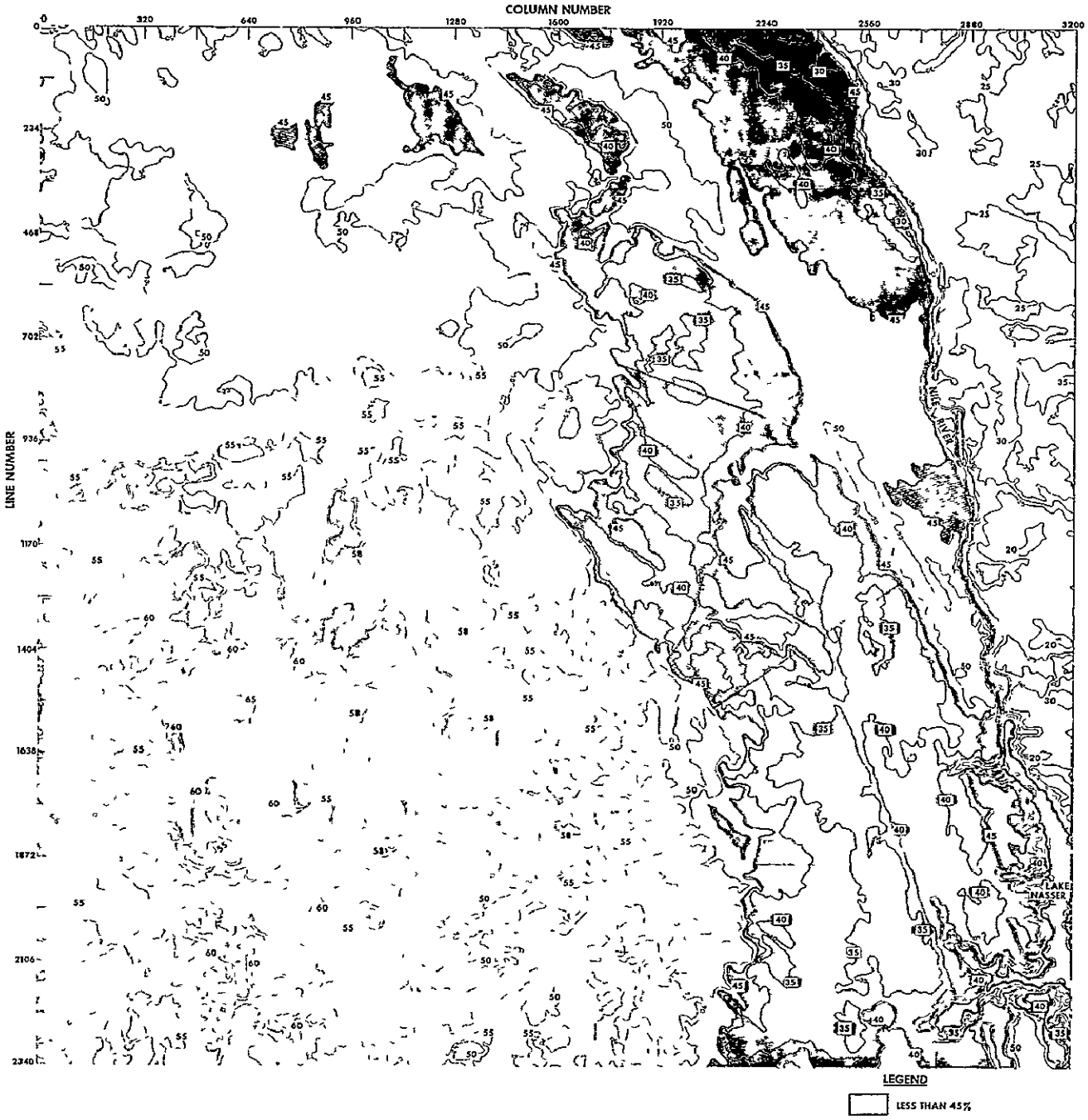

Figure 20.b. Space reflectivity (%) derived from Landsat 1 MSS 7, 9 Nov. 1972 frame shown in Figure 20a (Cal-Comp line-drawn)

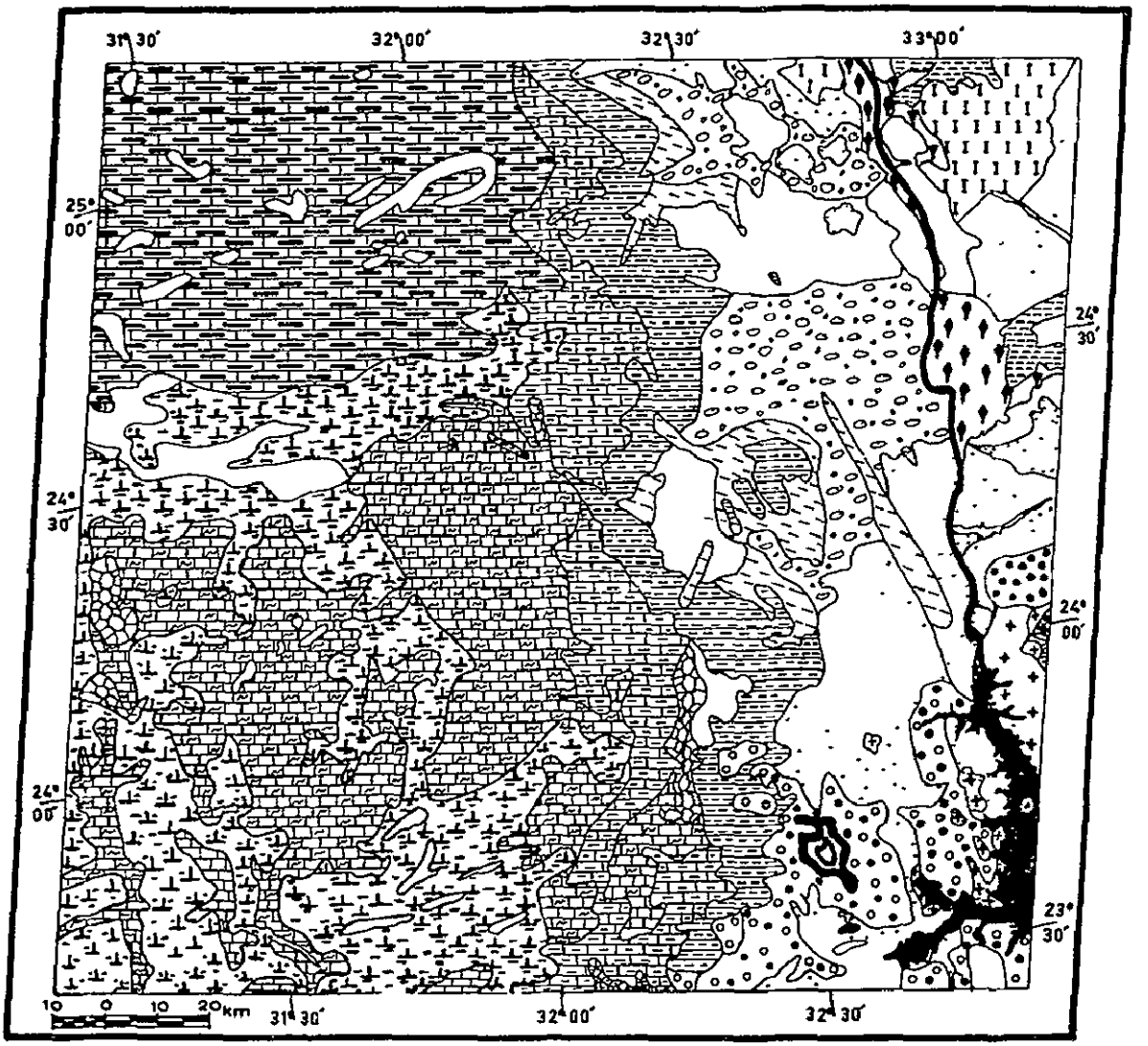

Figure 21. Geological map of West Aswan area, derived from Landsat 1 MSS 7, 9 Nov. 1972 frame shown in Figure 20a (El Shazely et al., 1974)

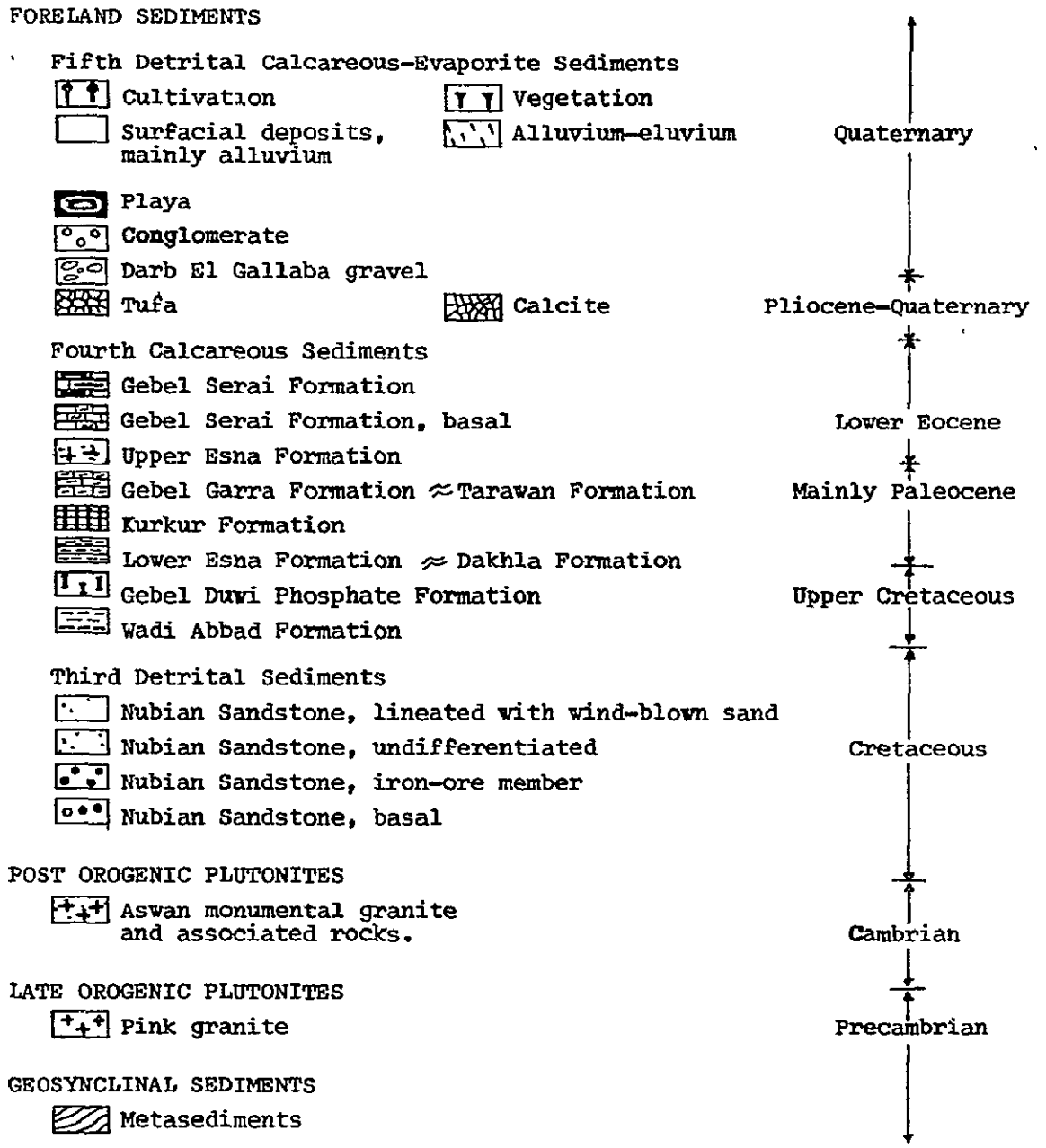

Figure 22. Geological unit classification used in Figure 21 (El Shazely et al., 1974)

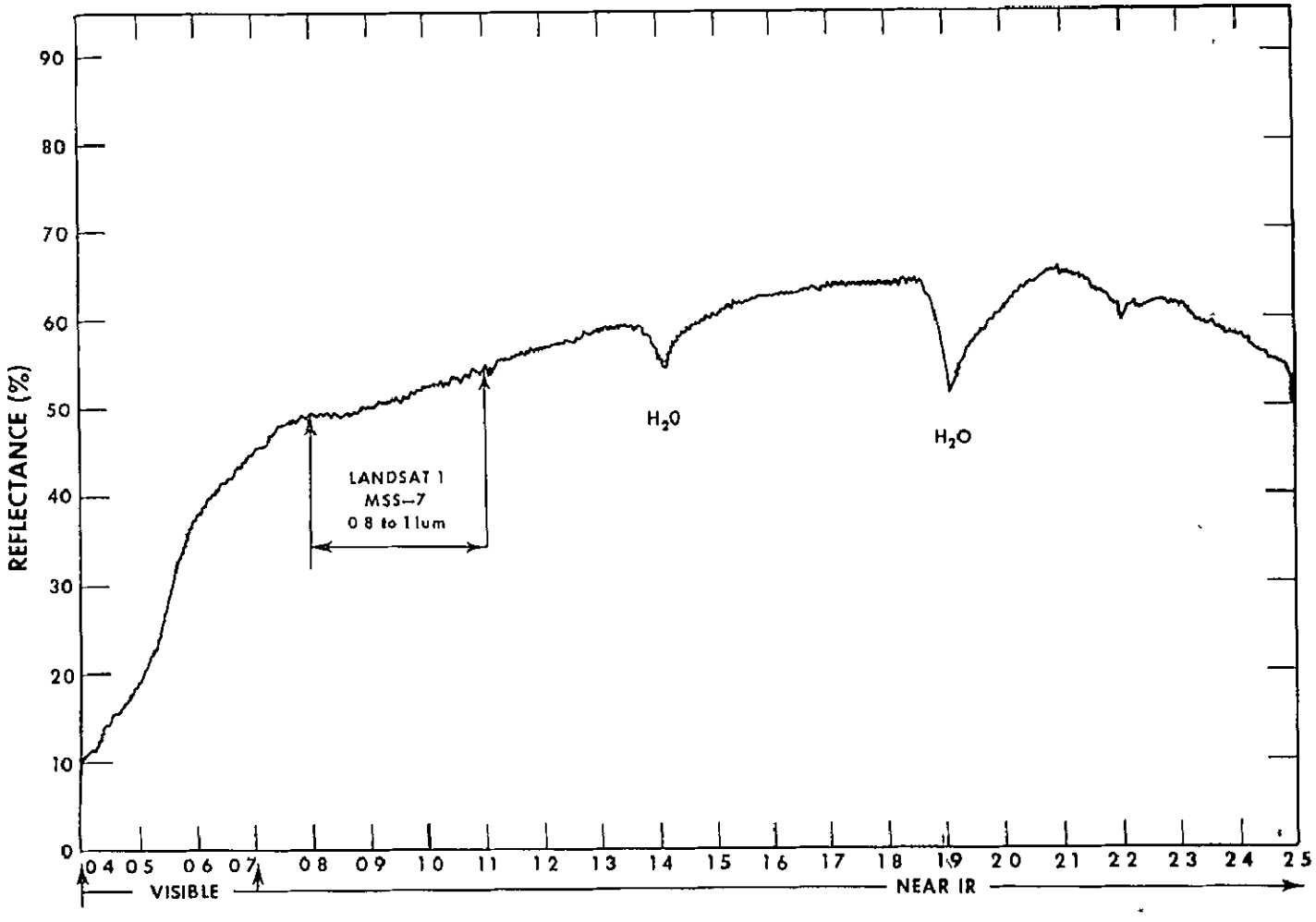

Figure 23. Laboratory spectographic analysis of Sinai desert sand showing total diffusive reflectance (%)

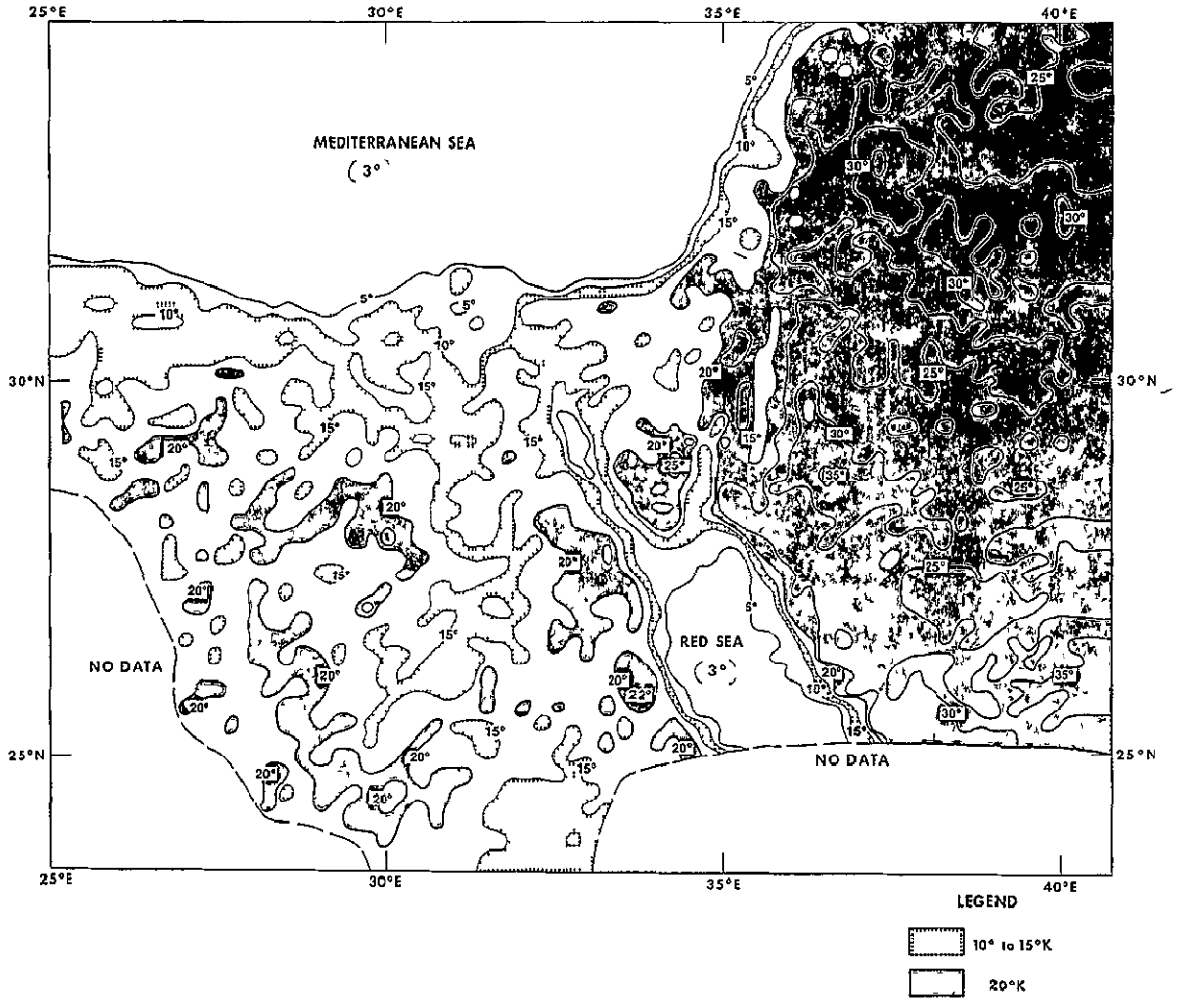

Figure 24. Nimbus 5 THIR 11 μm, orbit 7813 (day) – orbit 7821 (night) 16 July 1974; analyses of brightness temperature difference, computer-produced grid print map, 1:2 million, Mercator

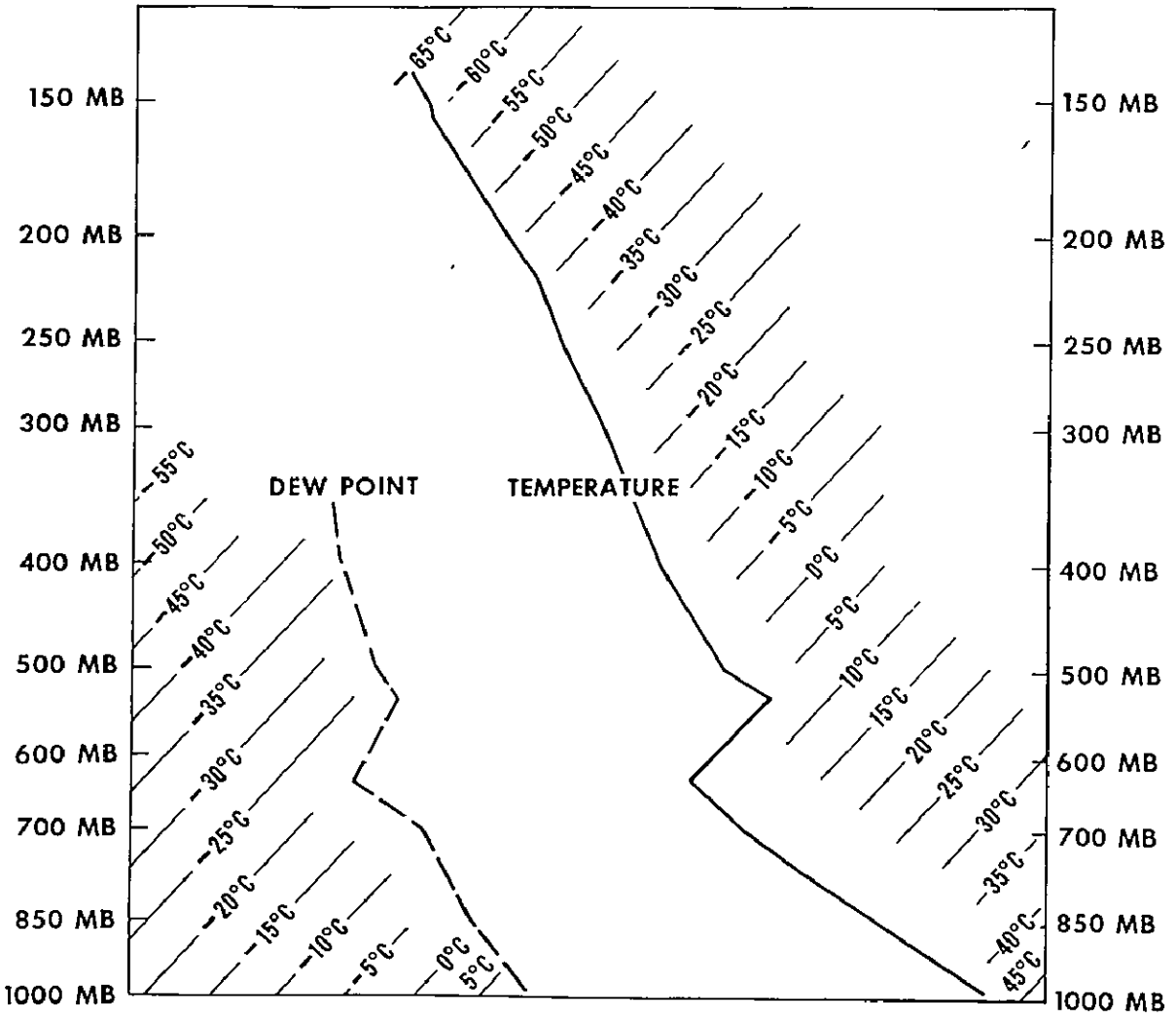

Figure 25. Radiosonde data, 1200 GMT, 16 July 1974, Aswan, Egypt (UAR)

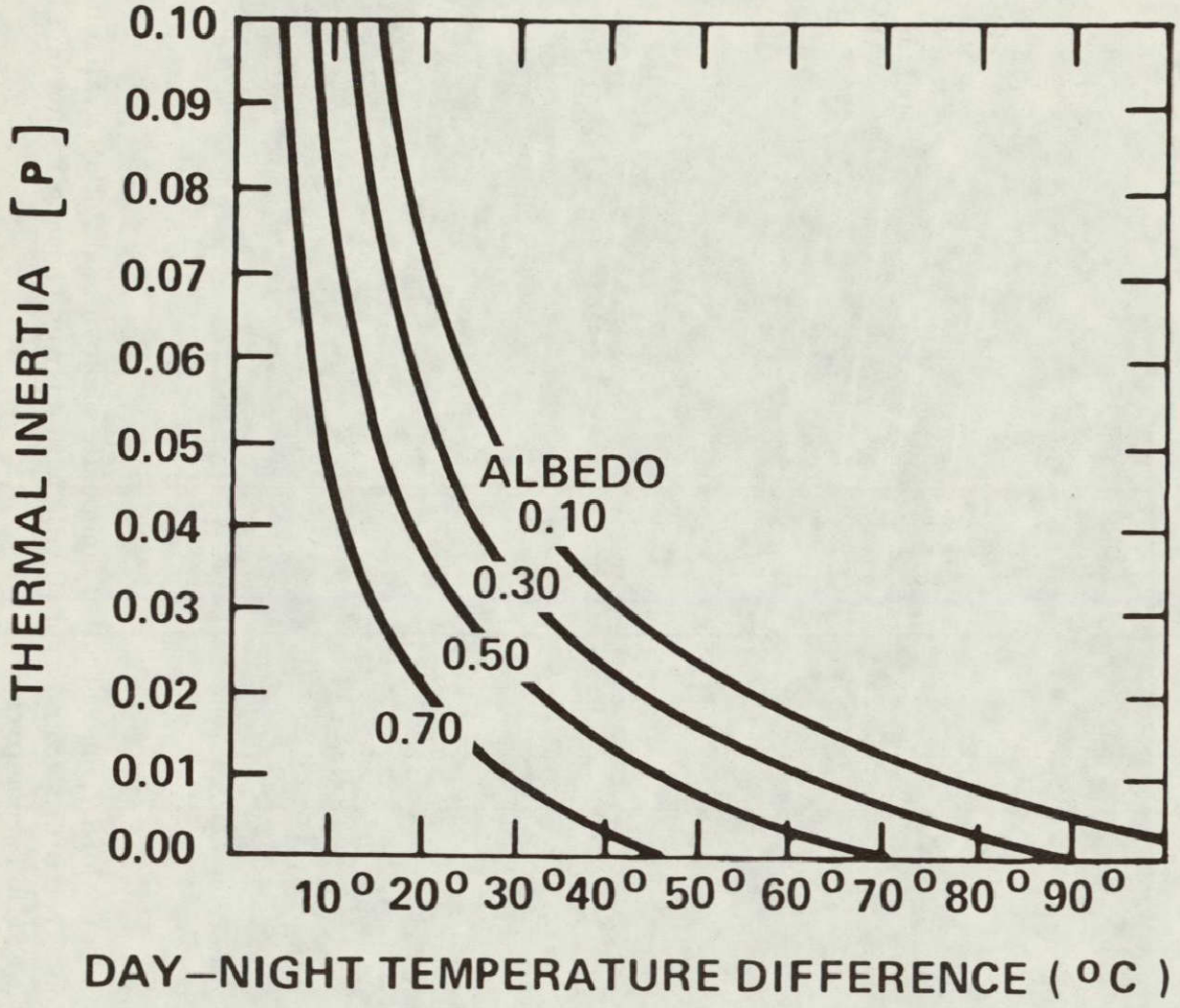

Figure 26. Least squares fit of thermal inertia versus day-night temperature difference for albedos ranging from 0.10 to 0.70 (Pohn et al., 1974)

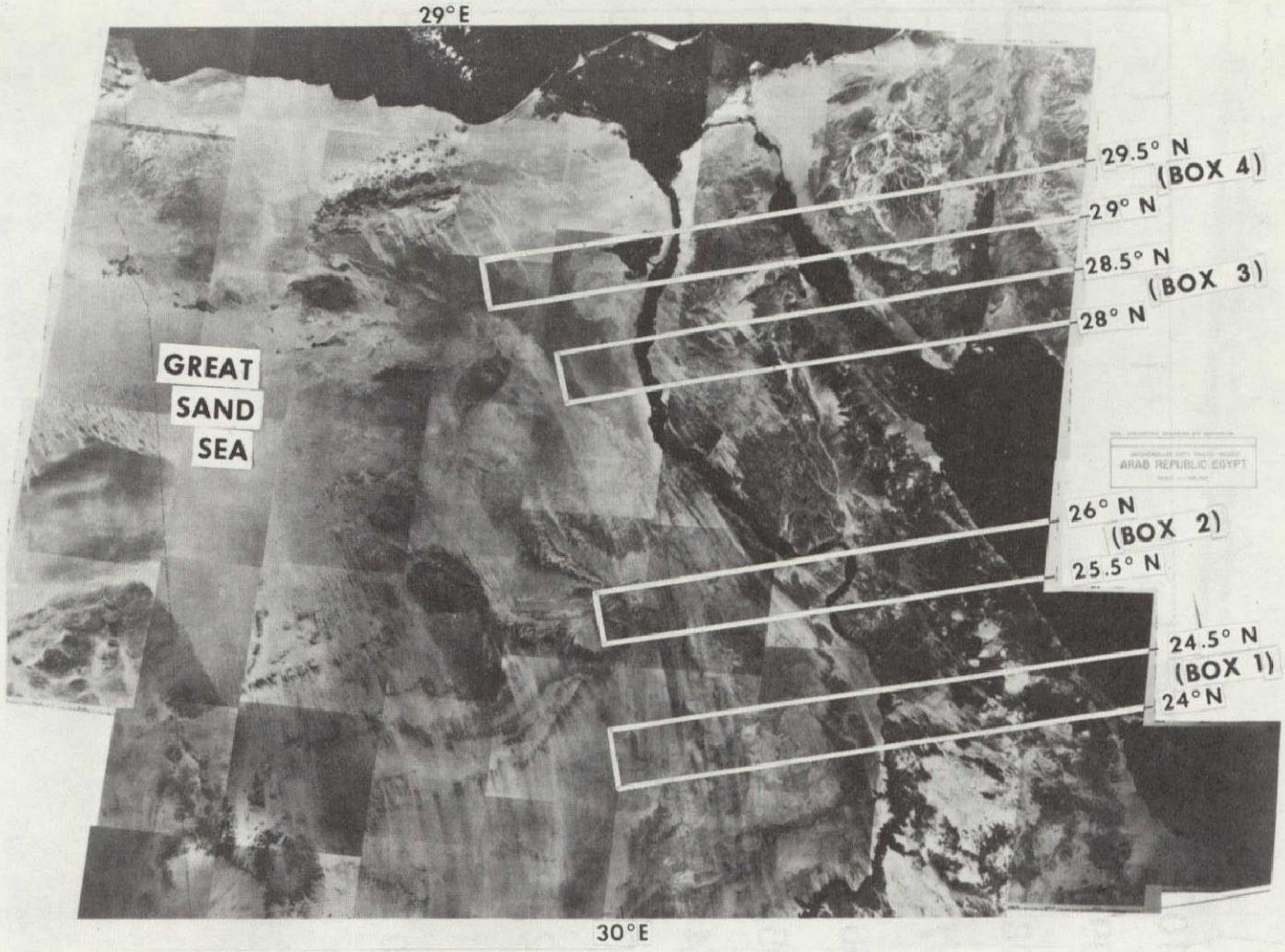

Figure 27. Landsat 1 MSS 7, uncontrolled composite photo-mosaic of all available cloud-free orbits over Egypt (UAR), with 4 boxes showing region of THIR and ESMR T_B comparison

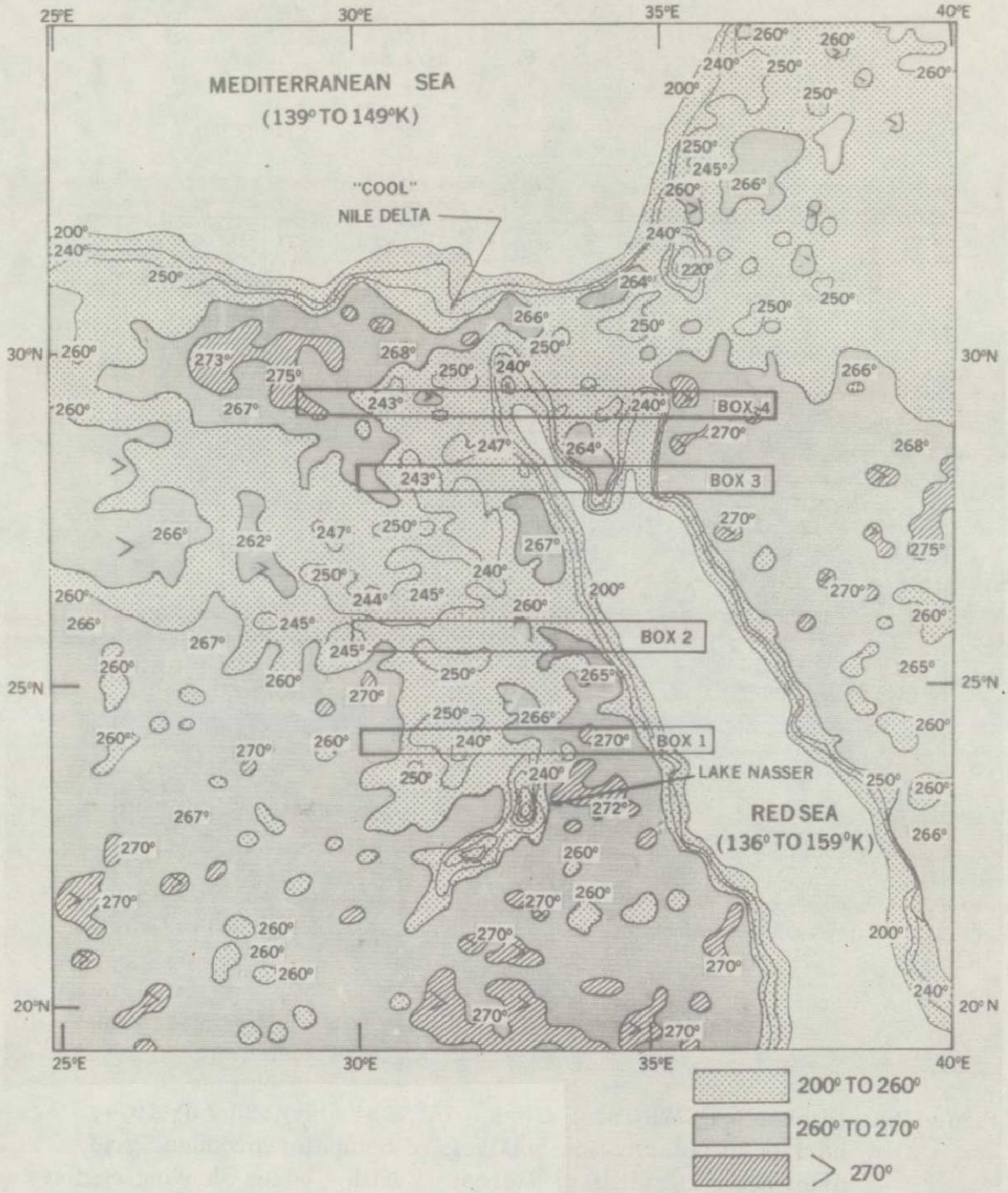

Figure 28. Nimbus 5 ESMR 19.35 GHz, orbit 7821 (night), 16 July 1974; horizontal polarization; analysis of computer-produced grid print map, 1:2 million, Mercator, with 4 boxes showing region of THIR and ESMR T_B comparison

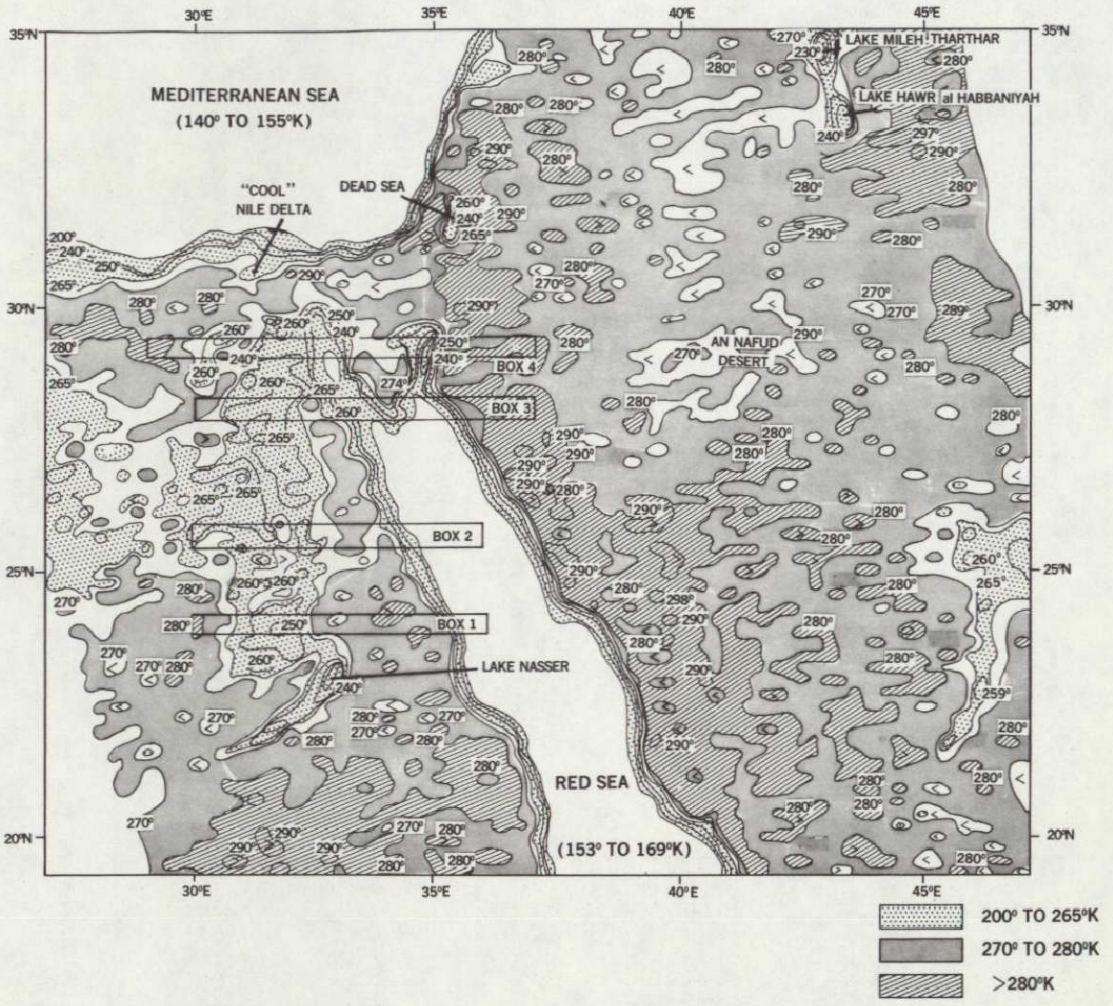

Figure 29. Nimbus 5 ESMR 19.35 GHz, orbit 7934 (day), 25 July 1974, horizontal polarization; analysis of computer-produced grid print map, 1:2 million, Mercator, with 4 boxes showing region of THIR and ESMR T_B comparison

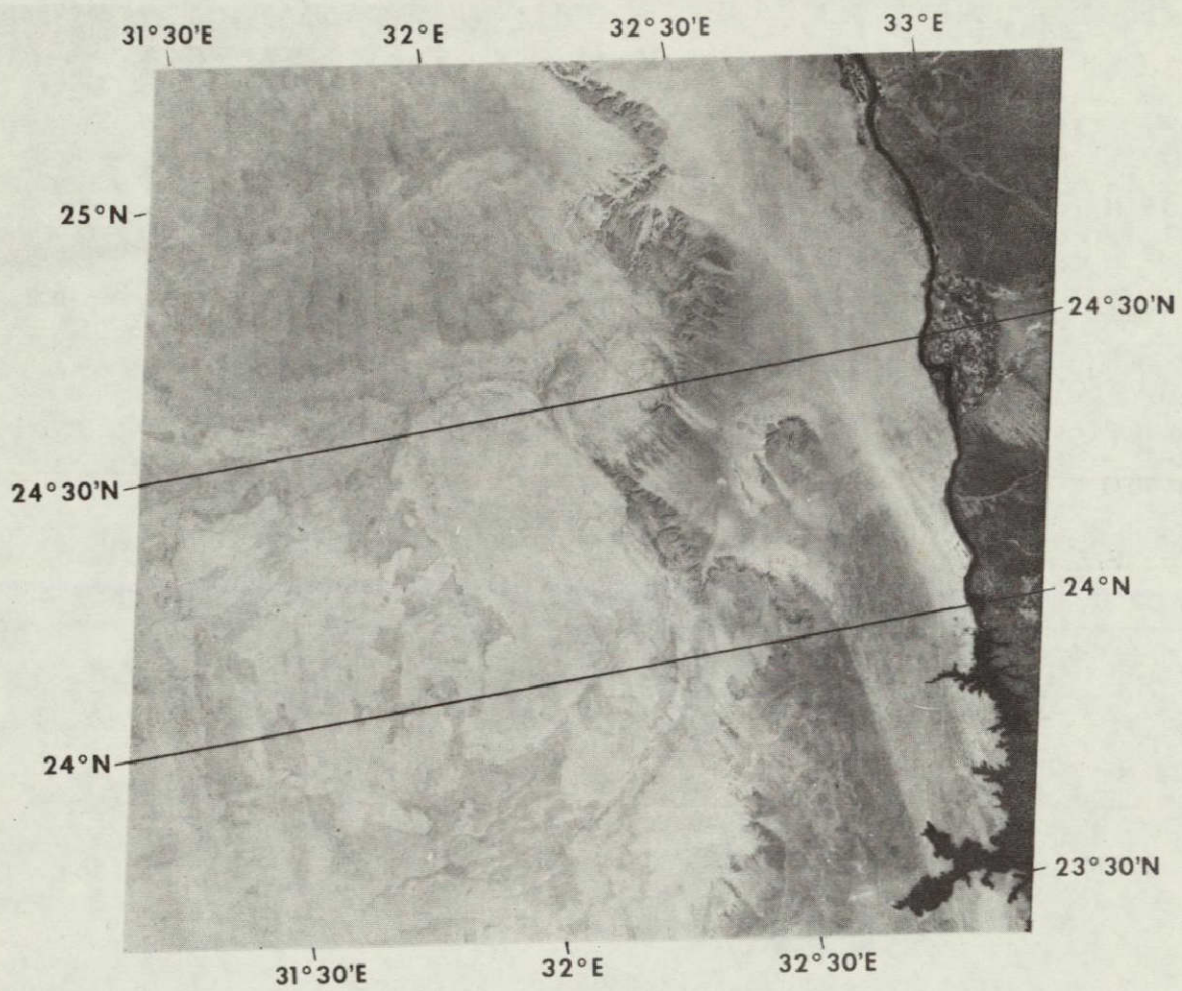

Figure 30. Landsat 1 MSS 7, 9 Nov. 1972, Lake Nasser and Nile Valley, Egypt (UAR), with box limits of THIR and ESMR T_B comparison

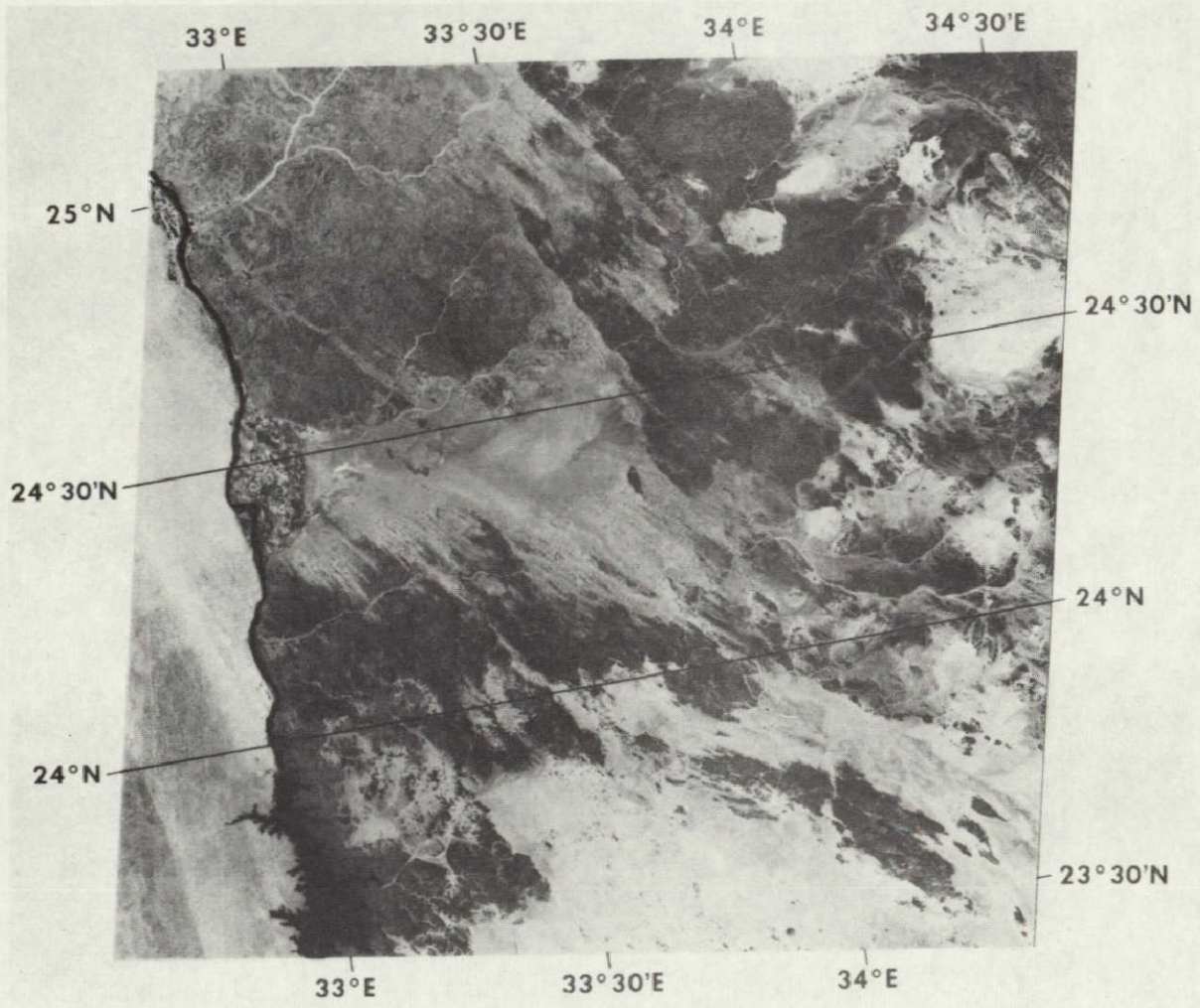

Figure 31. Landsat 1 MSS 7, 8 Nov. 1972, Lake Nasser and Nile Valley, Egypt (UAR), with box limits of THIR and ESMR T_B comparison

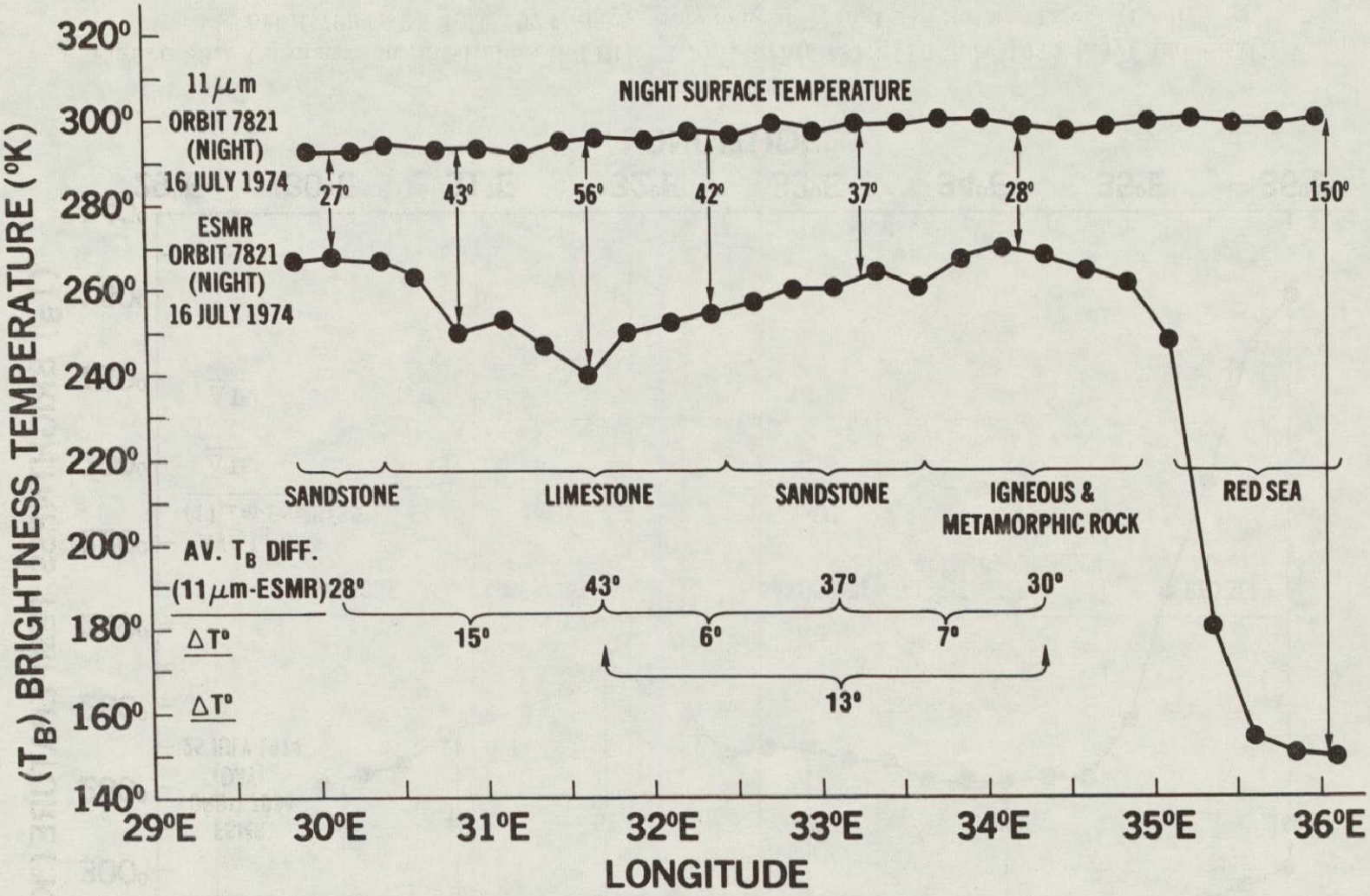

Figure 32. Comparison of Nimbus 5 THIR 11 μm and ESMR, orbit 7821 16 July 1974 (night) between 24° N and 24° 30° N, Egypt (UAR)

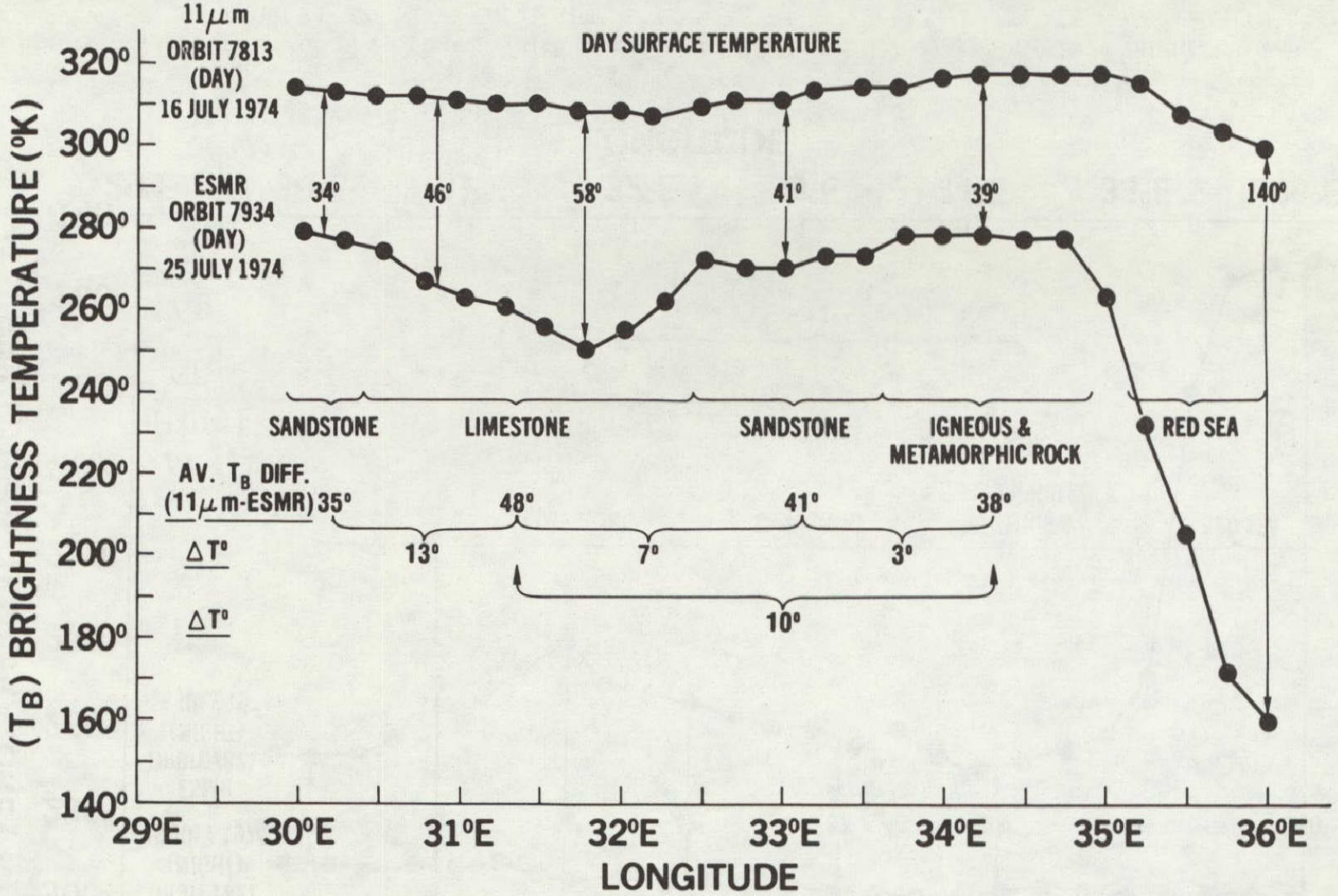

Figure 33. Comparison of Nimbus 5 THIR 11 μm, orbit 7813, 16 July 1974 (day) and ESMR, orbit 7934, 25 July 1974 (day), between 24°N and 24° 30'N. Egypt (UAR)

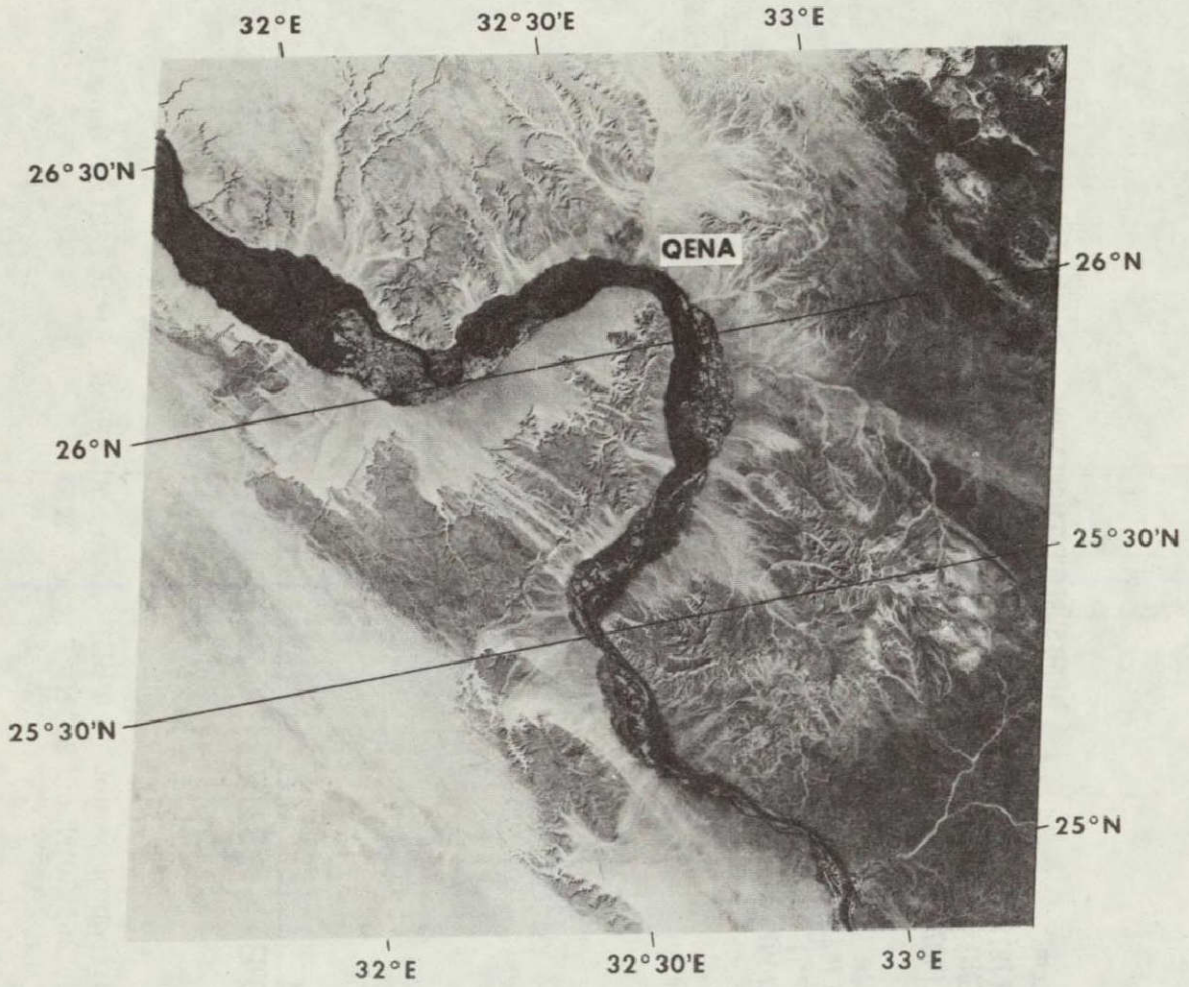

Figure 34. Landsat 1 MSS 7, 9 Nov. 1972, Nile River (Qena) Egypt (UAR) with box limits of THIR and ESMR T_B comparison

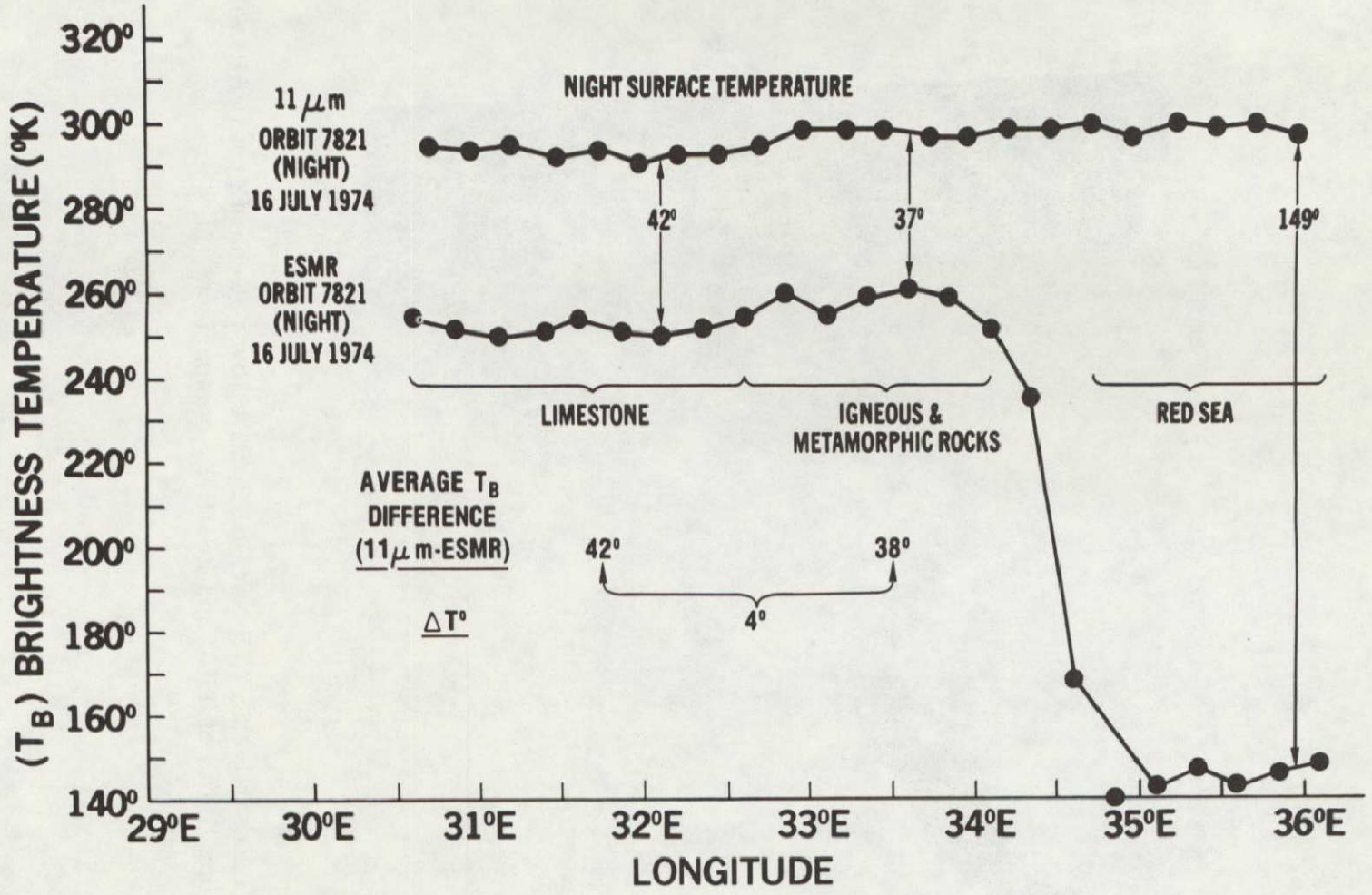

Figure 35. Comparison of Nimbus 5 THIR 11 μm and ESMR, orbit 7821 16 July 1974 (night) between 25° 30'N and 26° N, Egypt (UAR)

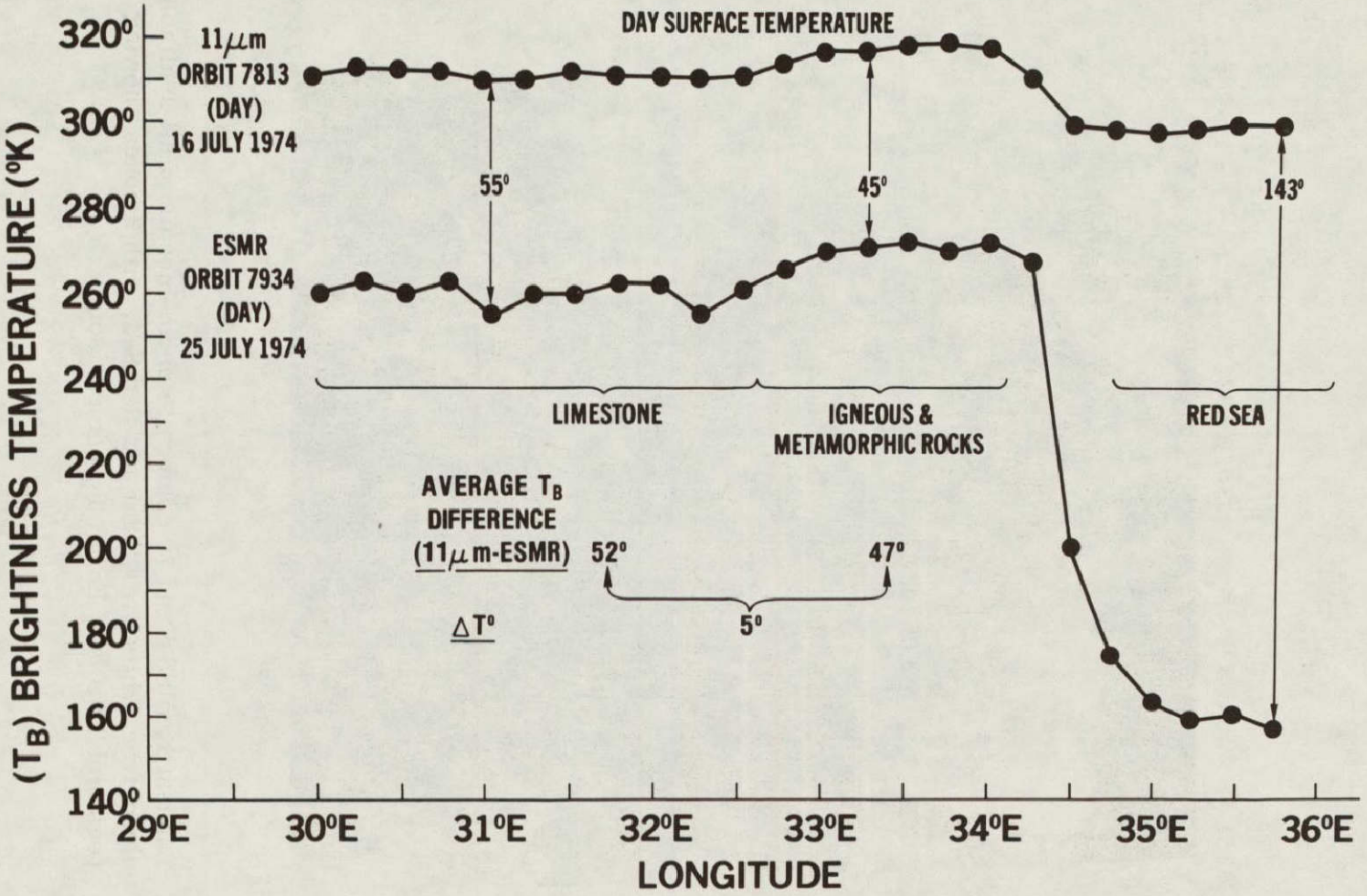

Figure 36. Comparison of Nimbus 5 THIR 11 μm, orbit 7813, 16 July 1974 (day) and ESMR, orbit 7934, 25 July 1974 (day) between 25° 30'N and 26°N, Egypt (UAR)

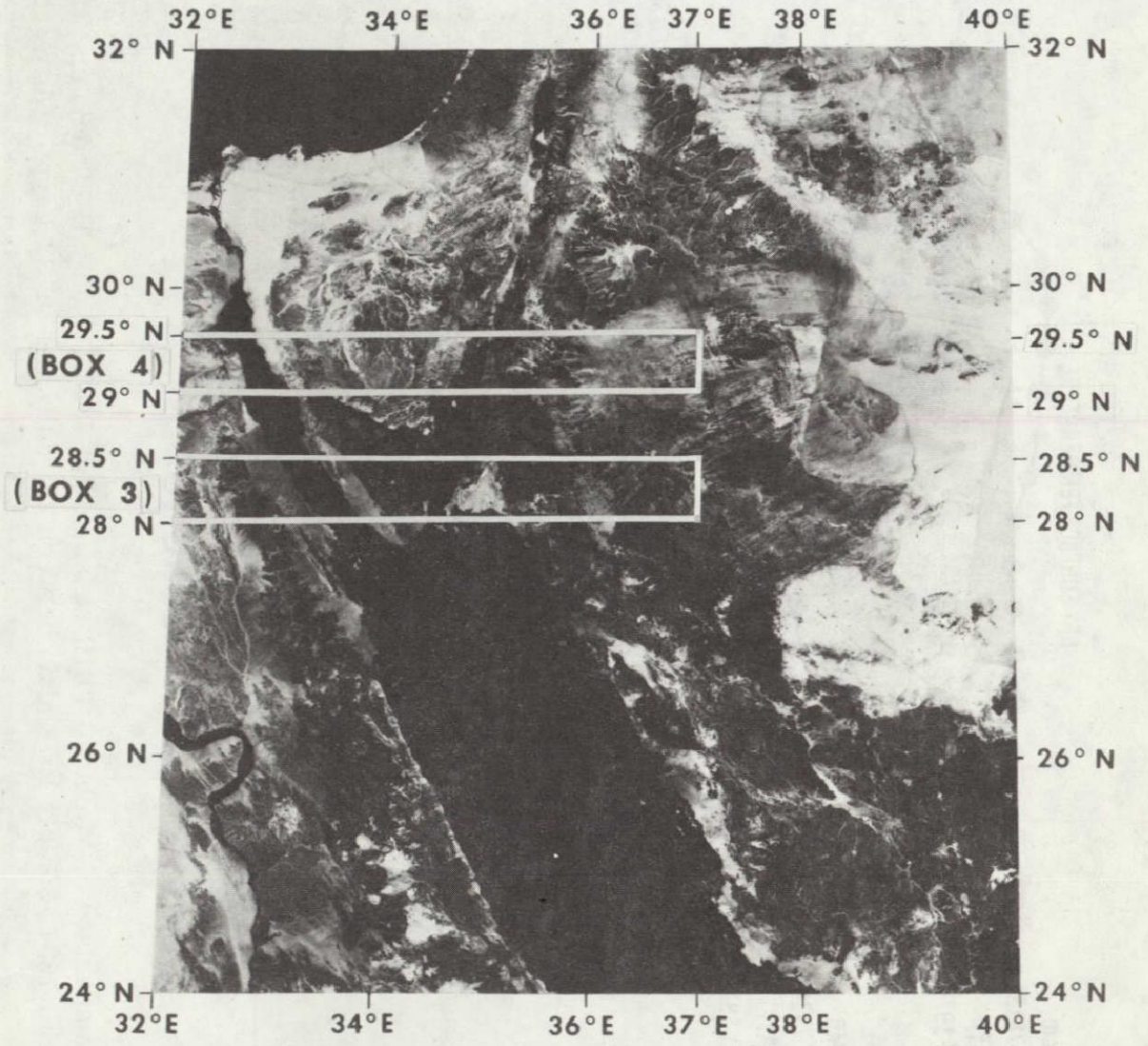

Figure 37. Landsat 1, MSS 5 and 7, composite photo-mosaic of all available cloud-free orbits over Sinai and Red Sea, with 2 boxes showing region of THIR and ESMR T_B comparison

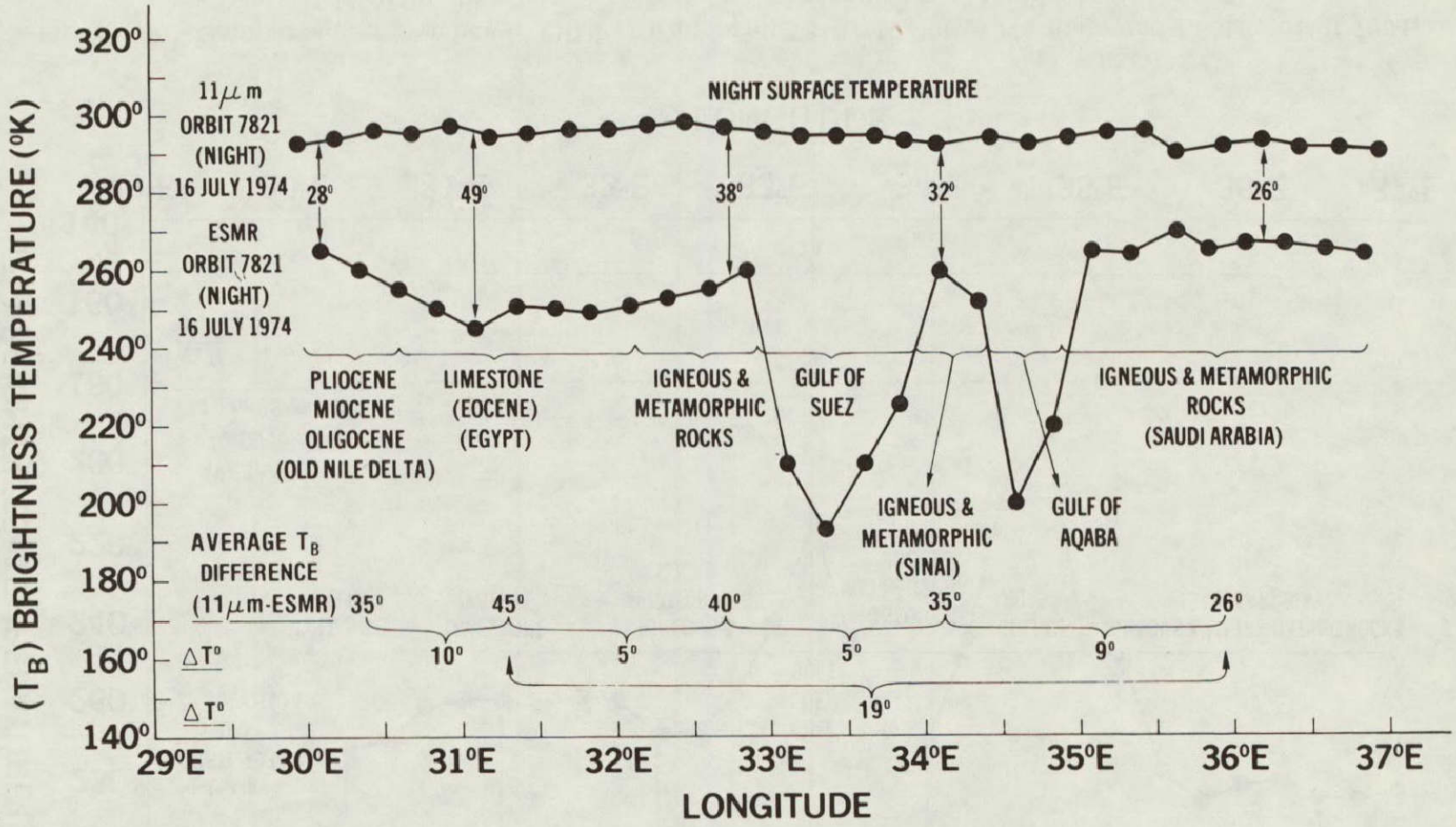

Figure 38. Comparison of Nimbus 5 THIR 11 μm and ESMR, orbit 7821, 16 July 1974 (night) between 28°N and 28° 30'N, Egypt and Saudi Arabia

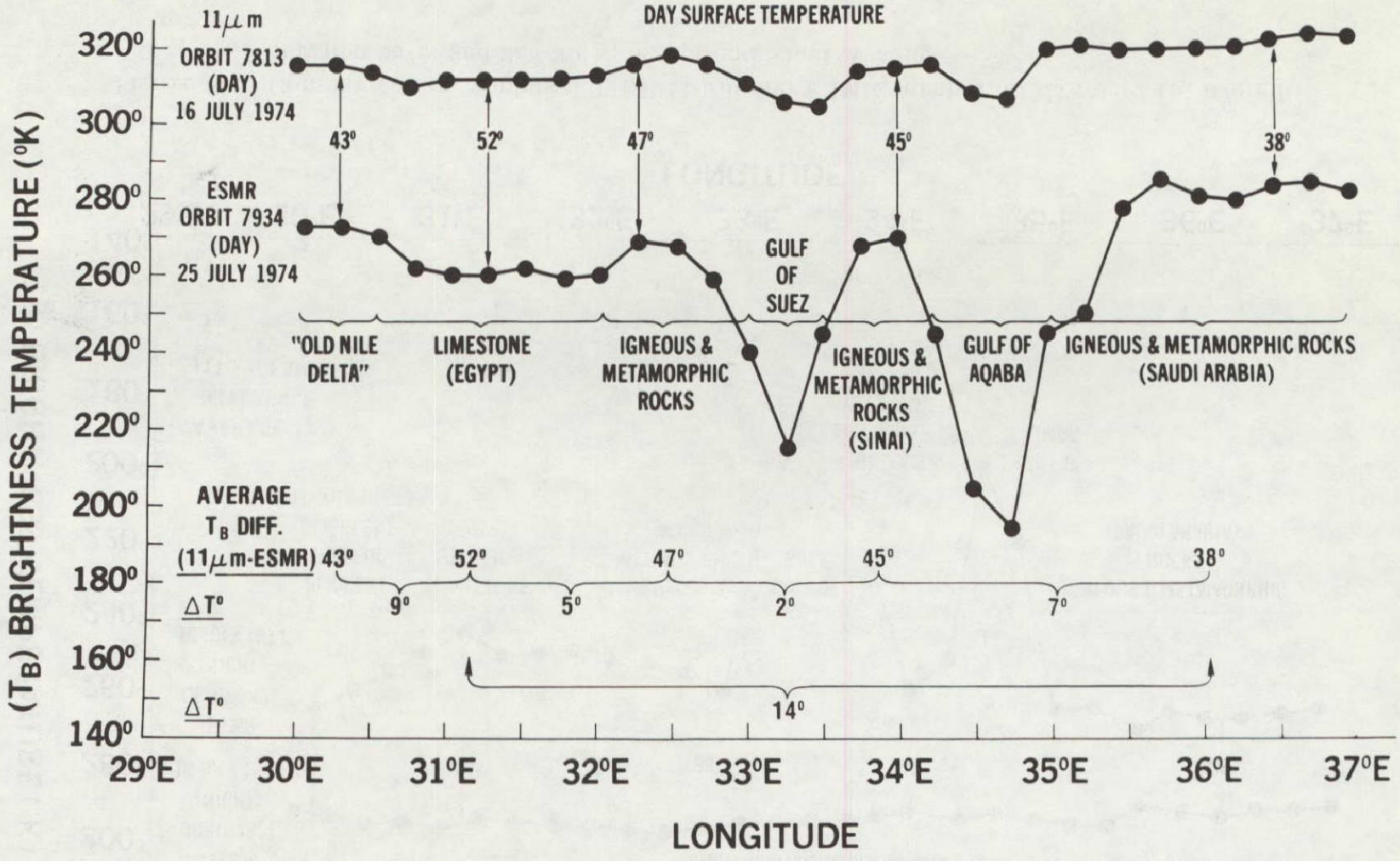

Figure 39. Comparison of Nimbus 5 THIR 11 μm, orbit 7813, 16 July 1974 (day) and ESMR, orbit 7934, 25 July 1974 (day), between 28°N and 28° 30'N, Egypt and Saudi Arabia

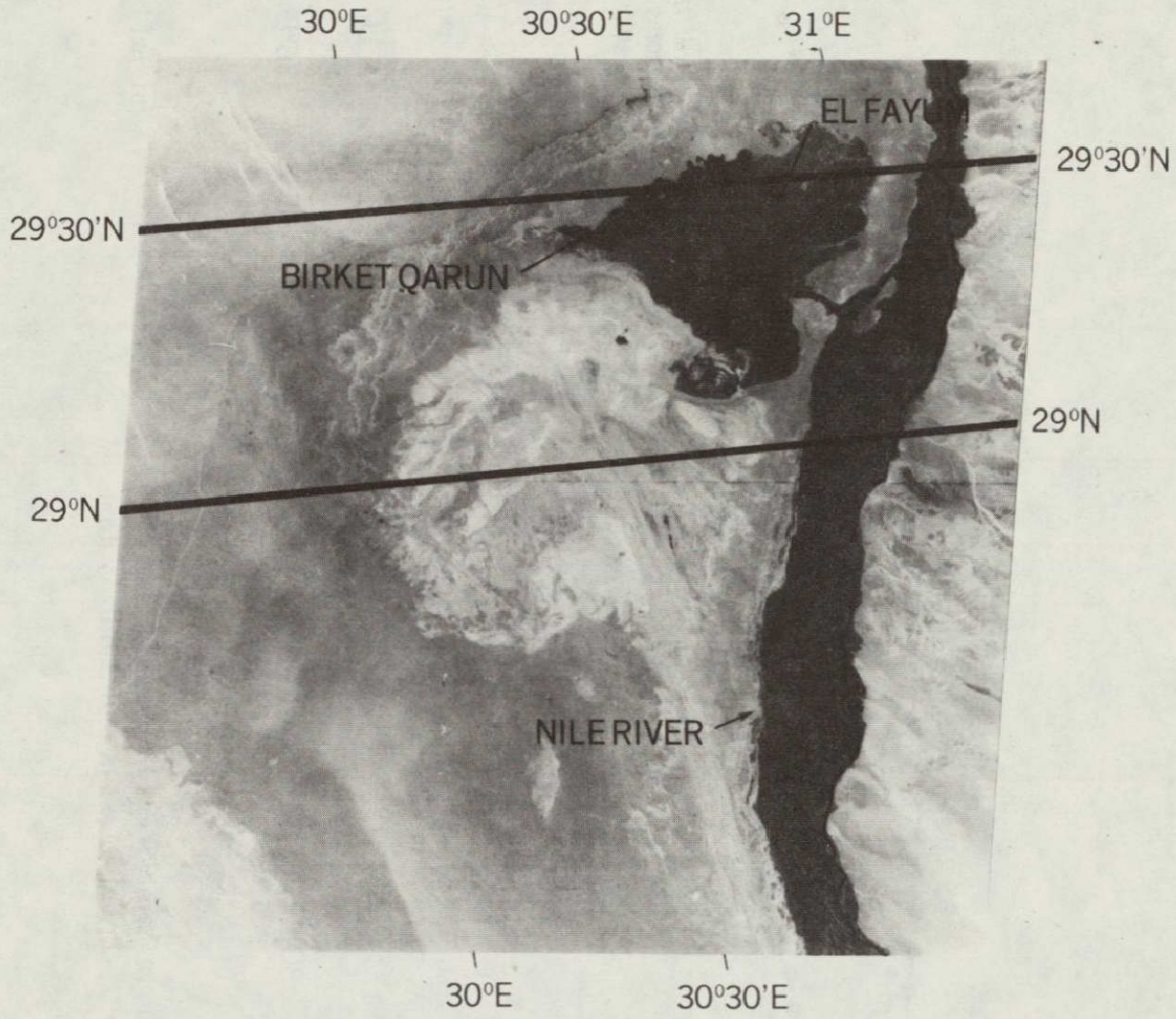

Figure 40. Landsat 2 MSS 7, 10 May 1973, El Fayum, Nile River Valley, Egypt (UAR) with box limits of THIR and ESMR T_B comparison

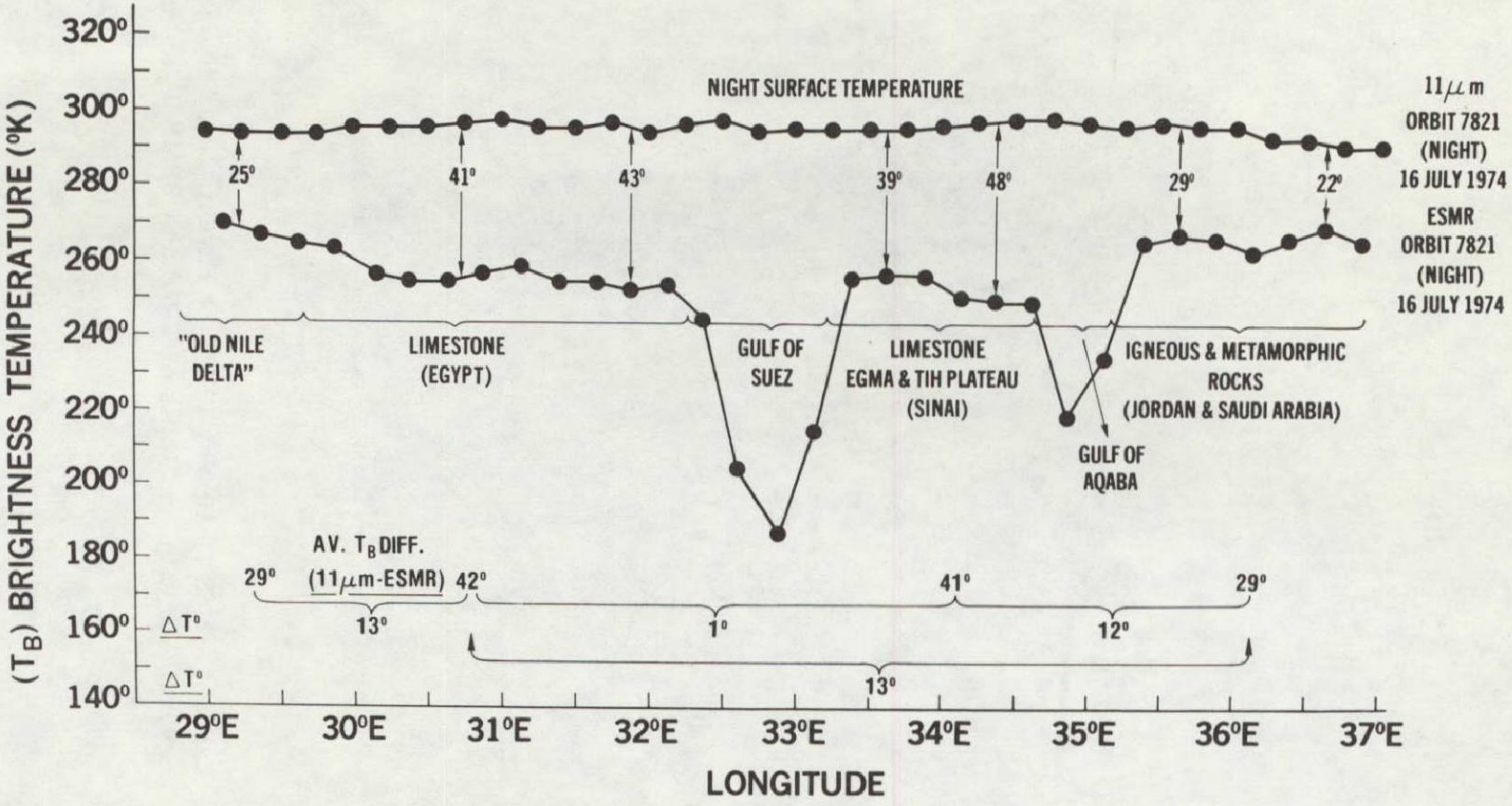

Figure 41. Comparison of Nimbus 5 THIR 11 μm and ESMR orbit 7821 16 July 1974 (night) between 29° N and 29° 30'N, Egypt, Jordan and Saudi Arabia

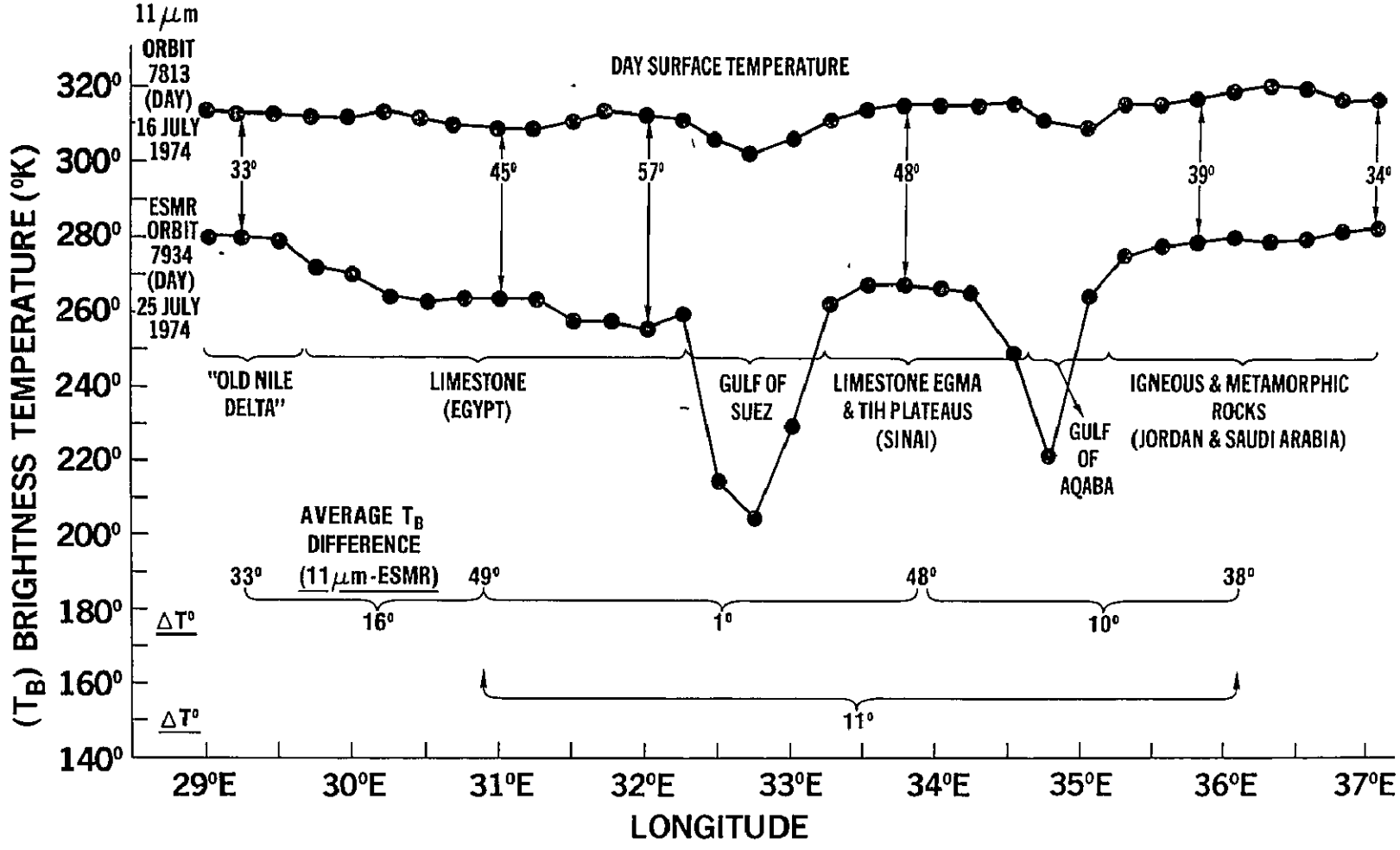

Figure 42. Comparison of Nimbus 5 THIR 11 μm, orbit 7813, 16 July 1974 (day) and ESMR, orbit 7934, 25 July 1974 (day), between 29°N and 29° 30'N, Egypt, Jordan and Saudi Arabia

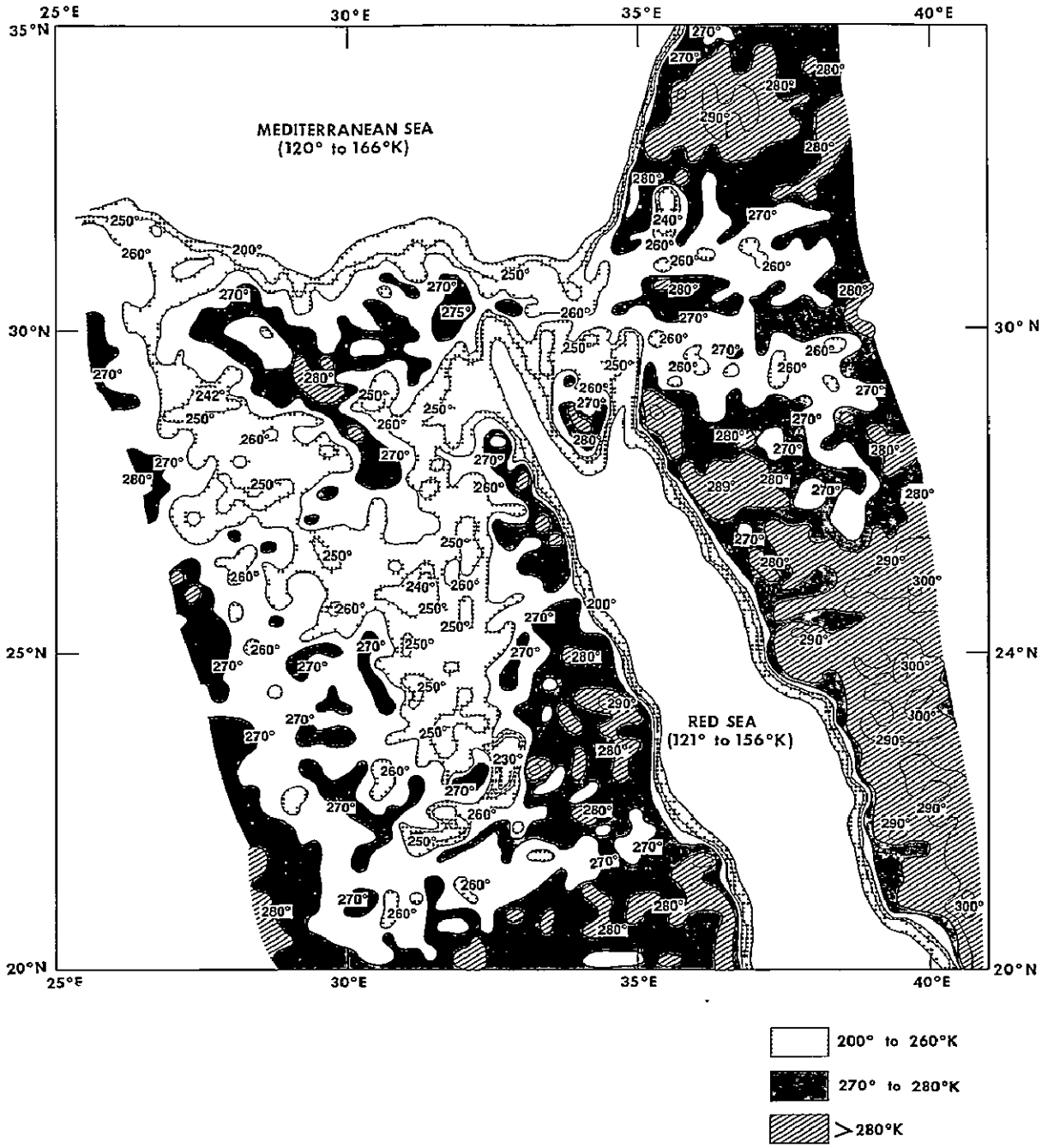

Figure 43. Nimbus 6 ESMR 37 GHz, orbit 618 (day), 28 July 1975, horizontal polarization; analysis of computer-produced grid print map, 1:2 million, Mercator

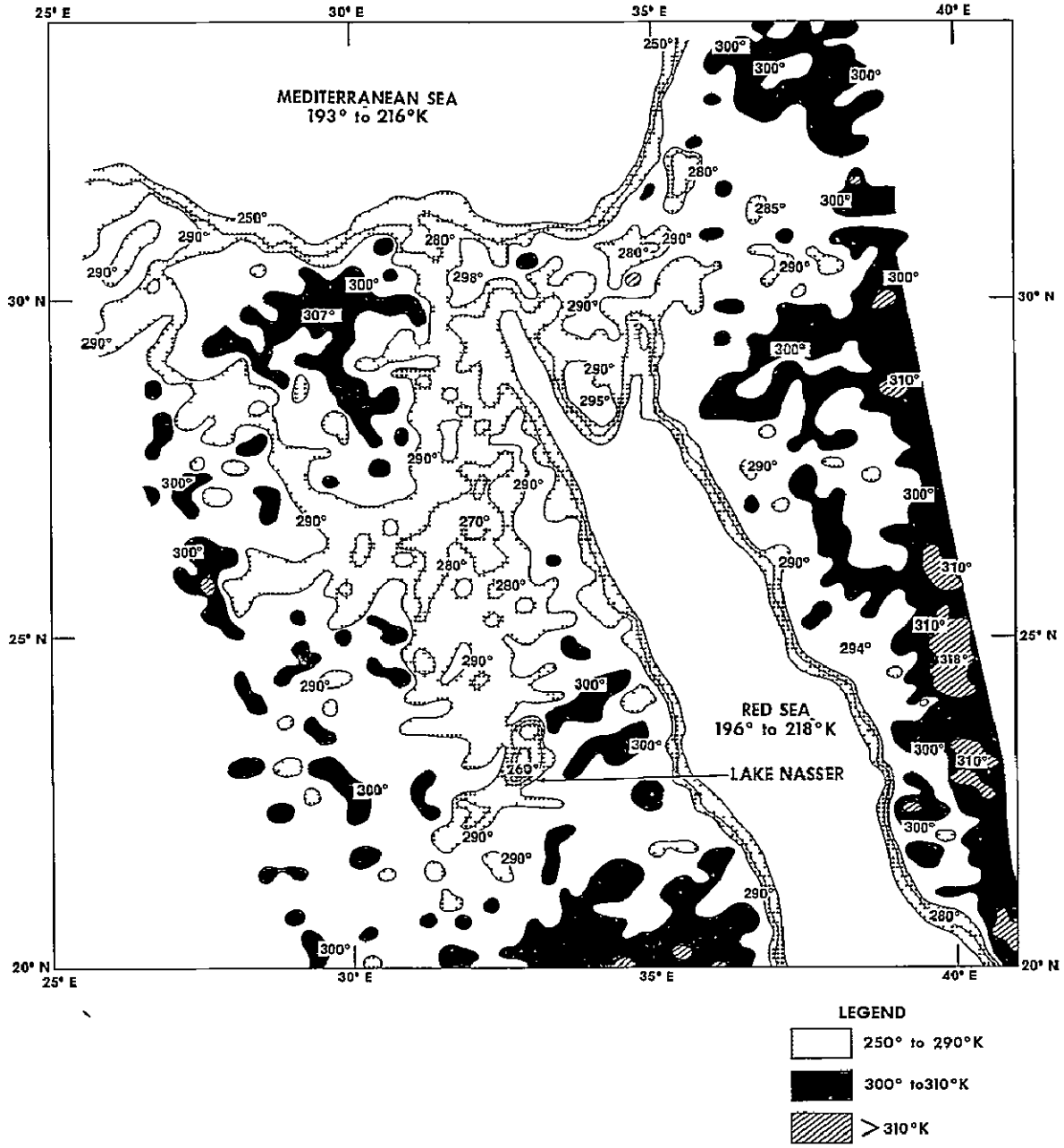

Figure 44. Nimbus 6 ESMR 37 GHz, orbit 618 (day), 28 July 1975, vertical polarization; analysis of computer-produced grid print map, 1:2 million, Mercator

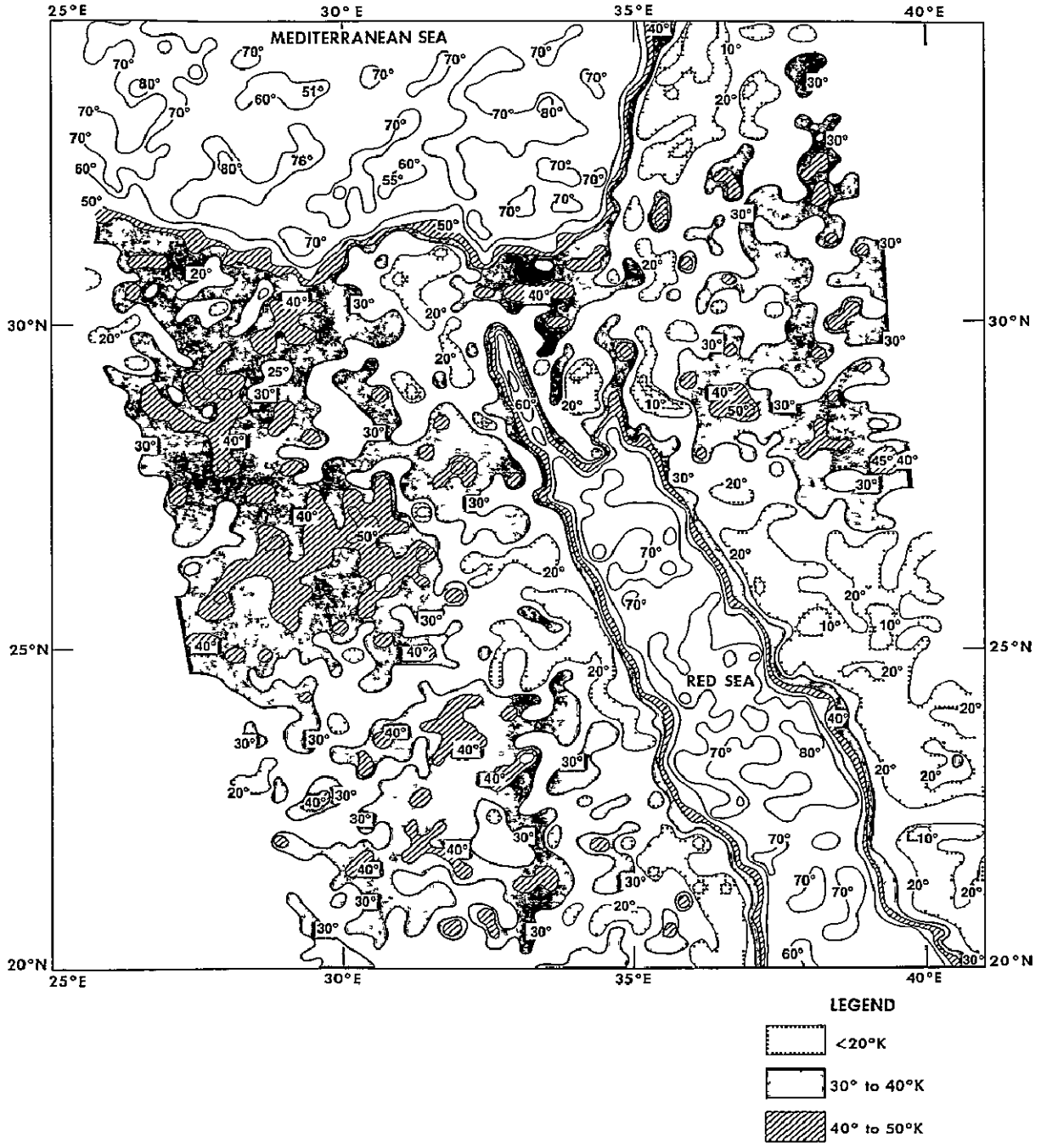

Figure 45. Nimbus 6 ESMR 37 GHz, orbit 846 (day), 14 August 1975, vertical minus horizontal polarization; analysis of computer-produced grid print map, 1:2 million, Mercator

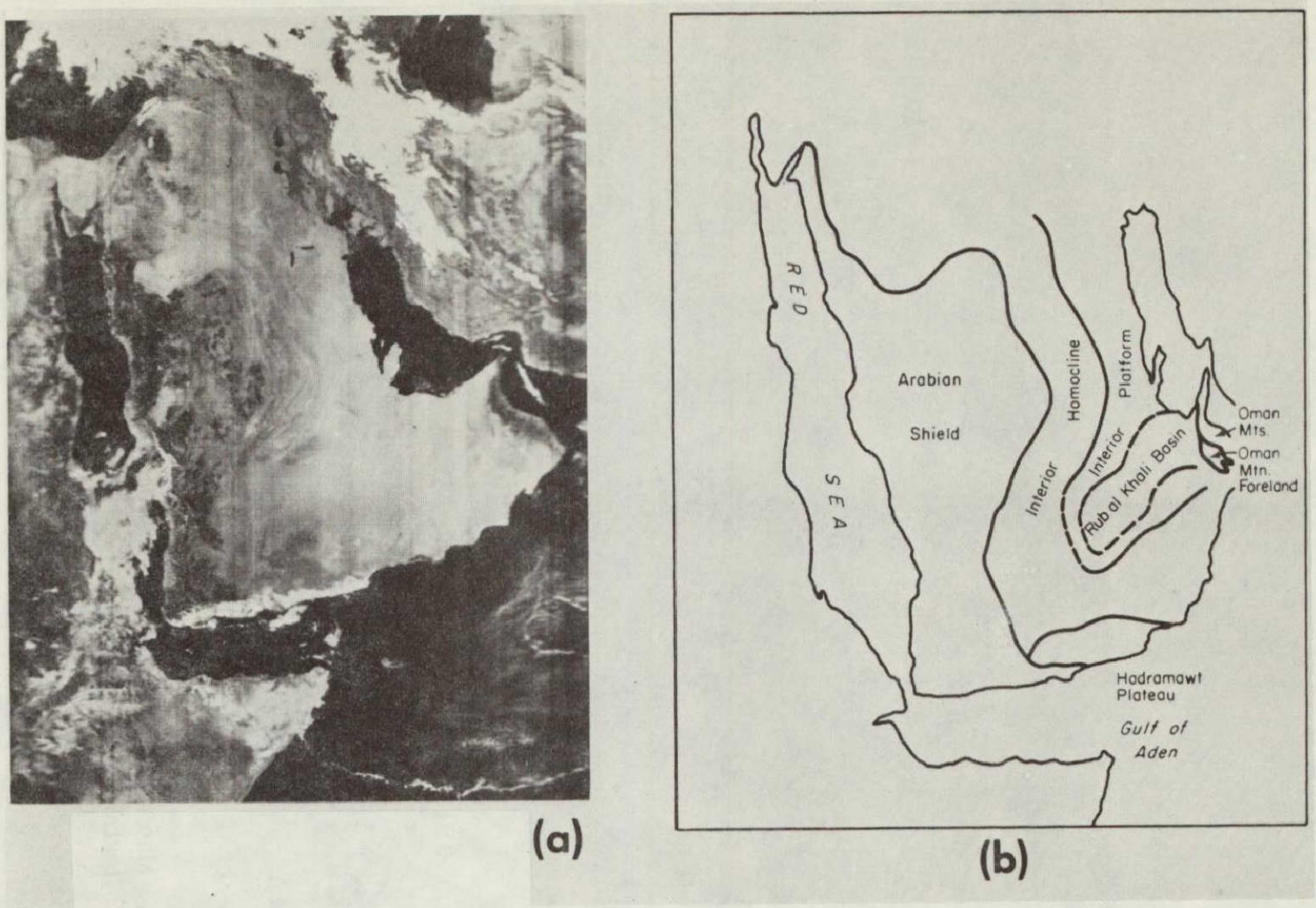

Figure 46. a) U.S. Air Force DMSP visual picture, orbit 4752, 14 Feb. 1975, 0837Z, (2 mile resolution) b) Map of Saudi Arabia indicating major geological features (Anon, U.S. Geological Survey, 1966)

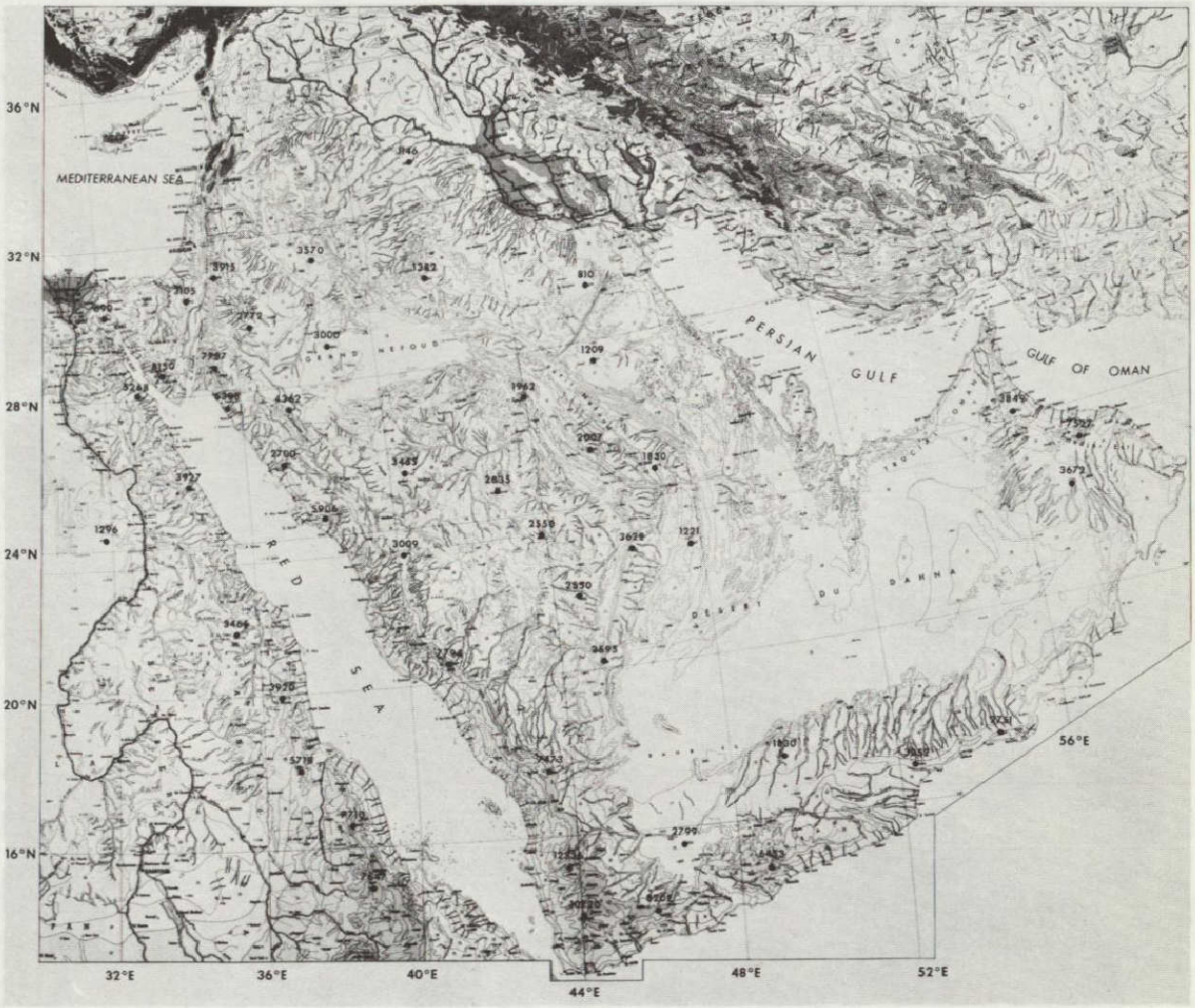

Figure 47. Map of Saudi Arabia and associated areas, elevations, land features, 1:5 million, (FAO-UNESCO Map, P. Laland)

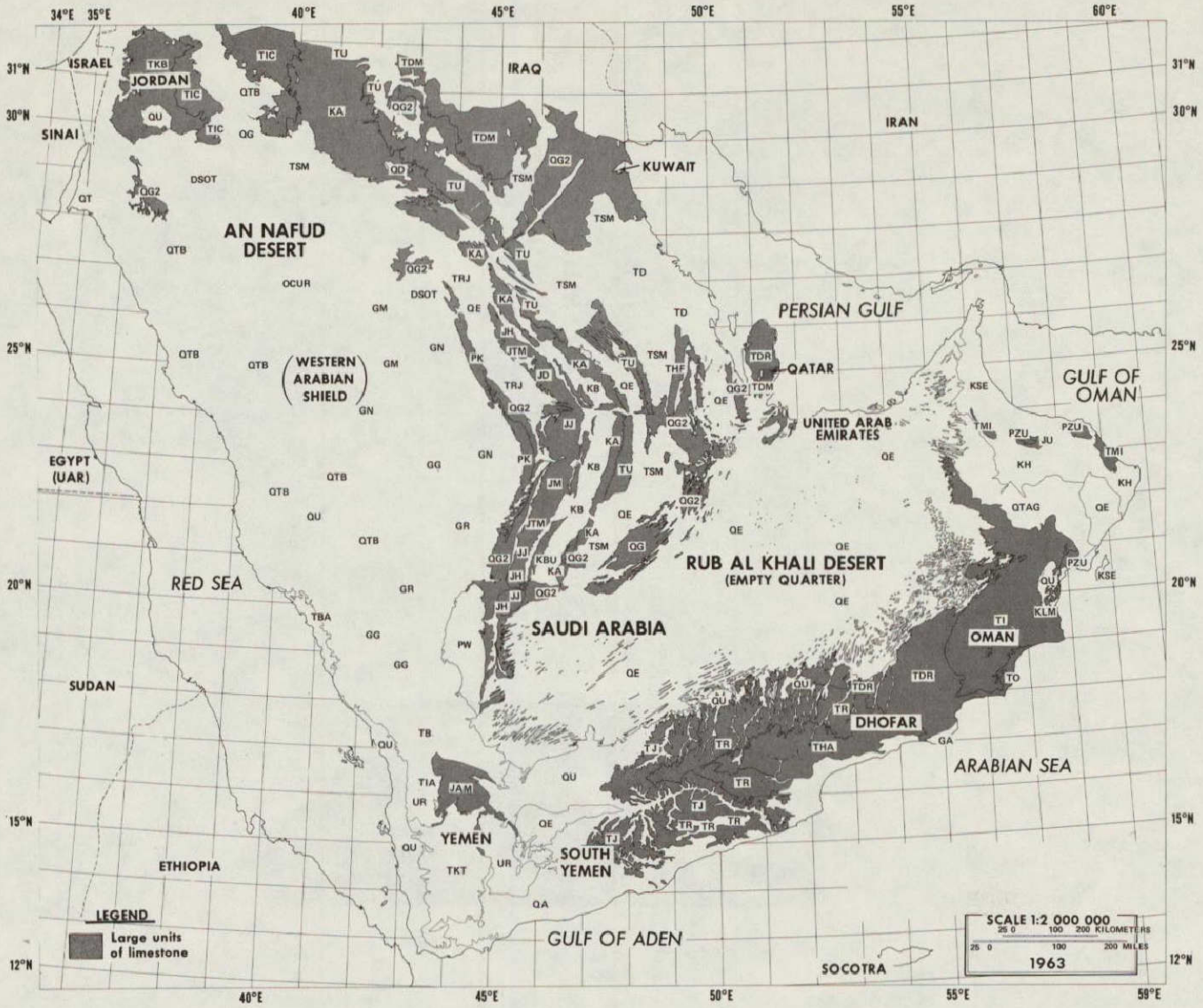

Figure 48. Geological map of the Arabian Peninsula, 1:2 million, indicating large units of limestone. (A complete description of the abbreviations on this figure may be found on legend of referenced map)

Figure 49. Nimbus 5 ESMR 19.35 GHz, orbit 3780 (night) 18 Sept. 1975, facsimile picture

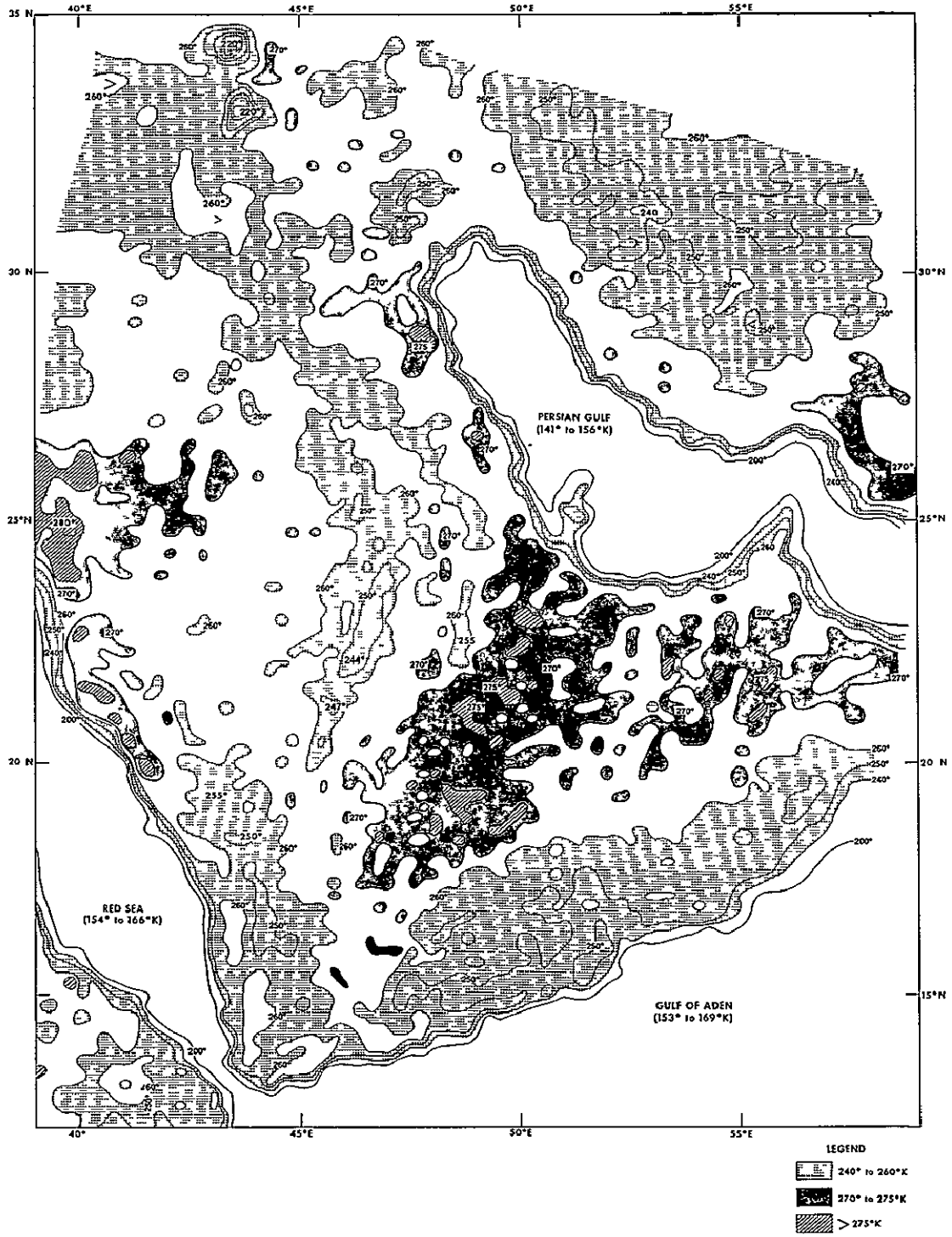

Figure 50. Nimbus 5 ESMR 19.35 GHz, orbit 3779 (night), 18 Sept. 1973, horizontal polarization; analysis of computer-produced grid print map, 1:2 million, Mercator

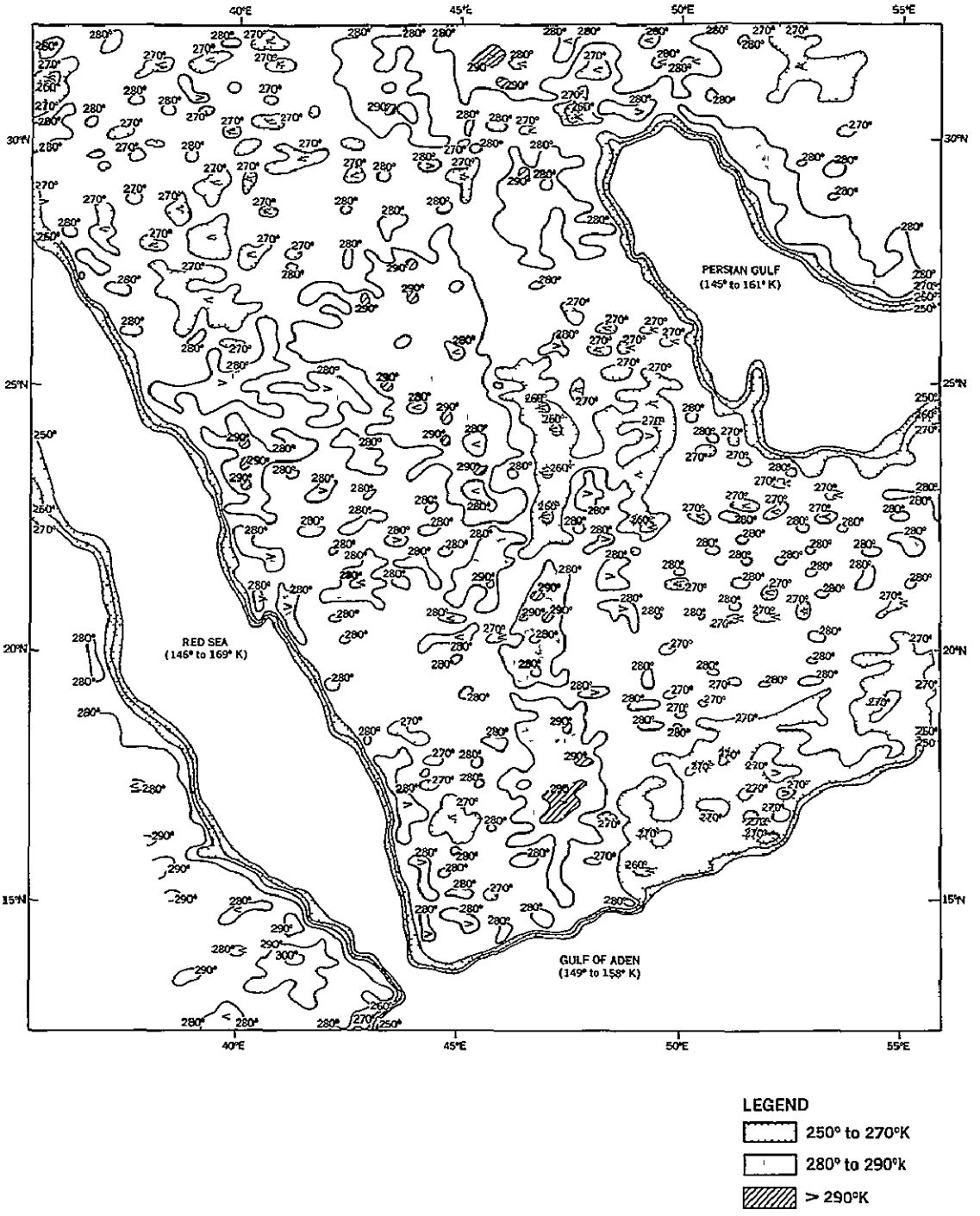

Figure 51. Nimbus 5 ESMR 19.35 GHz, orbit 3853 (day), 24 Sept. 1973, horizontal polarization; analysis of computer-produced grid print map, 1·2 million, Mercator

C 2

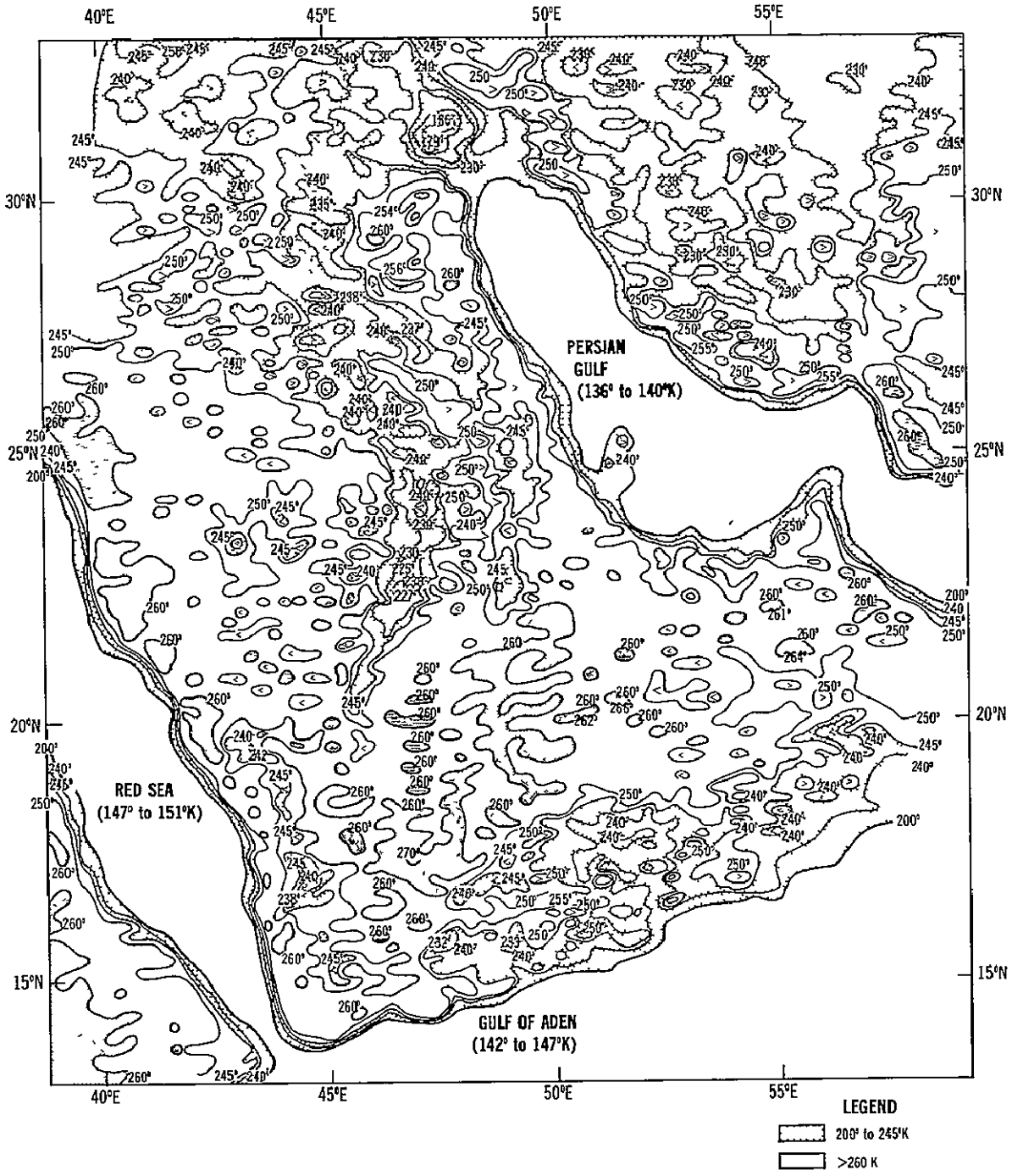

Figure 52. Nimbus 5 ESMR 19.35 GHz, orbit 10974 (night), 8 March 1975, horizontal polarization, analysis of computer-produced grid print map, 1:2 million, Mercator

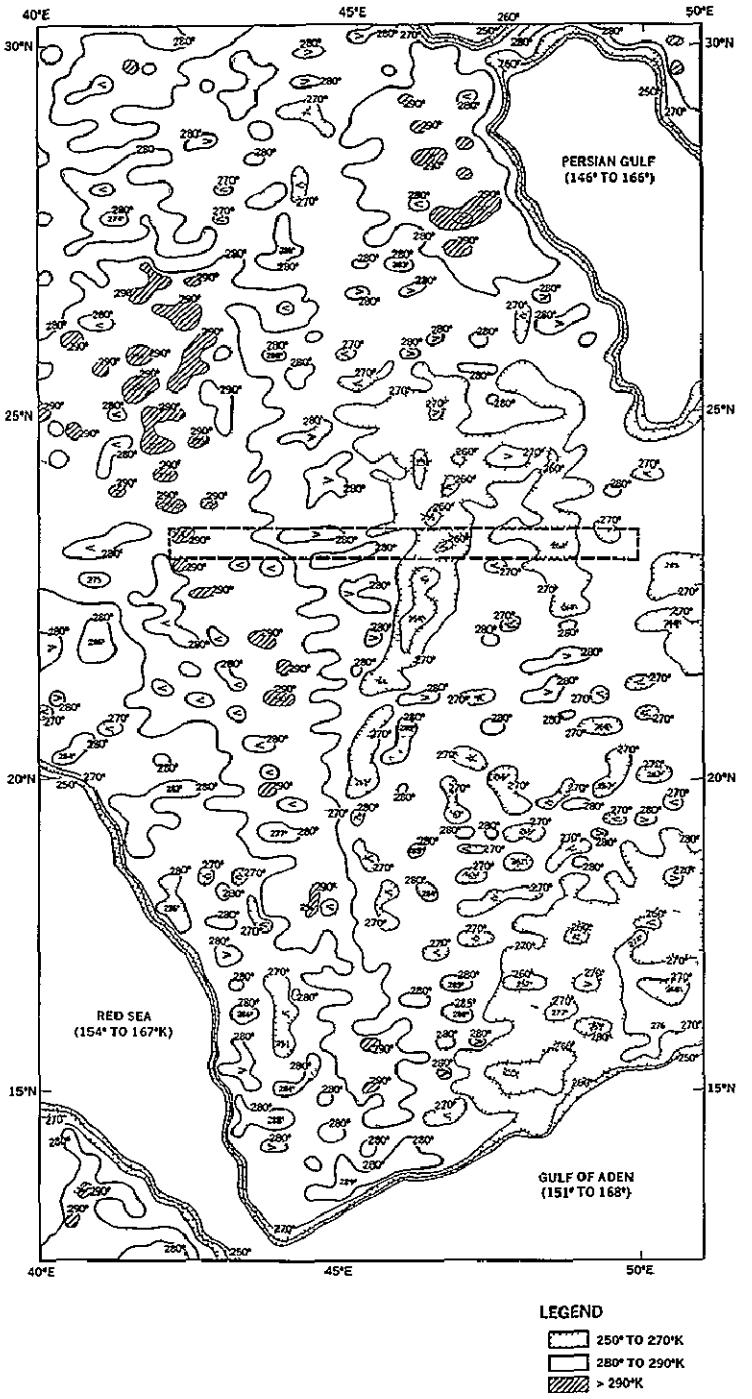

Figure 53. Nimbus 5 ESMR 19.35 GHz, orbit 7813 (day), 16 July 1974, horizontal polarization; analysis of computer-produced grid print map, 1:2 million, Mercator; dashed box indicates area of crossection shown in Fig. 55.

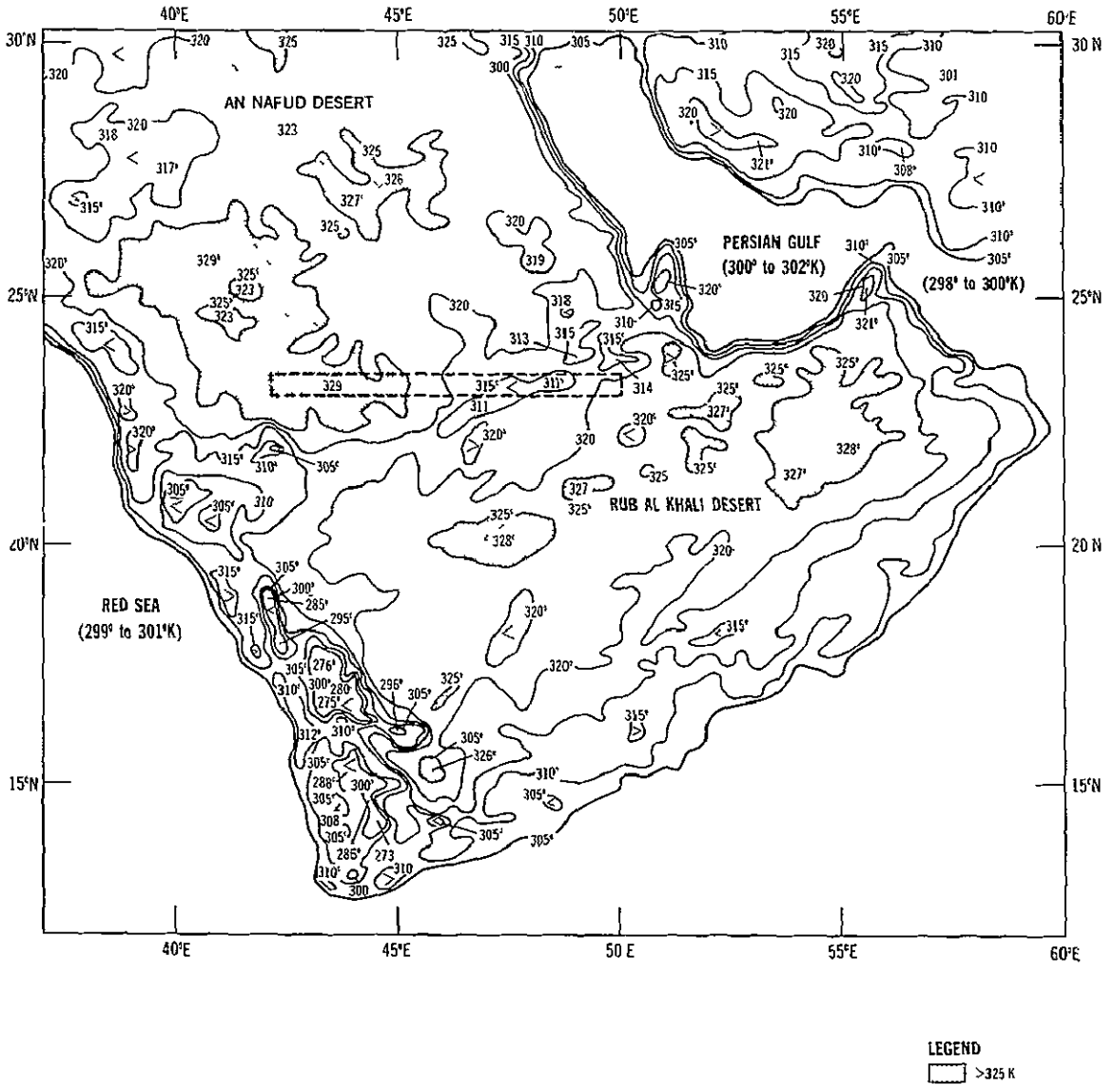

Figure 54. Nimbus 5 THIR 11 m orbit 7813 (day), 16 July 1974, analysis of computer-produced grid print map, 1:2 million, Mercator; dashed box indicates area of crossection shown in Fig. 55.

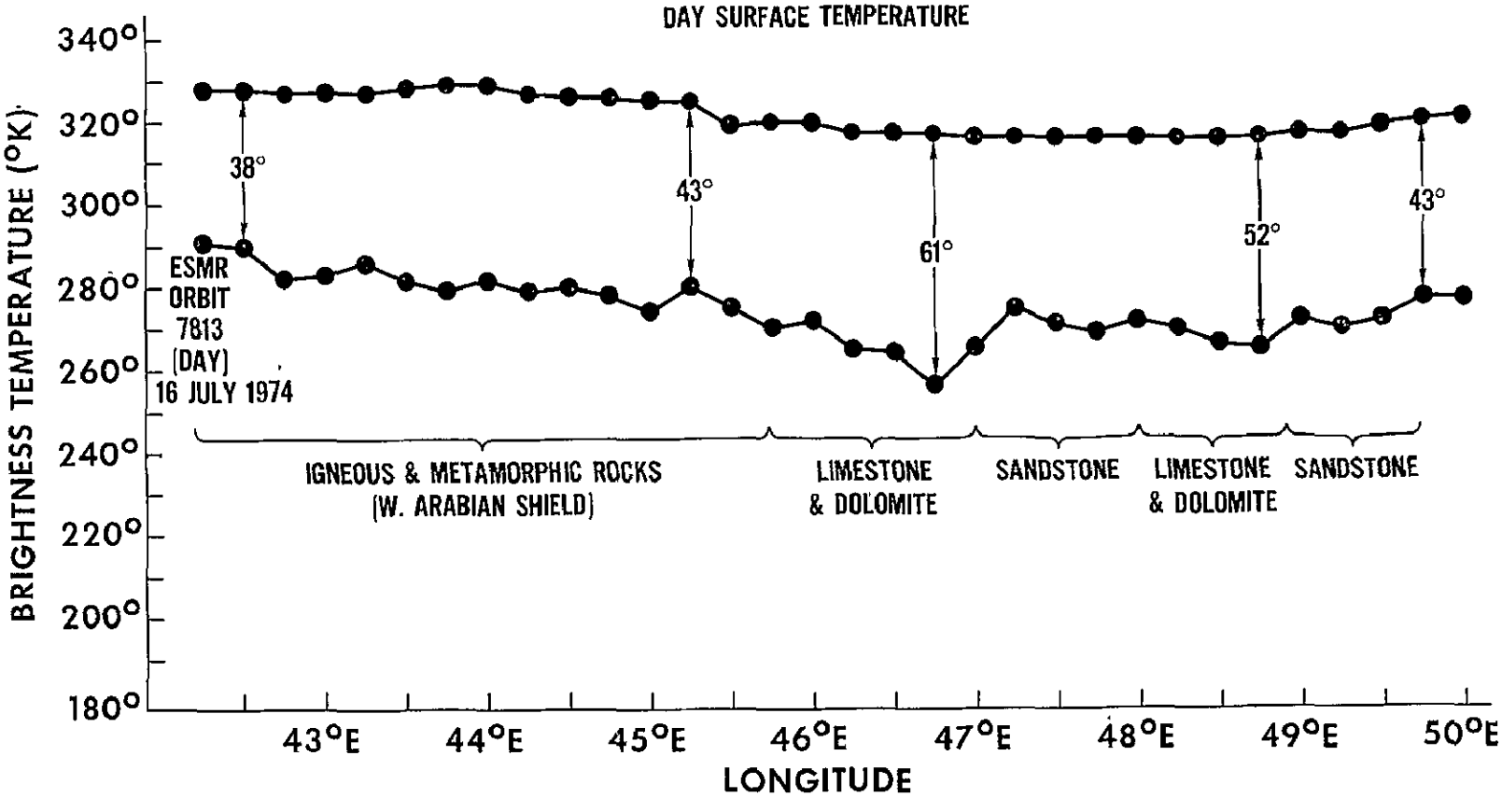

Figure 55. Comparison of Nimbus 5 THIR 11 μm and ESMR, orbit 7813 (day), between 23°N and 23° 30'N, Saudi Arabia

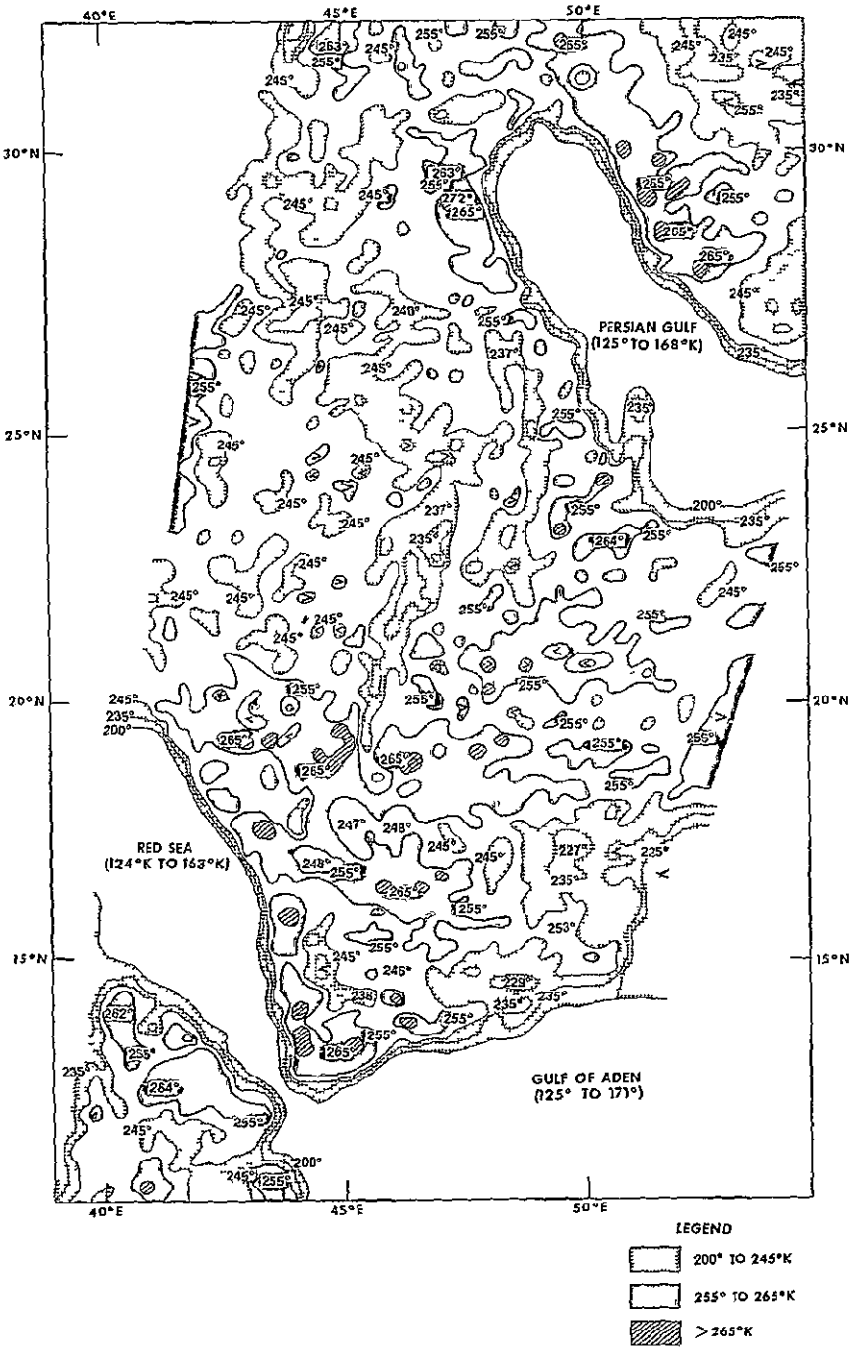

Figure 56. Nimbus 6 ESMR 37 GHz, orbit 880 (night), 16 August 1975, horizontal polarization; analysis of computer-produced grid print map, 1:2 million, Mercator

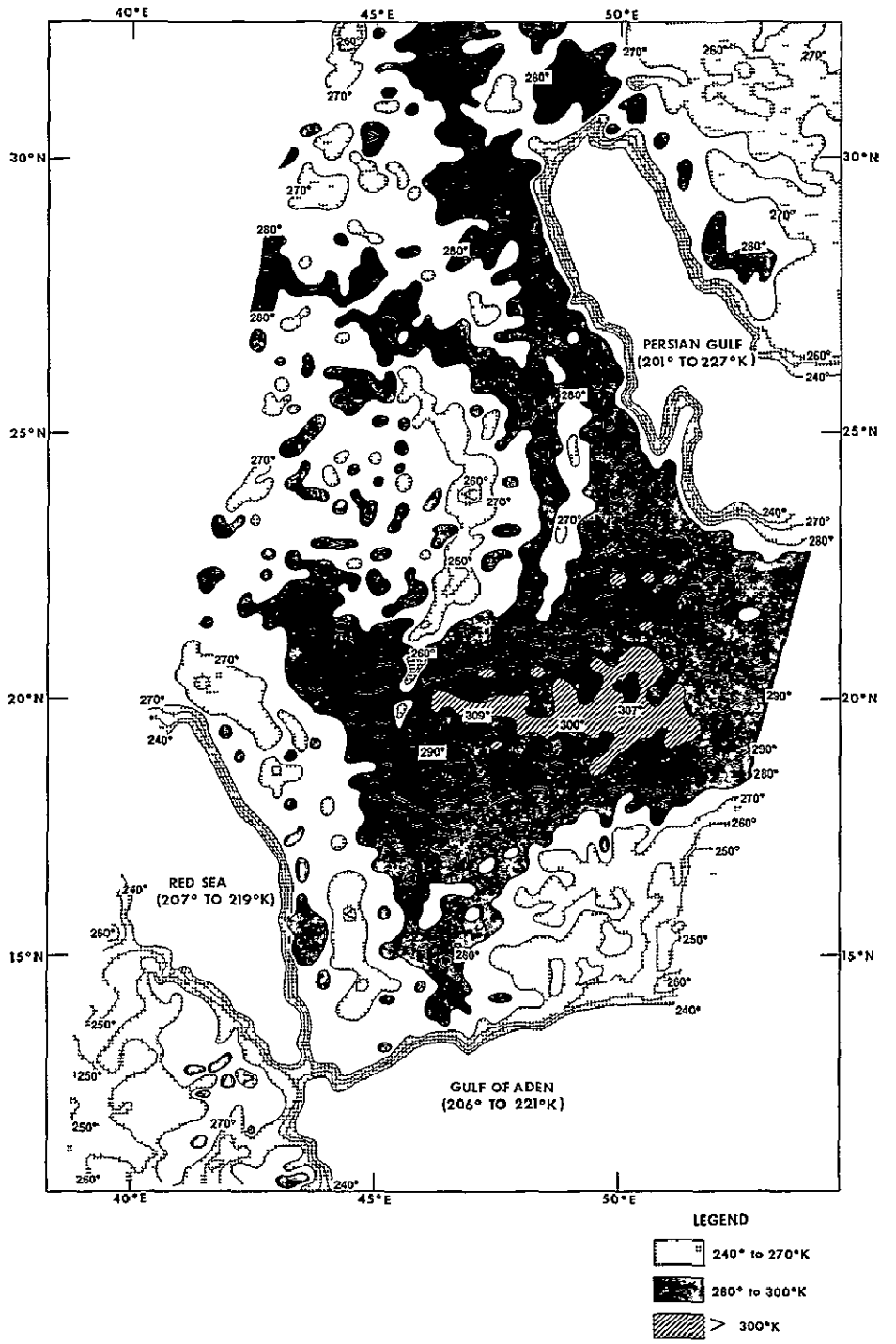

Figure 57. Nimbus 6 ESMR 37 GHz, orbit 880 (night), 16 August 1975, vertical polarization; analysis of computer-produced grid print map, 1:2 million, Mercator

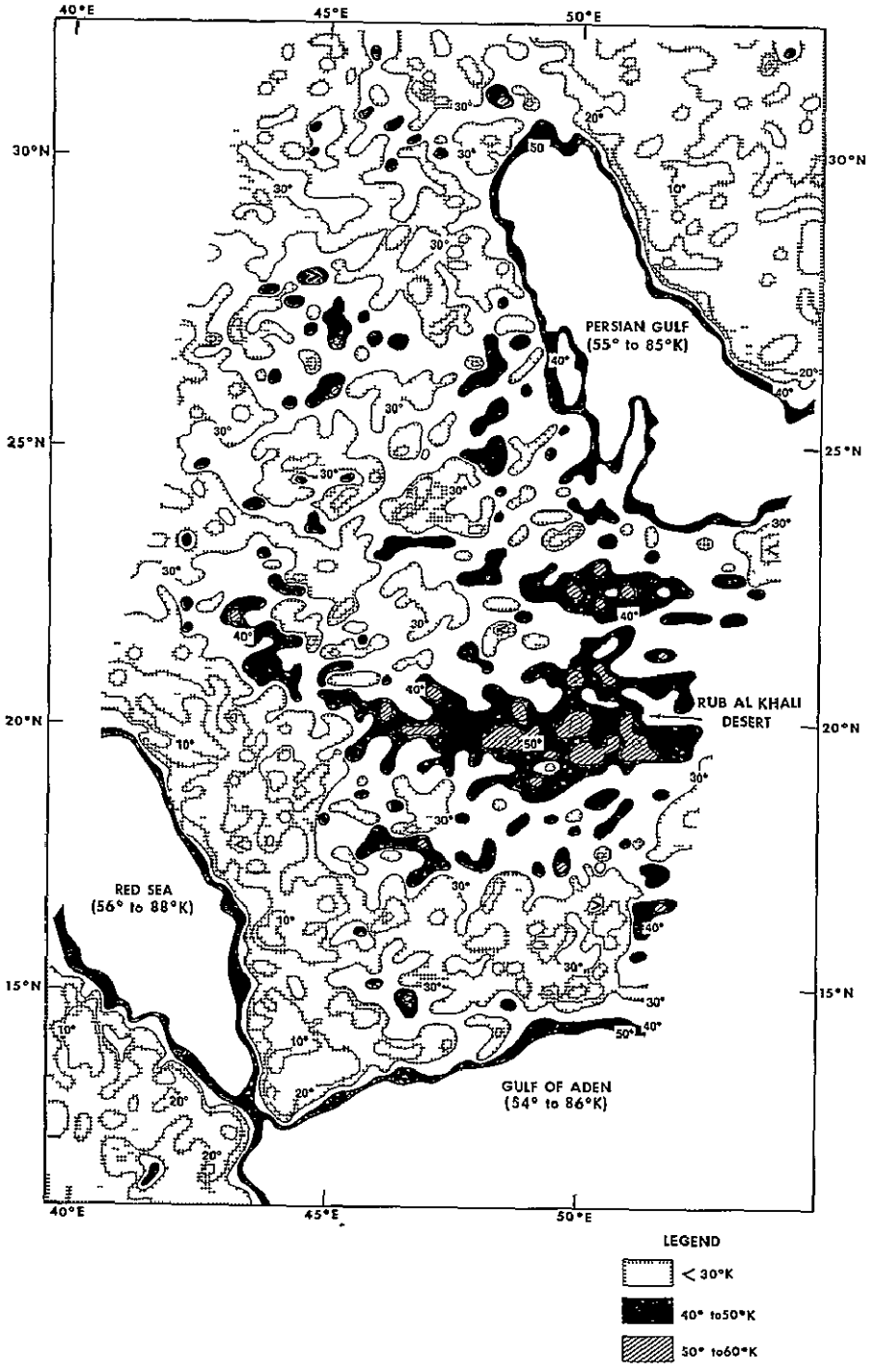

Figure 58. Nimbus 6 ESMR 37 GHz, orbit 880 (night), 16 August 1975, vertical minus horizontal polarization; analysis of computer-produced grid print map, 1:2 million, Mercator

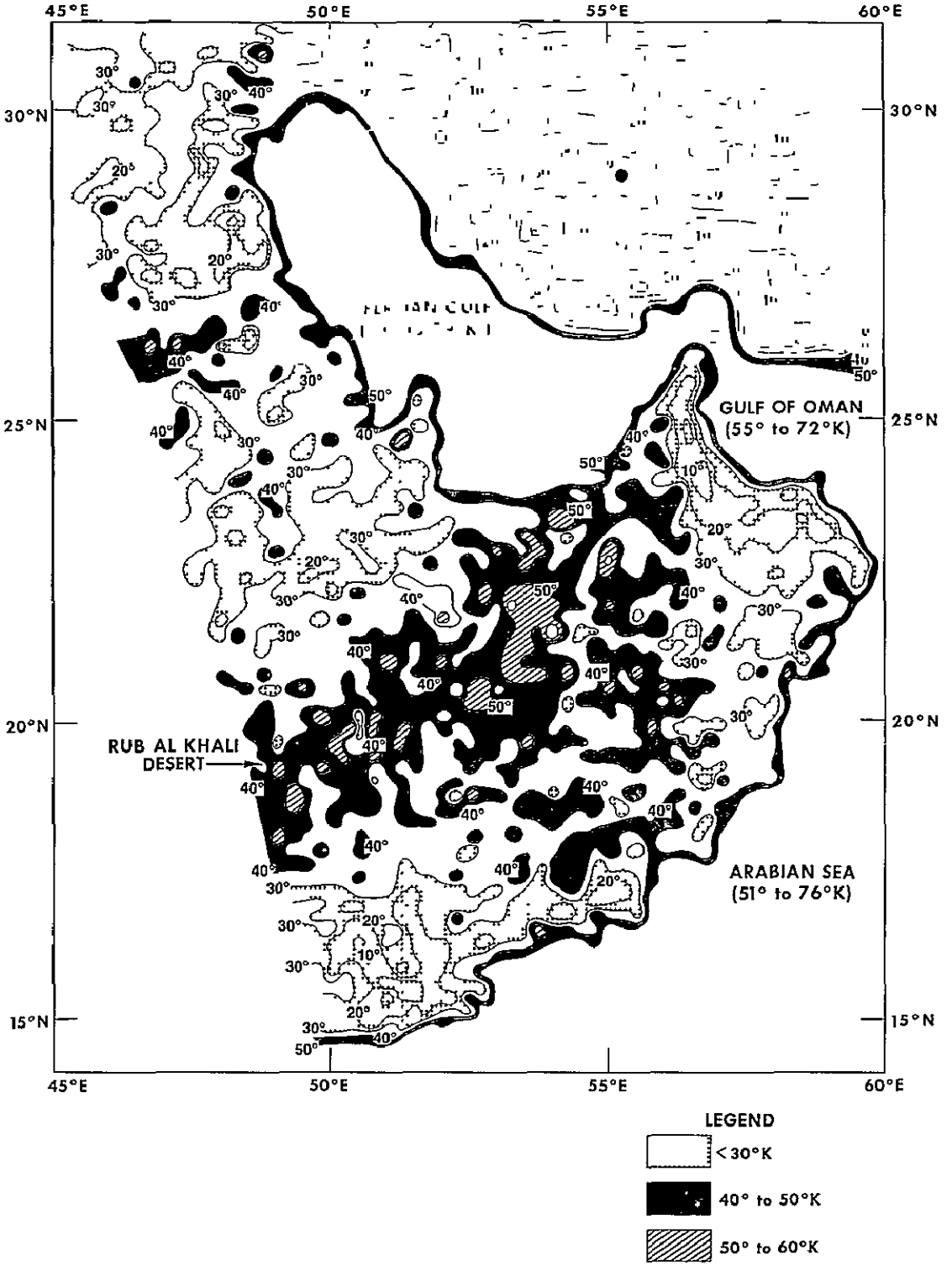

Figure 59. Nimbus 6 ESMR 37 GHz, orbit 738 (day), 6 August 1975, vertical minus horizontal polarization; analysis of computer-produced grid print map, 1:2 million, Mercator